ANN-ASSISTED NUMERICAL MODELLING OF LIFETIME ESTIMATION FOR SINGLE CRYSTALS IN TURBINE BLADES

A THESIS SUBMITTED TO
THE GRADUATE SCHOOL OF NATURAL AND APPLIED SCIENCES
OF
ATILIM UNIVERSITY

BY

UTKU KAFTANCIOĞLU

IN PARTIAL FULFILLMENT OF THE REQUIREMENTS
FOR
THE DEGREE OF DOCTOR OF PHILOSOPHY
IN
THE DEPARTMENT OF MECHANICAL ENGINEERING

JUNE 2025

Approval of the Graduate School of Natural and Applied Sciences, Atılım University.

_____

Assoc. Prof. Dr. Gökhan TUNÇ

Director

I certify that this thesis satisfies all the requirements as a thesis for the degree of **Doctor of Philosophy in Mechanical Engineering Department, Atılım University**.

_____

Prof. Dr. Hasan Umur AKAY

Acting Head of Department

This is to certify that we have read the thesis ANN-ASSISTED NUMERICAL MODELLING OF LIFETIME ESTIMATION FOR SINGLE CRYSTALS IN TURBINE BLADES submitted by UTKU KAFTANCIOĞLU and that in our opinion it is fully adequate, in scope and quality, as a thesis for the degree of Doctor of Philosophy.

_____

Prof. Dr. Özgür ASLAN

Supervisor

Examining Committee Members:

Prof. Dr. Ahmet Hakan ARGEŞO
Aerospace Engineering, Atılım University _____

Prof. Dr. Özgür ASLAN
Mechanical Engineering, University of Bristol _____

Asst. Prof. Dr. Ferit SAİT
Mechanical Engineering, Çankaya University _____

Asst. Prof. Dr. Hakan KALKAN
Mechanical Engineering, Atılım University _____

Asst. Prof. Dr. Bahram LOTFİ
Mechanical Engineering, TOBB ETU _____

Date: June 27, 2025

I declare and guarantee that all data, knowledge and information in this document has been obtained, processed and presented in accordance with academic rules and ethical conduct. Based on these rules and conduct, I have fully cited and referenced all material and results that are not original to this work.

Name, Last Name : UTKU KAFTANCIOĞLU

Signature :

ABSTRACT

ANN-ASSISTED NUMERICAL MODELLING OF LIFETIME ESTIMATION FOR SINGLE CRYSTALS IN TURBINE BLADES

Kaftancıoğlu, Utku

Ph.D., Department of Mechanical Engineering

Supervisor : Prof. Dr. Özgür ASLAN

June 2025, 138 pages

Nickel-based single crystal superalloys, such as CMSX-4, are the backbone of modern turbine blade applications due to their exceptional mechanical strength, creep resistance, and thermal stability under extreme service conditions. These materials are frequently subjected to complex thermo-mechanical fatigue (TMF) cycles, including high stress amplitudes, temperature gradients, and dwell times. Accurate lifetime assessment under such demanding loading conditions remains a critical challenge due to the anisotropic behavior of single crystals and the limited availability of experimental data, particularly for components used in aerospace and defense sectors. Motivated by these challenges, this thesis explores a hybrid predictive framework that combines physics-based continuum damage mechanics (CDM) with data-driven machine learning models to assess fatigue lifetime and identify material parameters with high precision, even under data scarcity.

A modified Chaboche continuum damage model serves as the foundation for the generation of synthetic fatigue lifetime data in this study. This model is tailored to capture the anisotropic behavior of FCC single crystal superalloys, incorporating temperature-dependent material responses across a range of stress ratios and loading conditions. However, the broader fatigue lifetime prediction framework is built upon artificial

neural networks (ANNs), which are trained on multiple types of input data. Two distinct ANN-based models are introduced. The first model uses semi-synthetic datasets combining experimental fatigue and creep data with limited UTS/endurance information to predict both creep rupture time and fatigue lifetime under high-cycle and combined-cycle fatigue (HCF and CCF) conditions. The second model is trained exclusively on fully synthetic SN curves generated using the modified Chaboche law. It is designed to reproduce lifetime predictions across various temperatures and R-ratios, generating SN curves and Goodman diagrams from normalized, log-scaled inputs. Together, these models establish a predictive backbone capable of extrapolating fatigue behavior across a wide range of operational domains.

To overcome the critical limitation of sparse and scattered experimental fatigue data, transfer learning strategies are applied to adapt the synthetic-data-trained ANNs to experimental datasets from both CMSX-4 and generic metals such as AISI 4340. Two transfer learning models are developed: one based on direct parameter tuning of a pretrained model and another incorporating an input expansion scheme to integrate new physical variables. These models are evaluated using leave-one-out cross-validation (LOOCV) to ensure robustness and generalizability. The transfer learning approach demonstrates significant potential in predicting fatigue lifetime from minimal experimental data while preserving model consistency across temperature and R-ratio domains.

In addition to fatigue life prediction, the thesis presents a data-driven parameter optimization pipeline designed to infer constitutive model parameters from stress–strain data. This approach leverages a custom-built finite element-based simulation loop to generate datasets using a rate-independent J2 plasticity model with Voce-type hardening. A neural network regressor is trained to map the full stress–strain profile to the underlying material parameters, enabling inverse modeling from experimental or simulated mechanical responses. This framework is capable of recovering key material constants efficiently and accurately, even for highly nonlinear plastic behavior.

Overall, the proposed framework offers a versatile and scalable methodology for fatigue life assessment, model calibration, and data augmentation in high-performance materials. By synthesizing synthetic data generation, ANN-based regression, and

transfer learning under a unified pipeline, this thesis addresses the longstanding challenge of modeling fatigue in anisotropic, high-temperature materials with limited experimental support. The methods developed here not only contribute to predictive accuracy but also enhance the interpretability and adaptability of fatigue modeling tools in critical applications such as gas turbine engine components.

Keywords: Lifetime Assessment Modelling, Artificial Neural Networks, Transfer Learning, Single Crystal Nickel Based Superalloys, Parameter Optimization

ÖZ

TÜRBİN KANATLARINDA TEK KRİSTALLERİN ÖMÜR TAHMİNİ İÇİN YAPAY SİNİR AĞI DESTEKLİ SAYISAL MODELLEMESİ

Kaftancıoğlu, Utku

Doktora, Makine Mühendisliği

Tez Yöneticisi : Prof. Dr. Özgür ASLAN

Haziran 2025, 138 sayfa

Nikel bazlı tek kristalli süperalaşımlar, üstün mekanik dayanımları, sünme direnci ve yüksek sıcaklıklardaki kararlılıkları sayesinde modern türbin kanadı uygulamalarının temel malzemeleri arasında yer almaktadır. Bu malzemeler, yüksek gerilme genlikleri, sıcaklık gradyanları ve bekletme sürelerini içeren karmaşık termomekanik yorulma (TMF) döngülerine sıklıkla maruz kalmaktadır. Özellikle uzay ve savunma sanayisinde kullanılan bileşenler için deneysel veri kısıtlılığı ve tek kristallerin anizotrop davranışı, bu zorlayıcı yükleme koşulları altında yorulma ömrü tahminini oldukça güçleştirmektedir. Bu zorluklardan yola çıkan bu tez, yorulma ömrünü tahmin etmek ve sınırlı veri koşullarında bile malzeme parametrelerini yüksek doğrulukla belirlemek amacıyla fizik tabanlı sürekli hasar mekaniğini (CDM) ve veri odaklı makine öğrenimi modellerini birleştiren hibrit bir öngörü çerçevesi sunmaktadır.

Bu tez çalışmasında, sentetik yorulma ömrü verilerinin oluşturulmasında temel olarak kullanılan model, FCC kristal yapısına sahip tek kristalli süperalaşımların anizotrop davranışlarını ve sıcaklığa bağlı malzeme tepkilerini dikkate alan, özelleştirilmiş bir Chaboche sürekli hasar modeli olmuştur. Ancak, yorulma ömrü tahmininde esas rolü oynayan yapı, farklı veri türleriyle eğitilen yapay sinir ağı (YSA) modelleridir. Tezin üçüncü bölümünün başında iki ayrı YSA modeli tanıtılmaktadır. İlk model, sınırlı ni-

hai çekme dayanımı ve dayanım bilgileriyle birlikte deneysel yorulma ve sünme verilerinden oluşturulan yarı-sentetik veri setini kullanarak hem sünme kopma süresini hem de yüksek çevrimli ve birleşik çevrimli yorulma (HCF ve CCF) koşullarındaki yorulma ömrünü tahmin etmektedir. İkinci model ise tamamen, özelleştirilmiş Chaboche modeli ile oluşturulan sentetik SN eğrileri ile eğitilmiştir. Bu model, sıcaklık ve R oranlarına bağlı olarak normalleştirilmiş ve logaritmik ölçeklenmiş girdiler üzerinden SN eğrileri ve Goodman diyagramları üretmek üzere yapılandırılmıştır. Bu iki model, geniş çalışma koşullarını kapsayabilen tahmin altyapısını oluşturmaktadır.

Deneysel yorulma verilerinin dağınık ve yetersiz olması problemini aşmak amacıyla, sentetik verilerle eğitilen YSA modelleri, transfer öğrenmesi yaklaşımlarıyla hem CMSX-4 hem de AISI 4340 gibi genel metal türleri için elde edilen deneysel veri kümelerine uyarlanmıştır. Bu bağlamda, biri önceden eğitilmiş modelin parametrelerinin doğrudan ayarlanmasına, diğeri ise yeni fiziksel değişkenlerin modele dâhil edilmesini sağlayan bir giriş genişletme yapısına dayalı iki farklı transfer öğrenmesi modeli geliştirilmiştir. Her iki model de veri güvenilirliğini sağlamak amacıyla bırak-bir çapraz doğrulama (LOOCV) yöntemi ile değerlendirilmiştir. Bu yaklaşımlar, sınırlı deneysel veriyle yorulma ömrü tahminlerinin gerçekleştirilebileceğini ve model tutarlılığının sıcaklık ve gerilme oranı ekseninde korunabileceğini göstermektedir.

Yorulma ömrü tahminine ek olarak, bu tezde, gerilme-şekil değiştirme verilerinden malzeme model parametrelerini tersine belirlemeyi amaçlayan, veri odaklı bir parametre optimizasyonu süreci de sunulmaktadır. Bu kapsamda, Voce tipi izotropik pekleşme içeren, oransal olmayan J2 plastiklik modeli ile oluşturulan sonlu eleman simülasyonları üzerinden bir veri seti üretilmiş ve tam gerilme-şekil değiştirme eğrisinden model parametrelerine haritalama yapabilen bir YSA regresyon modeli eğitilmiştir. Bu yapı, güçlü doğrusal olmayan plastik davranışlarda dahi temel malzeme sabitlerini yüksek doğrulukla ve verimli bir şekilde geri kazanabilmektedir.

Sonuç olarak, bu tezde sunulan yöntemsel yapı, yüksek performanslı malzemelerde yorulma ömrü değerlendirmesi, model kalibrasyonu ve veri genişletmesi gibi alanlarda esnek ve ölçeklenebilir bir çözüm sağlamaktadır. Sentetik veri üretimi, YSA tabanlı regresyon ve transfer öğrenmesini tek bir çerçevede birleştiren bu yaklaşım, sınırlı deneysel destekle anizotropik ve yüksek sıcaklık dayanımı gerektiren malzeme-

lerin yorulma modellemesine dair süregelen zorluklara etkin bir çözüm sunmaktadır. Bu kapsamda geliştirilen yöntemler, yalnızca tahmin doğruluğunu artırmakla kalmayıp, aynı zamanda gaz türbin motoru bileşenleri gibi kritik uygulamalarda yorulma modelleme araçlarının yorumlanabilirliğini ve uyarlanabilirliğini de geliştirmektedir.

Anahtar Kelimeler: Ömür Tahmin Modellemesi, Yapay Sinir Ağları, Transfer Öğrenmesi, Tek Kristalli Nikel Bazlı Süperalaşımlar, Parametre Optimizasyonu

ACKNOWLEDGMENTS

First and foremost, I would like to express my deepest gratitude to my supervisor, Prof. Dr. Özgür Aslan, for his unwavering guidance, support, and mentorship throughout the course of my doctoral studies. His expertise, insightful feedback, and encouragement have been invaluable at every stage of my research. I am truly grateful for the opportunities he provided and for the trust he placed in me, which greatly contributed to my academic and personal growth.

I would also like to sincerely thank the members of my thesis committee for their valuable time, feedback, and guidance. My special thanks go to Prof. Dr. Ahmet Hakan Argeşo, who not only served as the head of my thesis committee but also supported me as a member of my thesis monitoring committee. I am equally thankful to Asst. Prof. Dr. Ferit Sait for his constructive input and for his role in the monitoring committee. Furthermore, I extend my appreciation to Asst. Prof. Dr. Bahram Lotfi and Asst. Prof. Dr. Hakan Kalkan for their insightful comments and contributions that helped improve the quality of this thesis.

I am especially thankful to Prof. Dr. Emin Bayraktar for his generous support and guidance, which greatly contributed to my academic development and research success. I would also like to express my appreciation to my colleague Çağatay Kasar for his valuable collaboration throughout my doctoral studies. My sincere thanks also go to the members of the Computational Science & Engineering Laboratory (CSE-Lab), especially Gamze Çakır Kabakcı and Caner Çamalan, for their assistance and encouragement.

I gratefully acknowledge the financial support provided by the Scientific and Technological Research Council of Turkey (TÜBİTAK) and TUSAŞ Engine Industries (TEI) within the scope of the TÜBİTAK 2244 Industrial PhD Program under project number 119C037.

Finally, I would like to express my heartfelt gratitude to my parents, Macide and Ünver Kaftancıoğlu, for their constant support, patience, and understanding throughout this challenging and rewarding endeavor. I am also deeply thankful to my friends Can Şanlıtürk, Cansu Kasar, Mertcan Sevinç, Esma Selek and Engin Deniz Uçak for their unwavering encouragement and companionship along the way.

TABLE OF CONTENTS

ABSTRACT iii

ÖZ vi

ACKNOWLEDGMENTS ix

TABLE OF CONTENTS xi

LIST OF TABLES xv

LIST OF FIGURES xvii

CHAPTER

1 INTRODUCTION 1

1.1 Background 1

1.1.1 Failures in Turbine Blades 3

1.1.2 Single-Crystal Nickel-Based Superalloys 5

1.1.2.1 Microstructure and Creep Resistance . 5

1.1.2.2 Alloy Systems and Applications in Turbine Blades 5

1.1.2.3 Production and Crystallographic Orientation Effects 6

1.1.2.4 Anisotropic Fatigue and Crack Propagation Behavior 6

1.1.3 Lifetime Assessment Modeling 7

1.1.3.1 Stress/Strain-Life (Safe-Life) Methods 7

1.1.3.2 Fracture Mechanics (Damage-Tolerance) Approaches 7

1.1.3.3 Continuum Damage Mechanics (CDM) Models 8

1.1.3.4 Energy-Based and Statistical Methods 8

1.1.3.5 Multiaxial and Thermomechanical Fatigue (TMF) 9
1.1.3.6 Machine Learning Based Methods . . 10
1.1.3.7 Physics-Guided and Hybrid Approaches 10
1.2 Scope and Objectives 11
1.3 Thesis Outline 13
2 FATIGUE LIFE MODELING WITH CONTINUUM DAMAGE MECHANICS 15
2.1 History of CDM-Based Prediction Models 15
2.2 Isotropic Fatigue Damage Model 17
2.2.1 Variable Amplitude Loading 18
2.2.2 Nonlinear Damage Accumulation 21
2.3 Extension to FCC Single-Crystal Superalloys 23
2.3.1 Small Strain Crystal Plasticity 24
2.3.2 Critical Stress Determination 27
2.4 Fatigue Life Prediction on Notched Specimen 29
2.4.1 Material and Specimen Geometry 30
2.4.2 Finite Element Model of the Nothced Specimen . . 31
2.4.3 Post-Scripting of Modified Chaboche Model 32
2.4.4 Results and Discussion 33
3 ANN-BASED LIFETIME ESTIMATION 39
3.1 Literature Review 39
3.1.1 Early Development of Artificial Neural Networks . 39
3.1.2 Applications to Engineering and Materials Science 40
3.1.3 ANNs for Lifetime Estimation 41
3.1.4 Recent Advances in Lifetime Prediction 41
3.2 Fundamentals of Artificial Neural Networks 42
3.2.1 Artificial Neuron and Network Architecture 43
3.2.2 Activation Functions 44
3.2.3 Loss Functions and Optimization Methods 46

3.3 Training with Experimental and Semi-Generated Data 51
3.4 Training with Synthetic Data Generated from the Chaboche Model 55
3.4.1 Material Parameter Selection and Temperature-Specific Optimization 55
3.4.2 Synthetic Data Generation via Chaboche Model . . 56
3.4.3 Model Architecture and Training Setup 58
3.4.4 Prediction and Evaluation Results 60
3.4.5 Uncertainty Analysis and Model Robustness 62
3.4.6 Discussion on Generalization Capability 63
3.5 Transfer Learning 64
3.5.1 Introduction 64
3.5.2 Synthetic Data Generation 65
3.5.3 Transfer to Experimental Data 73
3.6 Input Expansion Approach 79
3.6.1 Method Description 79
4 PARAMETER OPTIMIZATION WITH NEURAL NETWORKS . . 88
4.1 Introduction 88
4.2 Optimization Workflow 90
4.3 Parametric Modeling in Abaqus 92
4.3.1 Parametric Input via *Parameter Block 92
4.3.2 Parameter Study with ParStudy API 93
4.3.3 Sampling Strategies 94
4.4 Data Extraction from ODBs 95
4.4.1 Output Database Structure 95
4.4.2 Format of Stress-Strain Dataset 96
4.4.3 Robustness and Error Handling 96
4.5 ANN-Based Regression for Parameter Prediction 97
4.5.1 Motivation for Curve-Based Regression 97
4.5.2 Input and Output Format 97

4.5.3 Training and Validation Logic 98
4.5.4 Comparison to Alternative Strategies 98
4.6 Case Study: J2 Plasticity with Voce Hardening 99
4.6.1 Finite Strain Kinematics 99
4.6.2 Yield Surface and Voce-Type Isotropic Hardening . 101
4.6.3 Numerical Implementation via UMAT 102
4.6.4 Domain Sampling for Training Data Generation . . 102
4.7 ANN Training, Results, and Future Outlook 103
4.7.1 Neural Network Architecture and Input Representation 103
4.7.2 Training Protocol and Data Splitting 104
4.7.3 Performance Metrics and Loss Behavior 104
4.7.4 Curve Reconstruction and Validation 105
4.7.5 Discussion and Future Work 106
5 CONCLUSIONS AND FUTURE WORK 108
5.1 Summary of Contributions 108
5.2 Limitations 109
5.3 Future Directions 109
REFERENCES 123
APPENDICES
A MODEL PARAMETERS 124
A.1 Crystal Plasticity & Modified Chaboche Model 124
A.2 Synthetic Data Generation (Single Crystal Superalloy Dataset) 124
A.3 Synthetic Data Generation (Generic Metal Dataset) 125
B FATIGUE CURVES & GOODMAN DIAGRAMS 126
B.1 Pre-trained Model (Transfer Learning) 126
B.1.1 Synthetic Data Generation 126
B.1.2 Goodman Diagram Results 134
CURRICULUM VITAE 138

LIST OF TABLES

TABLES

Table 2.1 Slip systems commonly observed in FCC crystals. Each slip system is defined by a unique combination of slip direction $\mathbf{m}^s$ and slip plane normal $\mathbf{n}^s$, which govern the plastic deformation mechanisms in single-crystal materials. Data adapted from an open-access source [79]. 26

Table 2.2 Chemical Composition of CMSX-4 (wt%). 30

Table 3.1 Common activation functions used in artificial neural networks. . . . 44

Table 3.2 Training and test losses (MSE) for experimental ANN models. . . . 53

Table 3.3 Validation and test metrics for ANN trained on Chaboche-generated synthetic data. 62

Table 3.4 Uncertainty (standard deviation) of lifetime predictions under input perturbations. 62

Table 3.5 Training and validation performance for the ANN model trained on CMSX-4 Chaboche data. 71

Table 3.6 Training and validation performance for the ANN model trained on Generic Metal synthetic data. 71

Table 3.7 LOOCV validation metrics for the transferred ANN model on CMSX-4 experimental data. 75

Table 3.8 LOOCV validation metrics for transferred model on experimental data (Generic Metal Dataset). 77

Table 3.9 Training and validation performance for the base Model 1 prior to input expansion. 81

Table 3.10 Performance of Model 2 trained on input-expanded CMSX-4 dataset. 84

Table 3.11 Performance of Model 2 trained on input-expanded Generic Metal dataset. 86

Table 4.1 Key commands in user-developed parameter study script for Abaqus 93

Table 4.2 Structure of stress-strain.csv with 4 intervals per simulation. 96

Table 4.3 Validation and test metrics for ANN regression model 104

Table A.1 Parameters of the crystal plasticity model for CMSX-4. 124

Table A.2 Parameters of the modified lifetime assessment model for CMSX-4. 124

Table A.3 Parameters of Chaboche Model used for data generation in Chapter 3. 124

Table A.4 Parameters of Chaboche Model used for data generation in Chapter 3. 125

LIST OF FIGURES

FIGURES

Figure 1.1 Schematic of a turbojet engine [1] 1

Figure 1.2 Schematic of a turbofan engine [4] 2

Figure 2.1 Variable amplitude loading consisting of four separate cycles. . . . 19

Figure 2.2 Illustration of nonlinear damage accumulation for two load levels with different fatigue lifetimes, inspired by the work of [59]. The first load level corresponds to a fatigue life of $N_1 = 10^3$ cycles, and the second load level corresponds to $N_2 = 10^5$ cycles. 22

Figure 2.3 Octahedral (**a**) and cubic (**b**) slip planes of a FCC crystal. 28

Figure 2.4 Demonstration of opening modes of a crack [84]. 28

Figure 2.5 Dimensions of the notched specimen [84]. 30

Figure 2.6 Finite element mesh of the notched specimen. 31

Figure 2.7 Boundary conditions of the FEA model of the notched specimen. . 32

Figure 2.8 Stress in 22-direction (**a**), logarithmic strain in 22-direction (**b**), and lifetime (**c**) contours of a single crystal notch specimen under HCF with R= 0.6 and cut orientation of (100)[001]. 34

Figure 2.9 Fatigue crack initiation at the surface of SC16 nickel-base single crystal with tensile crystal orientation <001> is represented in (**a**). Reproduced with permission from S. Forest, Crystal plasticity and damage at cracks and notches in nickel-base single-crystal superalloys [88]. Lifetime assessment of the same specimen orientations is represented in (**b**), where the minimum lifetime on the FEA model is marked as the predicted crack initiation location. 35

Figure 2.10 Fatigue crack initiation at the surface of SC16 nickel-base single crystal with tensile crystal orientations ⟨011⟩ and ⟨111⟩ is shown in (**a**) and (**c**), respectively. Lifetime assessments of the same specimen orientations are given in (**b**) and (**d**), where the minimum lifetime predicted by the FEA model indicates the expected crack initiation sites. Reproduced with permission from S. Forest, *Crystal Plasticity and Damage at Cracks and Notches in Nickel-Base Single-Crystal Superalloys* [88]. 36

Figure 2.11 Comparison of numerical and experimental results of CMSX-4 notched specimens under HCF loading at 750 °C for $R = 0$. 37

Figure 2.12 Comparison of numerical and experimental results of CMSX-4 notched specimens under HCF loading at 750 °C for $R = 0.6$. 37

Figure 3.1 Structure of feed-forward neural networks (FFNNs) tailored for regression tasks, illustrating the input, hidden, and output layers. 40

Figure 3.2 Workflow integrating experimental and semi-generated obtained from creep model for fatigue model lifetime prediction. 51

Figure 3.3 Creep curve predictions using the trained ANN model. Experimental data points and predicted curves are shown for various temperatures. . . 54

Figure 3.4 Fatigue model predictions versus experimental results on test data. Data includes HCF, and CCF experiments across various R-ratios. 54

Figure 3.5 Synthetic SN curves produced using the Chaboche model for CMSX-4 at 600 °C with various R-ratios. 57

Figure 3.6 Synthetic SN curves produced using the Chaboche model for CMSX-4 at 900 °C with various R-ratios. 57

Figure 3.7 Fatigue curves predicted on synthetic training data for different temperatures and R-ratios. 60

Figure 3.8 Fatigue curves predicted on synthetic training data for varying R-ratios at a fixed temperature. 61

Figure 3.9 Fatigue curves predicted at intermediate temperatures for CMSX-4. 61

Figure 3.10 Schematic representation of the two transfer learning approaches: direct reuse of pretrained architecture (top), and input expansion with appended hidden layers (bottom). 64

Figure 3.11 Ultimate tensile strength (UTS) versus temperature behavior of CMSX-4 single crystal superalloy. The figure is inspired by data trends reported in Sengupta et al. [87]. 66

Figure 3.12 Synthetic SN curves for CMSX-4 at $R = -1$ across 9 temperatures. 67

Figure 3.13 UTS vs. temperature behavior of the Generic Metal Dataset where effective temperature is determined as $400°C$. 68

Figure 3.14 Synthetic SN curves for the Generic Metal Dataset at $R = -1$ across 10 temperatures. 68

Figure 3.15 Predicted vs. validation data for CMSX-4 training. 69

Figure 3.16 Predicted SN curves on Chaboche-generated CMSX-4 training data for $R = -1$. 70

Figure 3.17 Goodman diagram at 10^5 cycles across different temperatures for CMSX-4 training data. 70

Figure 3.18 Predicted vs. validation data for Generic Metal training. 72

Figure 3.19 Predicted SN curves on Chaboche-generated Generic Metal training data for $R = -1$. 72

Figure 3.20 Goodman diagram at 10^5 cycles across different R-ratios for Generic Metal training data. 73

Figure 3.21 Predicted vs. experimental lifetimes on the training set after transfer (Single Crystal Superalloy Dataset). 76

Figure 3.22 Predicted vs. experimental lifetime values for CMSX-4 experimental dataset after transfer. 76

Figure 3.23 Predicted vs. experimental lifetimes on training set after transfer (Generic Metal Dataset). 78

Figure 3.24 Predicted SN curves from transferred model based on experimental data for AISI 4340. 78

Figure 3.25 Input expansion scheme of Model 2. The base model, trained on maximum stress and R-ratio, is reused and combined with the new temperature input at the concatenation stage. The resulting combined tensor is processed through newly added dense layers to learn the expanded input space. 79

Figure 3.26 Synthetic SN curves for the Model 1's Dataset across 20 R Ratios. . 80
Figure 3.27 Predicted vs. validation values for Model 1 across 20 R-ratios. . . . 81
Figure 3.28 SN curves predicted by Model 1 across various R-ratios from training data. 82
Figure 3.29 Goodman diagram at multiple target lifetimes predicted by Model 1. 83
Figure 3.30 Predicted vs. validation values for Model 2 for single crystal dataset. 84
Figure 3.31 SN curves predicted by Model 2 for CMSX-4 training data at $R = -1$. 85
Figure 3.32 Predicted vs. validation values of Model 2 for generic metal dataset. 86
Figure 3.33 SN curves predicted by Model 2 for the Generic Metal Dataset at $R = -1$. 87

Figure 4.1 Overview of the parameter optimization workflow. 91
Figure 4.2 Structure of the Abaqus output database and access flow [130]. . . 95
Figure 4.3 Parameters of Voce type isotropic hardening 101
Figure 4.4 Comparison of true and ANN-reconstructed stress-strain curves using predicted parameters. 105

Figure B.1 Synthetic SN curves for CMSX-4 at $R = -0.2$ across 9 temperatures. 126
Figure B.2 Synthetic SN curves for CMSX-4 at $R = -0.5$ across 9 temperatures. 127
Figure B.3 Synthetic SN curves for CMSX-4 at $R = -0.7$ across 9 temperatures. 127
Figure B.4 Synthetic SN curves for CMSX-4 at $R = 0$ across 9 temperatures. . 128
Figure B.5 Synthetic SN curves for CMSX-4 at $R = -0.3$ across 9 temperatures. 128
Figure B.6 Synthetic SN curves for CMSX-4 at $R = 0.5$ across 9 temperatures. 129
Figure B.7 Synthetic SN curves for CMSX-4 at $R = 0.8$ across 9 temperatures. 129
Figure B.8 Synthetic SN curves for the Generic Metal Dataset at $R = -0.2$ across 10 temperatures. 130
Figure B.9 Synthetic SN curves for the Generic Metal Dataset at $R = -0.5$ across 10 temperatures. 130
Figure B.10 Synthetic SN curves for the Generic Metal Dataset at $R = -0.7$ across 10 temperatures. 131

Figure B.11 Synthetic SN curves for the Generic Metal Dataset at $R = 0$ across 10 temperatures. 131
Figure B.12 Synthetic SN curves for the Generic Metal Dataset at $R = 0.3$ across 10 temperatures. 132
Figure B.13 Synthetic SN curves for the Generic Metal Dataset at $R = 0.5$ across 10 temperatures. 132
Figure B.14 Synthetic SN curves for the Generic Metal Dataset at $R = 0.8$ across 10 temperatures. 133
Figure B.15 Goodman diagrams predicted by the pre-trained model for the single crystal superalloy dataset at $T = 500°C$. 134
Figure B.16 Goodman diagrams predicted by the pre-trained model for the single crystal superalloy dataset at $T = 700°C$. 135
Figure B.17 Goodman diagrams predicted by the pre-trained model for the single crystal superalloy dataset at $T = 800°C$. 135
Figure B.18 Goodman diagrams predicted by the pre-trained model for the single crystal superalloy dataset at $T = 900°C$. 136
Figure B.19 Goodman diagrams predicted by the pre-trained model for the single crystal superalloy dataset at $T = 1000°C$. 136
Figure B.20 Goodman diagrams predicted by the pre-trained model for the single crystal superalloy dataset at $T = 1100°C$. 137

CHAPTER 1

INTRODUCTION

1.1 Background

With the growing demands in aerospace engineering, various types of aero-engines have been developed to meet performance and efficiency requirements. One of the earliest and most fundamental types is the turbojet engine, known for its high-speed capability and relatively simple design. Figure 1.1 illustrates the three major components of a turbojet engine: a compressor, a combustion chamber, and a turbine, all aligned along a common shaft [1].

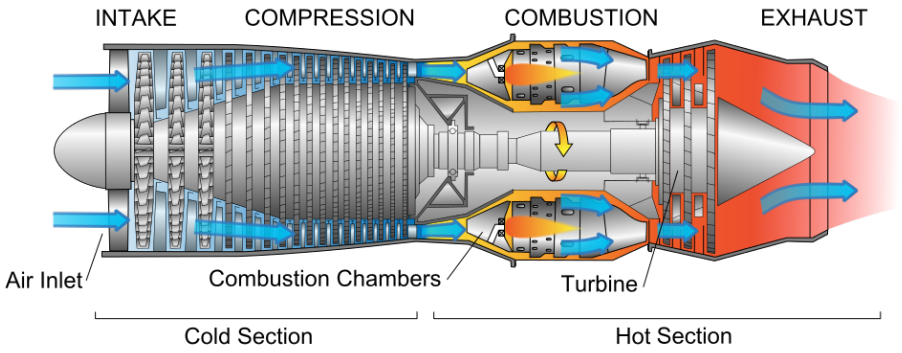

Figure 1.1: Schematic of a turbojet engine [1]

Air enters through the intake and is compressed in stages by a series of rotating and stationary blades within the axial-flow compressor. These blade groups successively increase the pressure and temperature of the air, preparing it for combustion. The high-pressure, high-temperature air then enters the combustion chamber, where fuel is injected and ignited. The resulting hot gas expands rapidly and is expelled through

the turbine, which extracts energy to drive the upstream compressor, and finally exits through the nozzle as a high-velocity jet, generating thrust [2, pp. 4–7].

Turbojets generate all their thrust from this jet flow, without any bypass air. This design enables high speeds but comes at the cost of increased fuel consumption and significant aerodynamic drag, especially as the aircraft approaches transonic speeds. To address the limitations in thrust at high altitudes and speeds, particularly in military applications, afterburners are often added downstream of the turbine. These inject additional fuel into the exhaust stream, which is ignited to produce a secondary combustion phase and boost thrust. However, this dramatically increases fuel consumption and thermal loads, making turbojets suitable primarily for military aircraft where fuel efficiency is less of a constraint [3].

The high thermal and mechanical demands of turbojet operation, especially within the turbine, prompted the evolution toward more efficient alternatives. This led to the development of the turbofan engine, a modified configuration of the turbojet that incorporates a bypass stream to improve fuel economy and reduce noise, particularly for commercial aviation [4].

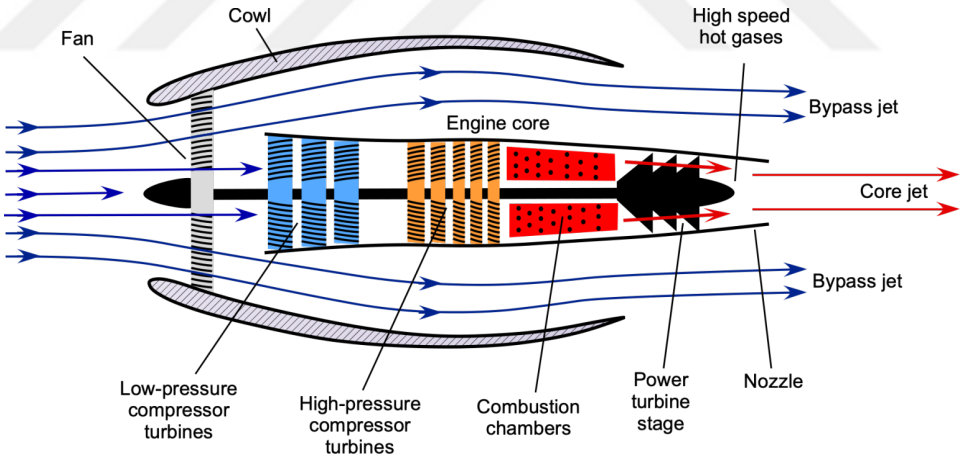

Figure 1.2: Schematic of a turbofan engine [4]

The turbofan engine operates on the same fundamental thermodynamic principles as the turbojet, but incorporates key modifications to improve fuel efficiency and reduce noise. Most notably, a large fan is positioned at the front of the engine, driven by a low-pressure turbine located downstream of the combustion chamber [3]. This configuration divides the airflow into two streams as described in Figure 1.2: one that

passes through the core (high-pressure path, as in a turbojet) and another that bypasses the combustion core entirely, providing additional thrust more efficiently. The low-pressure turbine extracts energy from the exhaust gases to power the fan, while the high-pressure turbine continues to drive the compressor stages upstream. This bypass design allows turbofan engines to generate significant thrust at lower specific fuel consumption, making them the preferred choice for modern commercial aircraft [2, pp. 11–17].

As turbofan engines become more advanced and integrated, so too does the need for accurate lifetime estimation of their components. Safety, efficiency, and cost-effectiveness in long-term operation heavily depend on predicting and managing component degradation. Modern engines are equipped with numerous sensors and on-board diagnostic systems that monitor system health, identify faults, and support predictive maintenance strategies through real-time data acquisition and analysis [5]. Among all the components, turbine blades play a particularly critical role in lifetime prediction. Located in one of the most thermally and mechanically demanding sections of the engine and complex loading conditions. Whether in turbojet or turbofan configurations, accurately assessing the durability of turbine blades is essential for avoiding catastrophic failure and ensuring flight safety [2, pp. 45–57].

1.1.1 Failures in Turbine Blades

Turbine blades operate under extreme thermal and mechanical conditions. Mechanically, blades experience significant centrifugal loads due to high rotational speeds and aerodynamic forces generated by substantial pressure gradients across turbine stages [6]. These blades also confront thermal challenges, often operating near the upper limits of current metallurgical capabilities. Such conditions expose blades to multiple damage mechanisms, including fatigue, creep, corrosion, and thermal degradation [7, 8].

One major failure mechanism for turbine blades is creep, arising from prolonged exposure to high temperatures and stresses. Under normal operating conditions, blades gradually elongate, necessitating regular inspections and adjustments to blade tip clearance. If unchecked, excessive creep can lead to blade tip contact with the sur-

rounding shroud, causing severe mechanical damage [8]. Fatigue failures are often caused by high rotational speed, fast transient start-ups and vibrations due to gas flow resulting in both Low Cycle Fatigue (LCF) and High Cycle Fatigue (HCF) [9, 10]. Additionally, turbine blades frequently encounter complex loading scenarios characterized by simultaneous low-cycle fatigue (LCF) and thermomechanical fatigue (TMF). In these conditions, cyclic mechanical loading interacts synergistically with fluctuating high temperatures, significantly amplifying damage. Consequently, understanding and accurately modeling the creep–fatigue interaction becomes crucial for reliable lifetime prediction and ensuring the structural integrity of turbine blades under realistic operational conditions [11–14].

Corrosion represents another critical failure mode. Operating in aggressive chemical environments, turbine blades are susceptible to oxidation and high-temperature corrosion, often exacerbated by contaminants in the air or fuel. Protective coatings are typically employed to mitigate corrosion damage, yet these coatings can deteriorate under extreme conditions, necessitating frequent inspection and refurbishment [15].

Mechanical damage from foreign object debris (FOD), while primarily affecting compressor blades, can indirectly influence turbine blade integrity. Although foreign objects are generally pulverized by the compressor and combustion processes, smaller particles or fragments of thermal barrier coatings can reach the turbine blades, causing erosion and initiating fatigue cracks [7].

Given these diverse and complex failure mechanisms, turbine blade lifetime assessment is crucial for engine reliability and flight safety. To address the critical issue of creep and enhance overall blade durability, single crystal nickel-based superalloys have emerged as the optimal material choice for turbine blades due to their exceptional resistance to creep at high operating temperatures [16, 17]. Consequently, accurate fatigue lifetime estimation for these single crystal turbine blades has become a priority in modern aviation gas turbine engine management [18].

1.1.2 Single-Crystal Nickel-Based Superalloys

1.1.2.1 Microstructure and Creep Resistance

Single-crystal nickel-based superalloys are principally a two-phase material consisting of a continuous face-centered cubic (FCC) γ matrix reinforced by a high-volume fraction of γ' precipitates. The γ' phase, with its ordered $L1_2$ structure (typically Ni_3Al), comprises approximately 60–70% of the microstructure by volume [19, 20]. These precipitates form a coherent, cuboidal dispersion that impedes dislocation motion, thereby significantly enhancing creep resistance at high temperatures. The elimination of grain boundaries through single-crystal casting further improves performance by removing the pathways for grain boundary sliding and diffusion-driven creep [19].

Nonetheless, creep is not entirely suppressed. At elevated service conditions, dislocations accumulate at γ/γ' interfaces and propagate through the lattice via mechanisms such as precipitate shearing or climb [21, 22]. These dislocation-driven creep processes ultimately control long-term deformation and rupture, making them central to lifetime modeling.

1.1.2.2 Alloy Systems and Applications in Turbine Blades

Nickel-based superalloys constitute a large portion of high-performance gas turbine engines, particularly in the high-pressure turbine section [19]. Among these, CMSX-4 is a widely adopted second-generation single-crystal alloy used in both commercial and military aerospace engines [23]. It includes optimized additions of Re, Ta, Al, W, and Hf to enhance creep and fatigue resistance. The alloy maintains a high fraction of γ' and provides a strong balance between mechanical strength, oxidation resistance, and castability.

First-generation alloys (e.g., PWA 1480) lacked rhenium, while second-generation alloys like CMSX-4 introduced Re to improve high-temperature capabilities. Later third-generation systems further increased Re and added Ru, though at the cost of higher density and greater manufacturing complexity [20].

1.1.2.3 Production and Crystallographic Orientation Effects

Single-crystal blades are produced via directional solidification using a grain selector in a Bridgman furnace to favor the growth of a single [001]-oriented grain [24]. This process suppresses misoriented grains during solidification and aligns the lattice direction with the loading axis of turbine blades.

This orientation is crucial due to the anisotropy of FCC crystals. Creep resistance is maximized along [001] because it promotes uniform shear activation across multiple {111} planes [25]. Deviations from [001] significantly reduce creep life, as demonstrated by orientation-dependent rupture studies.

1.1.2.4 Anisotropic Fatigue and Crack Propagation Behavior

The absence of grain boundaries shifts crack initiation from intergranular sites to defects such as interdendritic pores, carbides, or surface irregularities [21]. In high-cycle fatigue, subsurface pores become critical crack origins due to the lack of surface-breaking inclusions.

Crack growth behavior in single crystals is likewise orientation-dependent. Early propagation follows specific {111} crystallographic planes (Stage I), transitioning to more classical Mode I paths (Stage II) as the crack length and stress intensity increase [26]. This transition complicates fatigue life prediction, requiring anisotropic fracture models.

In summary, single-crystal nickel-based superalloys provide exceptional high temperature mechanical properties due to their carefully engineered microstructure and crystallographic alignment. Their anisotropic behavior and unique failure mechanisms make them indispensable in turbine blade applications, but also demand advanced predictive models for creep and fatigue life. The next chapter explores such modeling frameworks in detail.

1.1.3 Lifetime Assessment Modeling

Fatigue life estimation methods have evolved over decades, reflecting the importance of predicting when a material or component will fail under cyclic loads. Fatigue is one of the most common failure modes in engineering—for instance, around 80% of failures in welded structures are attributed to fatigue damage [27]. Early approaches to life prediction were largely empirical (e.g., Wöhler's S–N curves introduced in the 19th century), but modern methods span a wide spectrum from purely statistical fits to physics-based damage models. An ideal fatigue life model would integrate multiple aspects—combining simplicity, realism, time-dependent damage evolution, microstructural sensitivity, and damage-mechanics correlation [28]. In practice, different frameworks have been developed, each with its own assumptions and application domain. Key approaches to fatigue lifetime modeling include:

1.1.3.1 Stress/Strain-Life (Safe-Life) Methods

These classical approaches use S–N curves (stress–life) for high-cycle fatigue and ε–N curves (strain–life) for low-cycle fatigue to predict the number of cycles to failure. They assume a material can endure a certain cyclic stress or strain range for a given life, independent of crack size. Design codes often employ safety factors on S–N data to ensure a "safe-life." To handle variable loading, the Palmgren–Miner linear damage rule (LDR) is widely applied—it linearly accumulates damage fractions for each load cycle until a total damage of 1 (100%) signals failure [28]. This approach is very easy to use and has been a workhorse in industry, but its limitations are well-documented: real materials show nonlinear damage accumulation and load sequence effects that Miner's rule neglects. For example, a high overload early in the loading history can induce residual stresses or microstructural changes that significantly reduce subsequent fatigue life—a phenomenon the linear rule cannot capture.

1.1.3.2 Fracture Mechanics (Damage-Tolerance) Approaches

Rather than predicting total life directly from cyclic stresses, damage-tolerance methods focus on crack growth behavior. They assume cracks or flaws exist and use crack

propagation laws to predict how many cycles are needed for a crack to grow from an initial size to a critical size. A classic example is the Paris–Erdogan law for stable crack growth in metals, which relates the crack growth rate $\mathrm{d}a/\mathrm{d}N$ to the stress intensity factor range ΔK via a power law [28]. Fracture mechanics is powerful for predicting remaining life in the presence of cracks, and modern computational tools allow crack-growth life predictions even under variable-amplitude loading and residual stress conditions. These methods form the basis of damage-tolerant design, which is crucial in safety-critical parts: components are periodically inspected for cracks, and the design ensures any detected crack will take a sufficient number of cycles to grow to failure.

1.1.3.3 Continuum Damage Mechanics (CDM) Models

In continuum damage mechanics (CDM)-based fatigue modeling, material deterioration is quantified by an internal damage variable (often denoted D) that evolves with each load cycle. This framework treats damage as a continuous degradation of material stiffness or cohesion. A classic formulation was pioneered by Lemaitre, who established thermodynamics-based evolution laws for damage accumulation [28]. Such models link micro-level phenomena (voids, micro-cracks, dislocations) to macro-scale properties like modulus reduction. As micro-cracks form and grow, the bulk elastic stiffness and Poisson's ratio of the material change measurably. The CDM approach is particularly effective for capturing the crack initiation period and has been successfully applied to both high-cycle and low-cycle fatigue [28].

1.1.3.4 Energy-Based and Statistical Methods

Energy-based fatigue models use the dissipated energy per cycle as a damage metric, linking failure to the accumulation of plastic work under cyclic loading. Morrow's pioneering work established that the area within the stress–strain hysteresis loop, a measure of cyclic plastic energy, correlates with fatigue life, providing a unified framework to account for both stress and strain effects [29]. Later developments introduced corrections for loading frequency, temperature, and even multiaxial loading by evaluating cracking energy density on critical planes [30, 31]. Modern energy-

based approaches continue to address the challenges of variable amplitude loading and environmental effects, refining the original models to improve their accuracy and applicability.

Statistical methods, in contrast, address the inherent variability of fatigue life among nominally identical specimens. Probabilistic models, using distributions such as Weibull or log-normal, fit S–N data to quantify the scatter and predict fatigue life at a specified probability of failure [32]. This leads to probability-based S–N (P–S–N) curves, enabling reliability-based design. Foundational work established statistical protocols for fatigue data analysis and the use of extreme-value statistics to describe endurance limits [33]. Recent advances incorporate Bayesian updating and reliability-based optimization, but the core aim remains the quantification and management of uncertainty in fatigue life prediction.

1.1.3.5 Multiaxial and Thermomechanical Fatigue (TMF)

Fatigue life prediction under multiaxial loading requires models that can account for crack nucleation on various planes due to complex stress states. Critical-plane approaches, such as those by Brown and Miller, evaluate both shear and normal strain on the most susceptible planes, while Fatemi–Socie's model introduces normal stress sensitivity for improved predictions under non-proportional loading [34, 35]. Invariant-based criteria, like Crossland's and the Dang Van method, use stress invariants or microscale thresholds for high-cycle fatigue prediction under multiaxial stress [36]. More recent models integrate these concepts with advanced cycle counting and energy-based parameters to address variable amplitude loading.

For thermomechanical fatigue (TMF), methods must simultaneously consider cyclic plasticity, creep, and oxidation, as seen in high-temperature turbine components. Manson's strain-range partitioning was a landmark, dividing each load cycle into plastic and creep contributions [37]. Later, Neu and Sehitoglu combined fatigue, creep, and oxidation damage in a unified cycle-by-cycle framework [38]. Recent developments continue to refine these frameworks, integrating viscoplastic constitutive laws and oxidation-sensitive metrics, yet TMF life prediction remains challenging due to the multitude of interacting factors [39].

1.1.3.6 Machine Learning Based Methods

Machine learning methods, especially artificial neural networks (ANNs), have become a flexible alternative for fatigue life prediction by learning relationships between input features and fatigue life from data, bypassing explicit physics-based rules. Early applications showed that ANNs could reproduce experimental S–N curves and account for factors like stress ratio and fiber orientation in composites [40, 41]. Other ML models, such as support vector machines and decision trees, have also been used for fatigue classification and regression, with the key advantage being their ability to incorporate numerous variables, though large training datasets are often required.

Recently, deep learning techniques have enabled models that process images and load histories (using CNNs and RNNs) [27]. A significant trend is the use of "physics-informed" neural networks, which embed mechanistic constraints (such as S–N curve behavior or damage accumulation) into data-driven models for improved generalization and reduced data needs [42]. These advances are making ML-based fatigue prediction increasingly relevant for complex materials and loading scenarios where conventional models struggle.

1.1.3.7 Physics-Guided and Hybrid Approaches

To overcome the limitations of purely data-driven models, hybrid approaches have emerged. These methods use physics-based simulations (e.g., Chaboche CDM models) to generate synthetic data for ANN training. Transfer learning is then used to fine-tune models on limited experimental data [27]. This enables faster convergence, improved generalization, and credible predictions in complex domains like single-crystal turbine blades. Such hybrid frameworks are central to this thesis.

From early empirical formulas to advanced data-driven methods, lifetime assessment modeling continues to evolve. In this thesis, a hybrid approach is adopted: generating synthetic data via the Chaboche CDM model, training ANNs on this dataset, and applying transfer learning to experimental data. This strategy enables generalizable, accurate predictions for fatigue life in CMSX-4 single-crystal turbine blades.

1.2 Scope and Objectives

This thesis aims to develop a generalized and experimentally transferrable fatigue lifetime prediction framework for aviation-grade single-crystal turbine blades. The work is motivated by the complex thermo-mechanical loading environments experienced by components such as CMSX-4 turbine blades, which are prone to damage mechanisms like low-cycle fatigue (LCF), high-cycle fatigue (HCF), and creep. Due to the high cost and restricted availability of experimental data on single-crystal nickel-based superalloys, particularly in the defense sector, standard data-driven models remain difficult to train and validate.

To address these limitations, this thesis proposes a hybrid modeling strategy that integrates physics-based synthetic data generation with machine learning techniques. Specifically, fatigue lifetime data are generated using the Chaboche continuum damage mechanics (CDM) model and then used to train artificial neural networks (ANNs). These trained models are subsequently adapted to real experimental domains using transfer learning, significantly reducing the need for large-scale experimental datasets while maintaining generalization across loading conditions and materials.

The proposed approach is applied to two distinct datasets:

- A CMSX-4-based synthetic fatigue dataset, used to train the initial base model (Chapter 3),
- Both CMSX-4 and generic metal experimental datasets, used for transfer learning validation with Leave-One-Out Cross-Validation (LOOCV).

In addition to lifetime prediction, a separate ANN-based regression pipeline is developed (Chapter 4) to extract material model parameters from stress-strain curves generated by finite element simulations involving a Voce-type hardening law. This method lays the groundwork for automated material calibration in complex user-defined models.

The primary objectives of this thesis are as follows:

1. To generate synthetic fatigue data for single-crystal nickel-based superalloys using the Chaboche CDM model across a wide range of R ratios, stress amplitudes, and temperatures.
2. To train artificial neural networks (ANNs) using this synthetic data to predict normalized fatigue lifetimes and assess their ability to reproduce generalizable SN curves and Goodman diagrams.
3. To implement and validate a transfer learning strategy that reuses trained ANN layers for prediction on sparse experimental datasets, improving accuracy and reducing overfitting.
4. To compare the transfer learning model performance on CMSX-4 and generic metals, highlighting the ability of the hybrid framework to generalize fatigue behavior beyond training domains.
5. To develop a separate ANN-based pipeline for inverse parameter identification in user-defined material models, predicting constitutive parameters directly from full stress-strain curves.
6. To demonstrate that, despite limited experimental data, combining CDM-based synthetic generation with ANN-based learning enables accurate and flexible fatigue life prediction—laying the foundation for future extensions involving dwell time and HCF-LCF interaction effects.

The outcomes of this research aim to contribute a novel and practical framework for lifetime estimation in critical aerospace components, overcoming data scarcity while leveraging both physics-based understanding and machine learning adaptability.

1.3 Thesis Outline

This thesis is structured into five chapters, each addressing a distinct stage of the proposed fatigue lifetime prediction framework for single-crystal turbine blades and generic metallic materials. A brief overview of each chapter is presented below:

- **Chapter 1 – Introduction:** This chapter provides background on aero-engine operation and failure mechanisms in turbine blades, with a specific focus on single-crystal nickel-based superalloys. It outlines the motivation for fatigue lifetime prediction and introduces various modeling approaches. The chapter concludes with the scope and objectives of the thesis.
- **Chapter 2 – Fatigue Life Modeling with Continuum Damage Mechanics:** This chapter presents a review of continuum damage mechanics (CDM)-based fatigue models, starting with historical developments and continuing through isotropic damage formulations and nonlinear damage accumulation rules. It also introduces modifications for FCC single crystals, describes how stress projection on critical slip systems is performed, and concludes with a finite element application on notched CMSX-4 specimens using a modified Chaboche damage model.
- **Chapter 3 – ANN-Based Lifetime Estimation:** This chapter introduces artificial neural networks (ANNs) for fatigue life prediction. It covers the literature background, ANN fundamentals, and model configurations trained on both experimental and synthetic data. The chapter also describes synthetic data generation via the Chaboche model and the implementation of two transfer learning approaches. The first transfer method directly adapts the base model to experimental data. The second method expands the base model with new inputs such as temperature, enhancing generalization.
- **Chapter 4 – Parameter Optimization with Neural Networks:** This chapter focuses on the inverse identification of material parameters using ANNs. A custom pipeline is introduced, which includes parameterized UMAT simulations in Abaqus, stress-strain data extraction, and regression-based training. A case study is conducted on finite strain J2 plasticity with Voce hardening. The

trained ANN predicts constitutive parameters directly from stress-strain curves, showing the feasibility of this approach for future application to complex material models.

- **Chapter 5 – Conclusions and Future Work:** The final chapter summarizes the key contributions of the thesis, discusses its limitations, and outlines potential future directions. Emphasis is placed on extending the transfer learning models to incorporate additional physical factors such as dwell time and HCF–LCF interactions for more comprehensive lifetime assessment in aviation-grade turbine components.

CHAPTER 2

FATIGUE LIFE MODELING WITH CONTINUUM DAMAGE MECHANICS

2.1 History of CDM-Based Prediction Models

The concept of continuum damage mechanics (CDM) was first introduced in the context of creep failure by Kachanov [43]. Kachanov proposed a damage variable that quantifies the progressive loss of load-bearing material under stress. Physically, this scalar variable represents the fraction of intact material remaining, such that as damage accumulates from 0 (undamaged) toward 1 (fully broken), the effective load-bearing area and stiffness degrade. In creep, Kachanov formulated a kinetic law for the damage variable as a function of stress and time, which provided one of the earliest micromechanically inspired damage laws in engineering.

Building on these ideas, researchers in the 1970s–1980s established a general theoretical foundation for continuum damage in metals. Lemaitre [44] was instrumental in extending CDM beyond creep to more general inelastic processes. His model incorporated thermodynamic and energy dissipation concepts, leading to the development of constitutive relations such as $\sigma = (1 - D)E\varepsilon$ and a damage evolution law derived from energy potentials [44]. Meanwhile, Krajcinovic and Fonseka [45] presented a statistical framework for CDM based on micromechanical observations of crack distributions and defect growth.

As it became evident that damage induces anisotropy in material response, researchers introduced tensorial damage variables. Murakami [46] and Cordebois and Sidoroff [47] developed second-rank damage tensors to describe direction-dependent stiffness loss, giving rise to anisotropic CDM formulations. Further, Chow and Wang [48] introduced damage evolution laws that accounted for multiaxiality, plasticity, and stress state parameters.

Simultaneously, coupling damage with plasticity became essential to capture realistic behavior in metals. Coupled elastoplastic-damage models by Lemaitre [44] and later by Chandrakanth and Pandey [49] introduced damage evolution laws driven by plastic strain or plastic energy release. Other authors such as Neu and Sehitoglu [38] emphasized thermodynamically consistent formulations incorporating coupled softening.

The integration of CDM into fatigue modeling began in the late 1980s. Chaboche and Lesne [50] proposed a non-linear fatigue damage accumulation law within the CDM framework, accounting for load sequences and micro/macro crack growth separation. This model served as a foundational reference for subsequent CDM-based fatigue life models such as those by Liu and Mahadevan [51] and Xiao et al. [52], who adapted the CDM framework for multiaxial and high-cycle fatigue scenarios.

Later contributions included numerical implementations of CDM-based fatigue, such as the finite-element model by De Jesus et. al. [53], which embeds damage variables within an explicit finite-element framework to simulate stiffness degradation and crack initiation in pressure vessel-like structures. This work advanced CDM's application from analytical models to practical, spatially-resolved fatigue predictions.

Later developments include nonlocal damage models, probabilistic extensions [54], and anisotropic models for composite materials [55]. Today, CDM-based models are widely applied to simulate fatigue and failure in metallic materials and serve as a robust alternative to purely empirical life prediction laws.

2.2 Isotropic Fatigue Damage Model

In typical metallic fatigue studies, cyclic loading is administered slowly enough that dynamic effects are negligible. This defines the quasi-static loading regime, within which inertial forces and rate-dependent behaviors do not significantly influence material response. Furthermore, fatigue-safe design and experiment usually operate under small-strain (infinitesimal strain) conditions, where total deformations are minimal enough to assume the undeformed and deformed configurations remain geometrically similar. Under quasi-static cyclic loading and elastic-plastic behavior at small strains, the damage accumulates predictably and can be quantified directly through a scalar variable. This approach enables incremental, cycle-by-cycle tracking of material degradation, simplifying the ensuing constitutive model [56–58].

Lemaitre and Chaboche [59] first formalized a scalar damage variable, D, that grows with the cyclic load's stress amplitude, σ_{amp}, and mean stress, as respresented in Equation 2.1. In their framework, fatigue degradation is driven by the reduction of the material's effective load-bearing area, so that the constitutive response scales with the undamaged fraction. For isotropic multiaxial loading, the uniaxial amplitudes in the original law are replaced by an equivalent critical stress, most commonly the von Mises and maximum principle stress measures, ensuring that contributions from all principal directions are captured in a single invariant. This substitution preserves the thermodynamic form of the evolution equation while extending the model's applicability to complex service spectra encountered in turbine disks, crankshafts, and other three-dimensional components.

$$\delta D = f(\sigma^*_{amp}, \sigma^*_{mean})\, \delta N \tag{2.1}$$

where D is the scalar variable representing fatigue damage evolution from the virgin state ($D = 0$) up to fatigue fracture ($D = 1$) and σ^* represents the multiaxial stress definition most appropriate to the case at hand. The differential equation of the fatigue damage on the dominant cleavage plane is expressed as:

$$\delta D = \left[1 - (1 - D)^{\beta+1}\right]^{\alpha(\sigma^*_{amp}, \sigma^*_{mean})} \left[\frac{\sigma^*_{amp}}{M(\sigma^*_{mean})(1 - D)}\right]^{\beta} \delta N \tag{2.2}$$

where β is a temperature-dependent model parameter.

The function α represents the effects of nonlinear accumulation:

$$\alpha(\sigma^*_{amp}, \sigma^*_{mean}) = 1 - a\left\langle \frac{\sigma^*_{amp} - \sigma_l(\sigma^*_{mean})}{\sigma^*_{uts} - \sigma^*_{max}} \right\rangle \tag{2.3}$$

where a is a model parameter, σ_{uts} is the ultimate tensile stress, and σ_l is the fatigue limit in terms of amplitude stress. The relation between fatigue limit and mean stress is represented by Goodman's linear relation:

$$\sigma^*_l = \sigma^*_{l_0}(1 - b_1\sigma^*_{mean}) \tag{2.4}$$

where σ_{l_0} is the fatigue limit at zero mean stress i.e., endurance limit, and b_1 is the model parameter establishing the relation between fatigue limit and mean stress. M is expressed with the same linear relation dependent on mean stress and model parameters b_2 and M_0 as

$$M = M_0(1 - b_2\sigma^*_{mean}) \tag{2.5}$$

Fatigue life, N_f, of a material is determined by integrating the damage variable, D, in Equation (2.2) from 0 to 1 since $D = 1$ represents the fatigue failure of a virgin material.

$$N_f = \frac{1}{(\beta + 1)[1 - \alpha(\sigma^*_{amp}, \sigma^*_{mean})]}\left[\frac{\sigma^*_{amp}}{M(\sigma^*_{mean})}\right]^{-\beta} \tag{2.6}$$

2.2.1 Variable Amplitude Loading

Variable-amplitude loading describes any fatigue load history in which the peak-to-peak stress (or strain) and mean stress vary from cycle to cycle instead of remaining constant. In service, whether it is an aircraft climb-cruise-descent sequence, a turbine ramp-hold-shutdown, or a road-load spectrum, components rarely experience the perfectly repetitive, fully reversed waveform used in standard S–N tests. Instead, they see a succession of overloads, under-loads, dwell periods, and intermediate excursions that interact in non-linear ways to drive damage.

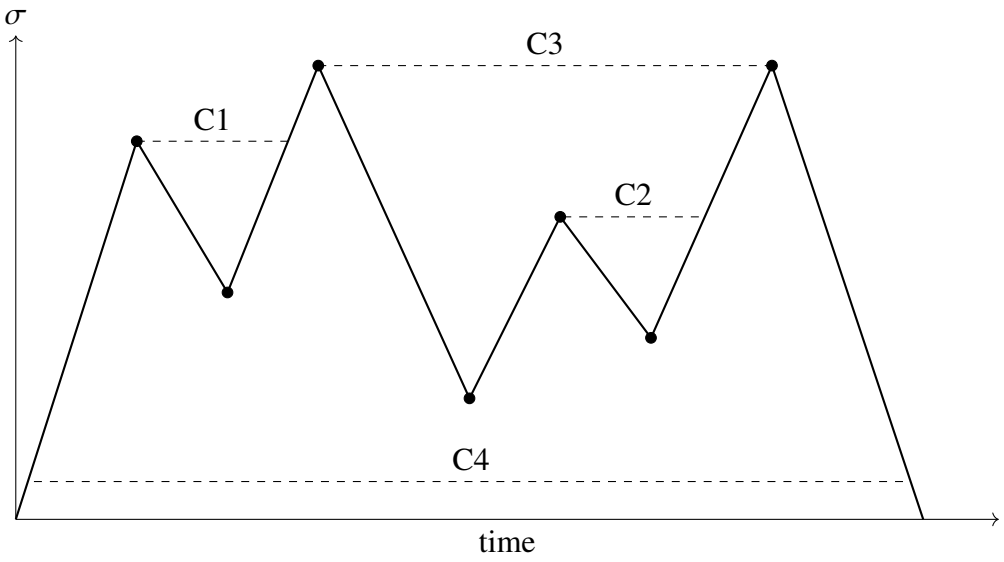

Figure 2.1: Variable amplitude loading consisting of four separate cycles.

The variable amplitude loading history illustrated in Figure 2.1 consists of multiple cyclic segments occurring sequentially, where C1, C2, C3 and C4 represent four distinct cycles extracted from the original stress–time signal. Each of these cycles is characterized by its own stress amplitude and mean stress, both of which contribute to the overall fatigue damage. Among them, cycles with the highest amplitudes, such as C3 and C4 in this case, tend to dominate fatigue life consumption due to the nonlinear nature of damage accumulation. Additionally, the short horizontal plateaus visible in the signal correspond to dwell periods, which can further accelerate damage accumulation through creep-fatigue interaction, particularly in high-temperature applications.

To analyze such complex loading sequences, cycle counting algorithms are employed to extract the individual closed cycles and define their amplitude and mean stress. In this study, the **three-point rainflow algorithm** is used to perform the decomposition. The rainflow cycle-counting method was introduced by Matsuishi and Endo in 1968 to extract equivalent fatigue cycles from arbitrary stress–time histories [60]. Downing and Socie [61] later formalized the efficient three-point variant, which balances accuracy with computational simplicity and is recognized as mathematically equivalent to the classical four-point (ASTM E1049) implementation [62, 63].

The pioneering practical implementation, including detailed FORTRAN routines for both three- and four-point rainflow counting, was published by Cheng and Broz [64], providing a foundational tool for processing random load histories in fatigue analysis.

The algorithm carried out by, initially, reducing the recorded stress history $\sigma(t)$ to a sequence of local extrema via peak-valley filtering:

$$\{X_1, X_2, \ldots, X_N\} \quad X_i = \sigma(t_i) \quad t_1 < t_2 < \cdots < t_N \tag{2.7}$$

Then, for each sliding triplet (X_{n-2}, X_{n-1}, X_n), the stress ranges are computed as

$$R_{\text{prev}} = |X_{n-2} - X_{n-1}| \quad R = |X_{n-1} - X_n| \tag{2.8}$$

A closed cycle is identified when the following condition is satisfied

$$R \leq R_{\text{prev}} \tag{2.9}$$

Once a cycle is detected, its amplitude and mean stress are calculated as

$$\sigma_a = \frac{1}{2}R \qquad \sigma_m = \frac{1}{2}(X_{n-1} + X_n) \tag{2.10}$$

The point X_{n-1} is removed from the sequence, and the window continues scanning. This process repeats until all valid cycles are extracted. Any remaining unpaired points in the sequence are treated as half cycles and included in the cumulative damage assessment [65].

The algorithm mirrors the energy dissipation seen in material hysteresis by consistently peeling off smaller embedded cycles first. McInnes and Meehan [63] showed that the three-point algorithm generates the same cycle set as the four-point algorithm, despite possible differences in cycle order. Its low memory usage, requiring only three points at any given time, makes it highly effective for fatigue evaluation in large finite element datasets, as utilized in this study.

2.2.2 Nonlinear Damage Accumulation

Nonlinear cumulative damage models have been developed because linear damage rules (like Miner's) often fail under variable-amplitude loading, particularly when load sequence and history effects are significant [66]. Among nonlinear approaches, fracture mechanics, continuum-damage methods, and life-curve (damage-curve) techniques provide varying levels of complexity and physical fidelity. For this study, life-curve methods were selected due to their ease of implementation, insensitivity to stress-state dimensionality, and compatibility with fatigue parameters—making them ideal for the problem at hand [67].

The baseline is the Palmgren–Miner rule, which assumes linear superposition of damage:

$$D = \sum_i \frac{n_i}{N_i} \tag{2.11}$$

While Miner's rule is simple and widely used, experimental results show life predictions ranging from 0.7 to 2.2 of actual life under constant uniaxial loading, and even lower (e.g., 0.19) under complex biaxial spectra [68]. Its critical flaw is the inability to model cycle-order effects or cumulative interactions between high and low-cycle blocks. To mitigate these shortcomings, Manson introduced the Double Linear Damage Rule, which splits the damage curve into two linear segments with a "kneepoint" indicating the transition between low-cycle fatigue and high-cycle fatigue behavior [69]. One then applies Miner's rule separately within each region. Locating this kneepoint and calibrating its slope requires specialized block-loading experiments, as detailed by Manson and Halford [70]. This method allows for a more accurate yet still relatively straightforward application across multiple load blocks.

One of the earliest attempts to improve fatigue failure prediction through nonlinear damage modeling was introduced by Richart and Newmark in 1948 [71]. Rather than relying on a linear damage line, they proposed a continuous damage curve that more accurately reflects the evolution of damage under cyclic loading. This model, later termed the Damage Curve Approach (DCA), was based on the observation that low-amplitude, high-cycle loadings do not immediately initiate damage. Instead, a substantial number of cycles must accumulate before the damage rate increases sig-

nificantly. Once this threshold is passed, damage progresses at an accelerating rate, quickly leading to failure. In contrast, high-amplitude, low-cycle loading produces less of this delayed behavior.

To overcome the limitations of linear damage summation, Chaboche applied a nonlinear extension of the Damage Curve Approach (DCA), originally based on the work of Richart and Newmark and later developed by Manson and Halford. In this framework, the damage evolution is nonlinear with respect to the number of cycles and varies depending on the load level.

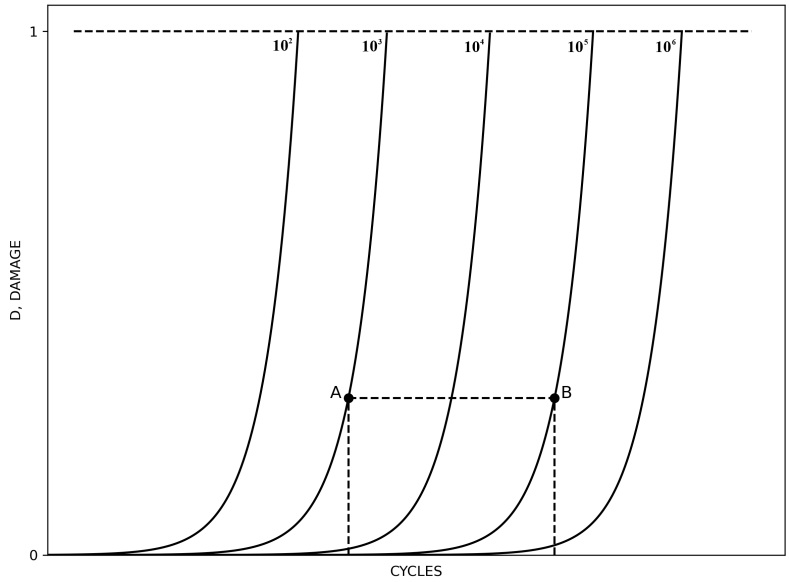

Figure 2.2: Illustration of nonlinear damage accumulation for two load levels with different fatigue lifetimes, inspired by the work of [59]. The first load level corresponds to a fatigue life of $N_1 = 10^3$ cycles, and the second load level corresponds to $N_2 = 10^5$ cycles.

Chaboche introduced a method of damage accumulation between two load levels by projecting the damage at an intermediate point onto a new damage curve. As illustrated in Figure 2.2, the transition from point A to point B allows for cumulative damage to be calculated using the following relation:

$$\frac{N_2}{N_{F_2}} = 1 - \left(\frac{N_1}{N_{F_1}}\right)^{\eta} \qquad \text{with} \qquad \eta = \frac{1-\alpha_2}{1-\alpha_1} \tag{2.12}$$

Here, N_1 and N_2 represent the number of cycles at respective load levels, and N_{F_1}, N_{F_2} are their corresponding fatigue lives under constant amplitude. The exponent η captures the interaction between the two levels, incorporating the material parameters α_1 and α_2.

This formulation enables a more accurate, sequence-dependent evaluation of damage by transitioning across damage curves. Lemaitre and Chaboche later embedded this idea into a thermodynamic damage framework, allowing fatigue damage computed with Equation 2.2 to evolve consistently with internal variables and mechanical behavior. The generalized version of nonlinear damage accumulation as follows:

$$D = \left[\left(\left(\frac{n_1}{N_{f_1}}\right)^{\eta_{12}} + \frac{n_2}{N_{f_2}}\right)^{\eta_{23}} + \cdots + \frac{n_{i-1}}{N_{f_{i-1}}}\right]^{\eta_{i,i+1}} + \frac{n_i}{N_{f_i}} \tag{2.13}$$

A primary advantage of the DCA is that it requires only one set of damage curves to represent a range of life levels. The linear damage line is treated as a baseline, used to establish the material constant, while all other curves are generated by shifting from this reference.

2.3 Extension to FCC Single-Crystal Superalloys

Fatigue life prediction in single crystal materials has been extensively studied from multiple perspectives. Experimental work by [34] demonstrated that, under multiaxial loading, fatigue crack initiation and propagation predominantly occur along preferred slip planes. This observation has led to the development of various prediction models, including probabilistic critical plane approaches and adapted isotropic formulations designed to incorporate multiaxial anisotropy [17, 72–74]. These models typically focus on resolved shear stress on critical planes, as it is well established that fatigue cracks tend to initiate along crystallographic directions governed by shear strain [34]. Following initiation, crack propagation continues along paths aligned with the direction of maximum shear strain. It is worth noting, however, that the directions of maximum stress and shear strain may not coincide, as they are strongly influenced by the material's crystallographic orientation. In this chapter small strain crystal plasticity model is post-processed with Chaboche fatigue damage law where multiaxial stress

is determined as the opening mode of the most dominant slip systems to capture the anisotropy specific to FCC single crystals.

2.3.1 Small Strain Crystal Plasticity

This section outlines the constitutive framework of the single-crystal plasticity model, which builds upon the crystallographic formulation originally proposed by Cailletaud [75]. The model operates at the mesoscale range (10^{-7} m to 10^{-4} m) and describes the behavior of dislocation motion and latent interactions across individual slip systems. At this scale, the model captures the localized plastic deformation occurring specifically on the active slip systems. Although it does not directly resolve the macroscopic strain response, the cumulative effect of micro-level plasticity—governed by both material orientation and loading direction—leads to an averaged macroscopic stress–strain response [76]. The model is designed to simulate the anisotropic, rate-dependent plastic behavior of nickel-based superalloys under small strain conditions. In this context, the linear strain tensor is defined as $\boldsymbol{\varepsilon} = \mathrm{sym}[\nabla \mathbf{u}]$, representing the symmetric part of the displacement gradient.

Due to the small-deformation assumption, an additive decomposition of strain is employed.

$$\boldsymbol{\varepsilon} = \boldsymbol{\varepsilon}^e + \boldsymbol{\varepsilon}^p \tag{2.14}$$

where $\boldsymbol{\varepsilon}^e$ denotes the elastic strain tensor and $\boldsymbol{\varepsilon}^p$ represents the plastic strain component. The relationship between the Cauchy stress $\boldsymbol{\sigma}$ and the elastic strain is defined by the constitutive state law:

$$\boldsymbol{\sigma} = \mathbf{C} : \boldsymbol{\varepsilon}^e \tag{2.15}$$

where $\mathbf{C}$ is the fourth-order elasticity tensor. Since the material under investigation possesses a face-centered cubic (FCC) crystal structure, it exhibits cubic elastic symmetry. As a result, the elasticity tensor $\mathbf{C}$ is defined by only three independent elastic constants: C_{11}, C_{12}, and C_{44}, as shown below.

$$\mathbf{C} = \begin{bmatrix} C_{11} & C_{12} & C_{12} & 0 & 0 & 0 \\ C_{12} & C_{11} & C_{12} & 0 & 0 & 0 \\ C_{12} & C_{12} & C_{11} & 0 & 0 & 0 \\ 0 & 0 & 0 & C_{44} & 0 & 0 \\ 0 & 0 & 0 & 0 & C_{44} & 0 \\ 0 & 0 & 0 & 0 & 0 & C_{44} \end{bmatrix} \quad \text{where} \quad \begin{aligned} C_{11} &= \frac{1}{3}(3K + 4\mu) \\ C_{12} &= \frac{1}{3}(3K - 2\mu) \\ C_{44} &= \mu + \mu' \end{aligned} \tag{2.16}$$

where K is the bulk modulus, μ is the shear modulus, and μ' is the effective shear modulus characterizing shear resistance along specific crystallographic directions [77]. An additional state law can be introduced to describe the isotropic hardening behavior of each slip system:

$$r^s = q \sum_{s=1}^{N} h^{sr} \rho^s \tag{2.17}$$

where q is a material constant associated with isotropic hardening, s denotes the slip system, and N is the total number of slip systems considered in the crystal structure. The term h^{sr} represents the interaction matrix that governs both self- and latent hardening, capturing the interactions among the N slip systems.

For single-crystal Ni-based superalloys, it is common in the literature to assume h^{sr} as the identity matrix, given the minimal influence of latent hardening in these materials [78]. This reflects the crystallographic characteristics of Ni-based superalloys, where cross-hardening between slip systems is generally negligible compared to self-hardening on each slip system. The variable ρ^s corresponds to the dislocation density on slip system s, which serves as a key internal variable describing the evolving microstructure during plastic deformation. In the present formulation, the dislocation density evolves according to a nonlinear isotropic hardening law, given by:

$$\rho^s = 1 - \exp(-b\,|\gamma^s|) \tag{2.18}$$

where b is a material parameter that controls the saturation rate of dislocation density with respect to accumulated plastic slip. Accordingly, the hardening variable r^s is defined as:

$$r^s = q \sum_{s=1}^{N} (1 - \exp(-b\,|\gamma^s|)) \tag{2.19}$$

where q is the hardening modulus and N is the total number of slip systems. The plastic slip γ^s for each slip system is determined by the resolved shear stress through Schmid's law. The Schmid criterion, which serves as a physically-based yield function for each slip system, can be written as:

$$f^s = |\tau^s| - r^s \quad and \quad \tau^s = \boldsymbol{\sigma} : (\mathbf{m}^s \otimes \mathbf{n}^s) \tag{2.20}$$

Here, τ^s denotes the resolved shear stress on slip system s, acting as the primary driving force for plastic slip. Plastic deformation is activated on a given slip system when the resolved shear stress exceeds the critical threshold determined by the hardening variable r^s. Thus, Schmid's law effectively functions as a multimechanism yield criterion at the crystal level. The resolved shear stress is computed as described in Equation 2.20, where $\mathbf{m}^s$ is the slip direction and $\mathbf{n}^s$ is the slip plane normal for slip system s. This tensorial representation enables explicit incorporation of crystallographic orientation and material anisotropy. The full set of slip directions and slip plane normals for FCC crystals is listed in Table 2.1.

Table 2.1: Slip systems commonly observed in FCC crystals. Each slip system is defined by a unique combination of slip direction $\mathbf{m}^s$ and slip plane normal $\mathbf{n}^s$, which govern the plastic deformation mechanisms in single-crystal materials. Data adapted from an open-access source [79].

Slip System Family	**System s**	**Slip Normal $\mathbf{n}^s$**	**Slip Direction $\mathbf{m}^s$**
Octahedral	1	(111)	$[\bar{1}01]$
	2		$[0\bar{1}1]$
	3		$[\bar{1}10]$
	4	$(1\bar{1}1)$	$[\bar{1}01]$
	5		[011]
	6		[110]
	7	$(\bar{1}11)$	$[0\bar{1}1]$
	8		[110]
	9		[101]
	10	$(11\bar{1})$	$[\bar{1}10]$
	11		[101]
	12		[011]
Cubic	1	(001)	$[\bar{1}10]$
	2		[110]
	3	(100)	[011]
	4		$[0\bar{1}1]$
	5	(010)	$[\bar{1}01]$
	6		[101]

According to the principle of maximum energy dissipation, the plastic strain rate tensor can be expressed as:

$$\dot{\boldsymbol{\varepsilon}}^p = \sum_{s=1}^{N} \dot{\gamma}^s (\mathbf{m}^s \otimes \mathbf{n}^s) \tag{2.21}$$

where $\dot{\gamma}^s$ denotes the plastic slip rate on slip system s, and the dyadic product $\mathbf{m}^s \otimes \mathbf{n}^s$ defines the contribution of that system to the overall plastic strain. The evolution of the slip rate is governed by a threshold-type Norton flow rule, given by:

$$\dot{\gamma}^s = \left\langle \frac{|\tau^s| - r^s}{K} \right\rangle^n \operatorname{sign}(\tau^s - r^s) \tag{2.22}$$

where K acts as a slip resistance parameter (threshold), n is the rate-sensitivity exponent, τ^s is the resolved shear stress, and r^s is the current strength of slip system s. The Macaulay brackets $\langle \cdot \rangle$ ensure that slip occurs only when the driving force exceeds the threshold.

2.3.2 Critical Stress Determination

Accurately estimating fatigue life requires selecting an appropriate equivalent stress measure that reflects both the material characteristics and the complexity of the loading condition, particularly in cases involving triaxial stress states or intricate geometries. For most metallic materials, maximum principal stress or von Mises stress are commonly used and generally yield reliable results under multiaxial loading. However, in the case of single crystals, it is more appropriate to incorporate slip system information in the definition of equivalent stress, as this allows the anisotropic mechanical response across various crystallographic orientations to be properly captured.

FCC single crystals exhibit four active octahedral slip planes and three active cubic slip planes, as illustrated in Figure 2.3. While octahedral slip systems remain active even at room temperature due to their closely packed atomic arrangement, cubic slip systems typically require higher activation energies and thus become active only at elevated temperatures. Since fatigue fracture tends to initiate and propagate along active slip planes, the stress acting in the cleavage directions of these planes is considered a critical factor in determining fatigue life.

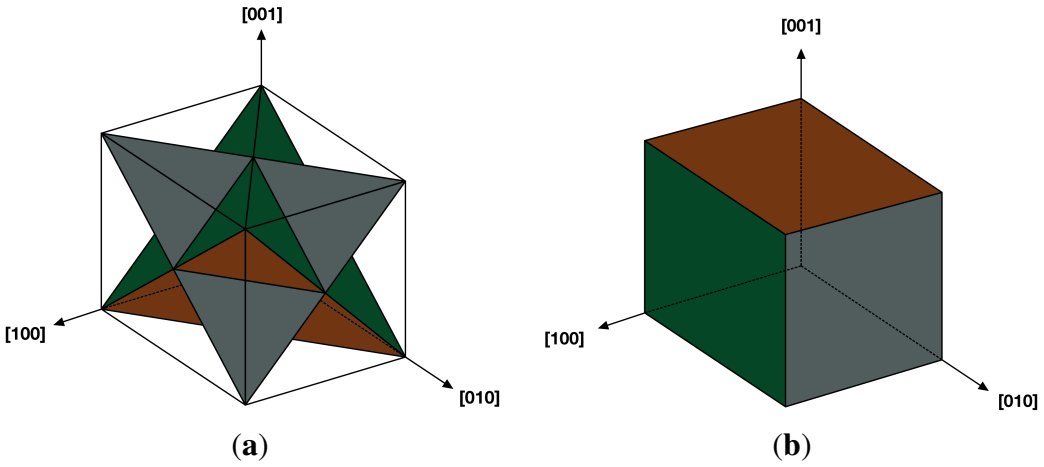

Figure 2.3: Octahedral (**a**) and cubic (**b**) slip planes of a FCC crystal.

Experimental investigations have demonstrated that mixed-mode loading is commonly observed in multiaxial fatigue fractures across various specimen geometries and loading configurations. As shown in Figure 2.4, crack opening behaviors can be categorized into different modes: Mode I corresponds to cleavage systems, while Modes II and III represent accommodation systems. Among these, Mode I is consistently dominant, even under pure shear loading, due to the fact that the manifestation of shear (Mode II) and tearing (Mode III) depends significantly on crack orientation and crystallographic texture [80, 81].

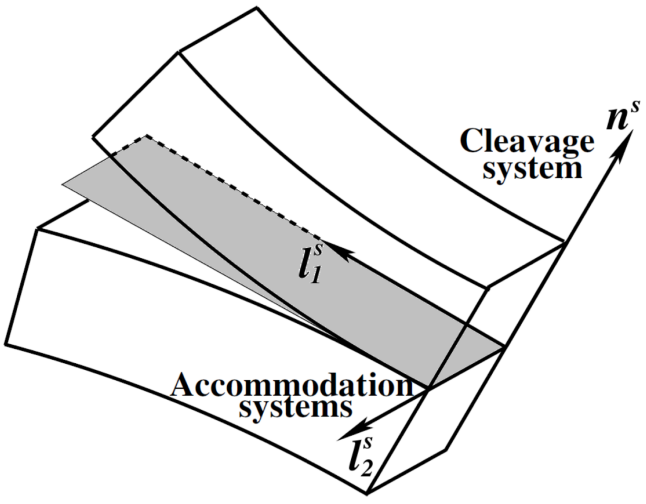

Figure 2.4: Demonstration of opening modes of a crack [84].

The cleavage system remains active in all cases, whereas the activation of accommodation systems is influenced by the specific nature of the fatigue loading. Consequently, the propagation of fatigue micro-cracks is more strongly governed by cleavage systems than by the other modes [82, 83]. Based on these findings, the critical stress for fatigue life estimation is defined as the cleavage stress acting on the slip planes where cracks are most likely to initiate.

In this chapter, the cleavage stress is determined by projecting the nominal stress tensor onto the normal vector of the (111) slip plane, which is the primary plane on which plastic deformation occurs in FCC single crystals. Given that slip in these materials typically develops along the [110] directions within the (111) planes, the Mode I opening stress, representing crack normal separation, is assumed to act along the [111] direction. Therefore, the resolved cleavage stress is computed as the normal component of the applied stress on the most critically oriented (111) plane, corresponding to the dominant fracture path under fatigue loading.

2.4 Fatigue Life Prediction on Notched Specimen

The high-cycle fatigue (HCF) test data and notched specimen geometry utilized in this study are adopted from Aslan [84], where detailed information on CMSX-4 specimen preparation, tensile testing, and fatigue experiments under various load ratios (R) is provided as part of the PREMECCY project. Comprehensive descriptions of the testing protocols, including specimen machining, environmental conditions, and failure criteria, can be found in [84].

The notched specimen geometry and corresponding cyclic loading amplitudes from that study were employed in the present work to replicate the experimental conditions and to calibrate the material behavior in simulations.

2.4.1 Material and Specimen Geometry

The second-generation nickel-based single crystal superalloy CMSX-4, whose chemical composition (in wt%) is provided in Table 2.2, was subjected to solution treatment followed by rapid cooling in order to promote the formation of a high volume fraction of γ' precipitates, approximately 70%, which serve as the primary strengthening phase within the alloy.

Table 2.2: Chemical Composition of CMSX-4 (wt%).

Ni	Cr	Co	Mo	W	Al	Ti	Ta	Re	Hf
61.8	6.5	9	0.6	6	5.6	1	6.5	3	0.1

Notched specimens oriented along the (100)[001] crystallographic direction were subjected to cyclic tensile loading at stress ratios of $R = 0$ and $R = 0.6$, using a test frequency of 118 Hz at an elevated temperature of 750 °C. The geometry of the notched specimen, including a notch thickness of 1.6 mm, is illustrated in Figure 2.5. Due to the localized stress concentration introduced by the notch, which varies based on both the notch radius and thickness, fatigue life is more accurately correlated with the maximum stress at the notch root rather than the nominal applied stress. This approach offers a more generalized representation of fracture behavior across different notched geometries.

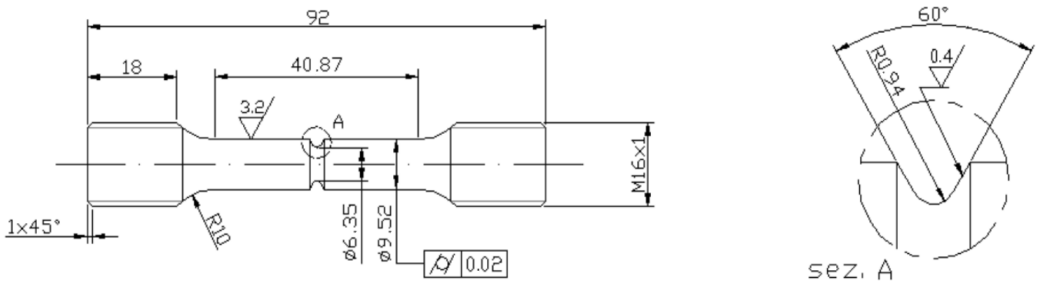

Figure 2.5: Dimensions of the notched specimen [84].

2.4.2 Finite Element Model of the Nothced Specimen

The finite element model corresponding to the notched specimen shown in Figure 2.5 was developed in Abaqus/CAE 2018 using quadratic axisymmetric elements (CAX8). The mesh configuration generated for the simulation is illustrated in Figure 2.6a. The anisotropic material response of the single crystal was modeled using the small strain crystal plasticity formulation described in Section 2.3.1, implemented through a user-defined material subroutine (UMAT).

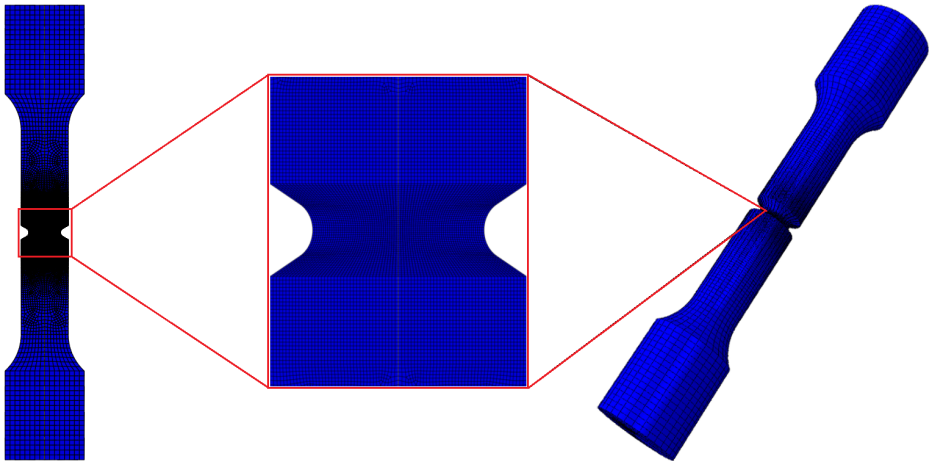

Figure 2.6: Finite element mesh of the notched specimen.

With regard to mesh sensitivity, the inclusion of rate-dependent behavior in the constitutive model contributes to the smoothing of deformation gradients, thereby mitigating sharp localizations commonly encountered in conventional elasto-plastic analyses. Additionally, the absence of material softening in the model helps to suppress plastic strain localization, further reducing sensitivity to mesh refinement [85, 86].

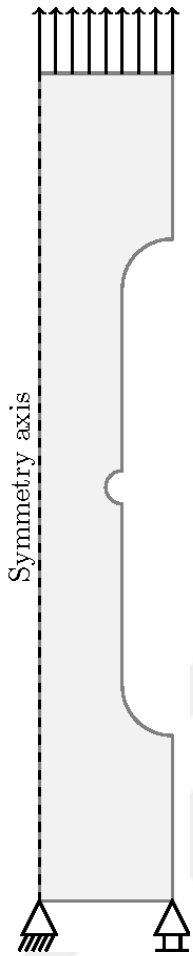

Figure 2.7: Boundary conditions of the FEA model of the notched specimen.

The boundary conditions applied in the simulation are defined as follows: the bottom edge of the specimen is constrained in the *y*-direction, while the left edge is treated as a symmetry boundary due to the axisymmetric nature of the model. A cyclic force amplitude is applied to the top surface to represent the experimental loading conditions, as illustrated in Figure 2.7.

2.4.3 Post-Scripting of Modified Chaboche Model

The stress histories at each integration point were extracted from the output database (ODB) of the single crystal plasticity simulation using Abaqus post-processing scripts written in Python 2.7. The extraction procedure relied on the odbAccess module for reading simulation results, the abaqusConstants module for specifying locations such as integration points, and the visualization module to support data inspection

and analysis. For each analysis frame, the stress tensor components (S, SDV) at all integration points, as well as the nodal displacement values (U), were retrieved to reconstruct the cyclic loading histories and monitor nodal movements over time.

From these stress histories, a peak–valley detection algorithm was applied to identify the maximum and minimum stress values for each cycle. These extrema were then used to calculate the corresponding stress amplitudes and mean stresses both of which serve as input parameters for the modified Chaboche fatigue model. Using the multiaxial anisotropic fatigue life prediction method introduced in this chapter, the fatigue lifetime was estimated at each nodal location. The resulting lifetime data, along with mesh information from the finite element model, were exported in Visualization Toolkit (.vtk) format. These files were subsequently used to generate spatial fatigue lifetime contours via ParaView, an open-source scientific visualization platform.

2.4.4 Results and Discussion

The plastic slip threshold parameter K and the rate sensitivity exponent n were calibrated to reproduce the stress–strain response of CMSX-4 at 750 °C. The elastic stiffness constants used for CMSX-4 were adopted from the literature [89], and are summarized in Table A.1 (Appendix A).

The temperature-dependent material parameters used in the lifetime assessment model including yield strength (σ_{yield}) and ultimate tensile strength (σ_{uts}), for CMSX-4 at 600 °C, 750 °C, and 900 °C were obtained from literature [87]. The amplitude and mean stress values were derived from high-cycle fatigue (HCF) test data, and the temperature-dependent model parameters were calibrated accordingly to ensure accurate lifetime predictions for both $R = 0$ and $R = 0.6$ cases.

The parameter set used for both the crystal plasticity model and the fatigue lifetime estimation model is provided in Table A.2 (Appendix A). Since CMSX-4, due to its FCC microstructure, does not exhibit a true fatigue limit, the endurance limit (σ_{l_0}) was taken as zero. This avoids assigning an arbitrary cycle threshold for infinite life and instead allows for clearer visualization of lifetime distributions throughout the specimen. Consequently, the parameter b_1, which relates to the fatigue limit at varying

mean stresses, becomes irrelevant and is omitted. The remaining parameters were manually fitted to match the available experimental data, which includes at most two *R*-ratios per temperature. Optimization techniques such as gradient descent or genetic algorithms were not employed, as they did not offer a notable improvement in this specific case.

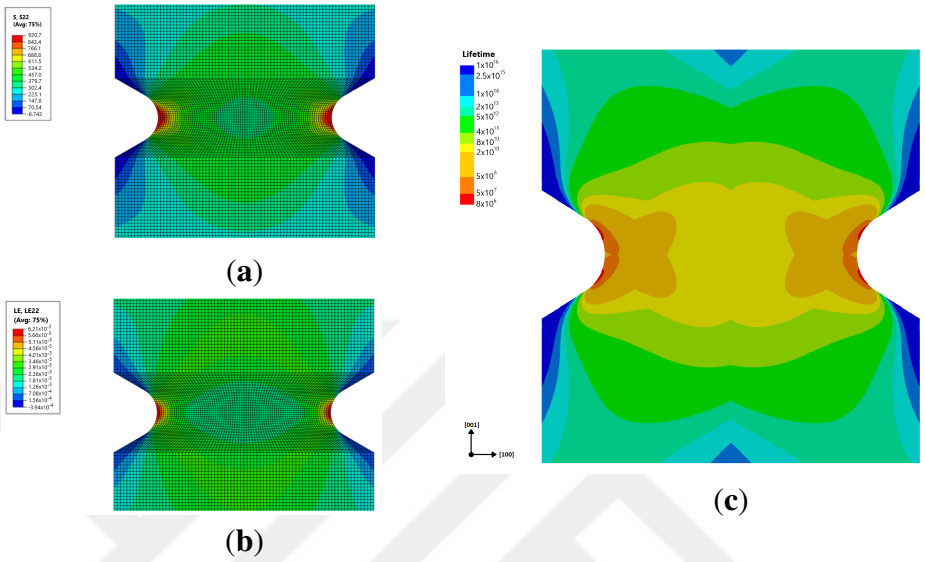

Figure 2.8: Stress in 22-direction (**a**), logarithmic strain in 22-direction (**b**), and lifetime (**c**) contours of a single crystal notch specimen under HCF with R= 0.6 and cut orientation of (100)[001].

For the (100)[001] crystal orientation, octahedral slip planes tend to dominate over cubic slip systems, even under elevated temperature conditions. Consequently, crack initiation is expected to occur predominantly on {111} slip planes, with crack propagation following cleavage stress directions associated with Mode I opening. This behavior implies that crack initiation locations are strongly influenced by the crystallographic orientation of the specimen, despite experiencing the same elastic stress field shown in Figure 2.8.

To evaluate lifetimes across various cut orientations, the local coordinate system of the crystal plasticity framework is rotated to align with the direction of applied tensile load. Figures 2.9 and 2.10 present a comparison between predicted crack initiation sites and simulation results for specimens with different cut orientations.

In the case of the <001> orientation, cracks are observed to initiate just above the notch tip, even though the highest geometric stress concentration is located at the notch root, as shown in Figure 2.10a. This finding is attributed to significant slip accumulation in that region, resulting from the combined elastic and plastic anisotropy specific to this orientation [88]. A similar mechanism is evident in Figures 2.9a and 2.10c for <011> and <111> orientations, where the dominant slip systems (listed in Table 2.1) are more aligned with the loading direction, thus facilitating slip activity near the notch tip.

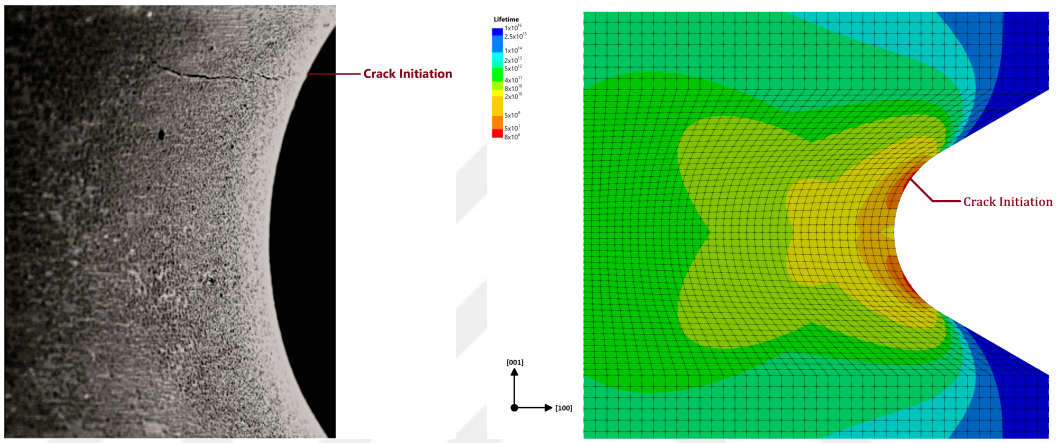

(**a**) (**b**)

Figure 2.9: Fatigue crack initiation at the surface of SC16 nickel-base single crystal with tensile crystal orientation <001> is represented in (**a**). Reproduced with permission from S. Forest, Crystal plasticity and damage at cracks and notches in nickel-base single-crystal superalloys [88]. Lifetime assessment of the same specimen orientations is represented in (**b**), where the minimum lifetime on the FEA model is marked as the predicted crack initiation location.

Figures 2.9 and 2.10 also show that the predicted crack initiation contours align well with experimental observations, as the highest cleavage stresses coincide with regions of pronounced slip accumulation. This agreement highlights the capability of the numerical model to capture the interplay between local stress fields and crystallographic slip, which governs crack initiation in these materials. Moreover, the consistency between the predicted contours and experimental crack paths provides further confidence in the model's ability to represent the complex anisotropic behavior of single-crystal superalloys under cyclic loading.

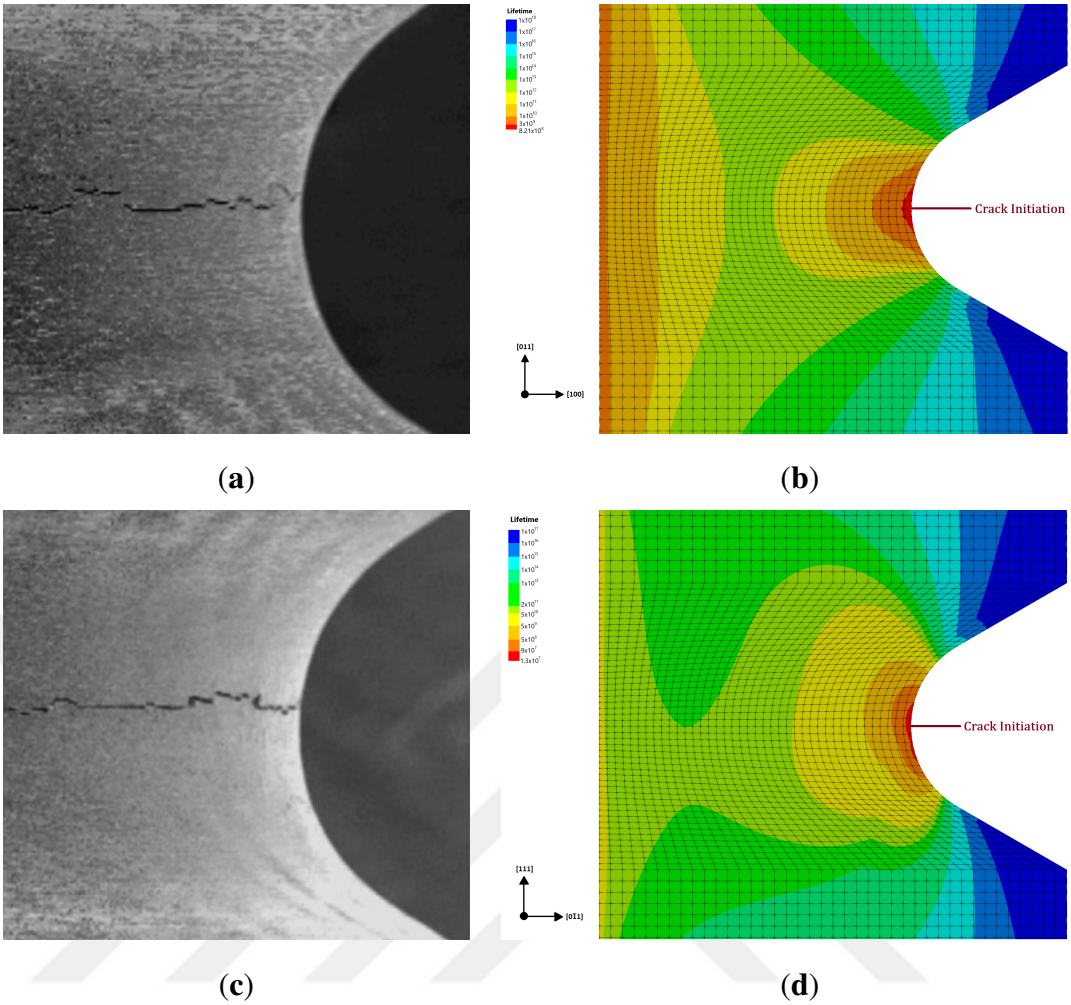

Figure 2.10: Fatigue crack initiation at the surface of SC16 nickel-base single crystal with tensile crystal orientations ⟨011⟩ and ⟨111⟩ is shown in (**a**) and (**c**), respectively. Lifetime assessments of the same specimen orientations are given in (**b**) and (**d**), where the minimum lifetime predicted by the FEA model indicates the expected crack initiation sites. Reproduced with permission from S. Forest, *Crystal Plasticity and Damage at Cracks and Notches in Nickel-Base Single-Crystal Superalloys* [88].

Finally, Figure 2.11 and Figure 2.12 illustrate the high-cycle fatigue (HCF) lifetime predictions for notched CMSX-4 specimens, modeled at 750 °C for different R-ratios, using the parameter sets listed in Tables A.1 and A.2. The numerical results are compared against experimental data to assess the accuracy of the model. The predicted lifetimes for both $R = 0$ and $R = 0.6$ show strong agreement with the corresponding experimental data, demonstrating the model's capability to capture the fatigue behavior of notched specimens under high-cycle loading conditions.

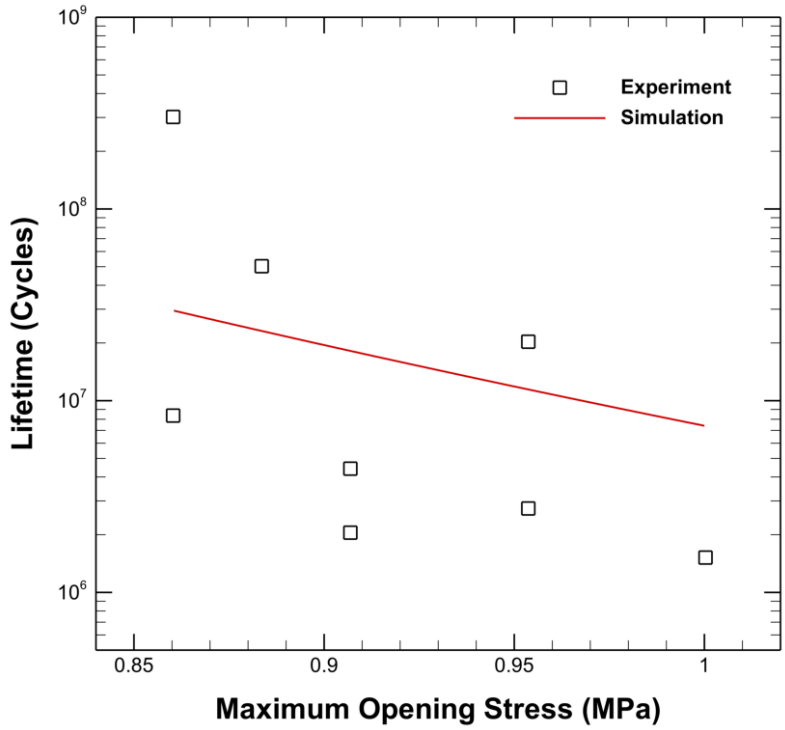

Figure 2.11: Comparison of numerical and experimental results of CMSX-4 notched specimens under HCF loading at 750 °C for $R = 0$.

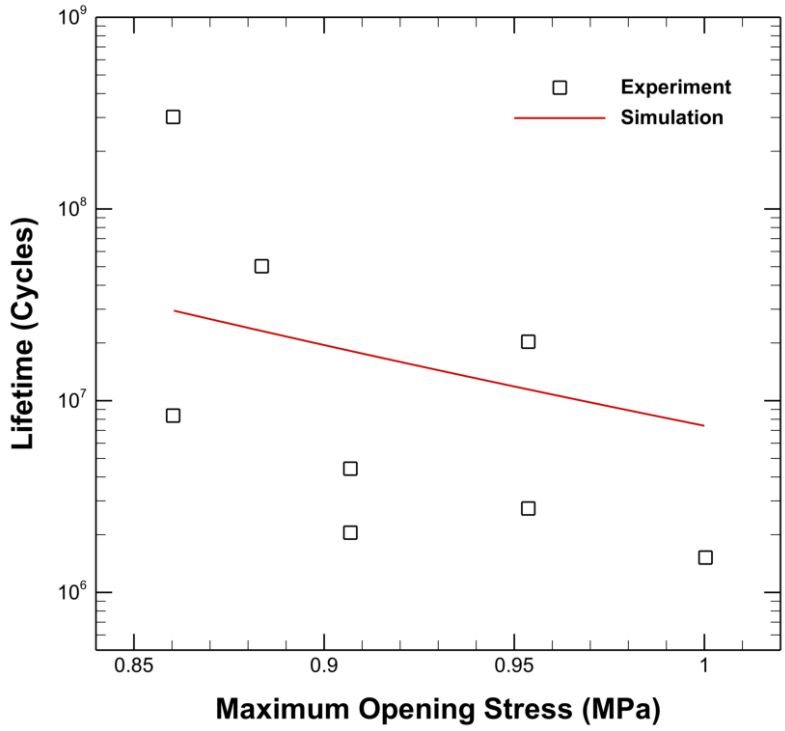

Figure 2.12: Comparison of numerical and experimental results of CMSX-4 notched specimens under HCF loading at 750 °C for $R = 0.6$.

The results demonstrate that the implemented lifetime assessment framework yields consistent agreement with both qualitative and quantitative experimental data. The model successfully captures fatigue crack initiation locations and relative lifetime trends under different loading conditions without requiring further modification to the underlying fatigue damage formulation. However, the current approach lacks the capability to generalize the effect of temperature on fatigue life, as the physical-based model does not inherently account for temperature-dependent failure mechanisms beyond those calibrated directly.

Rather than modifying the existing constitutive framework, artificial neural networks (ANNs) offer a more flexible solution for incorporating additional effects such as creep, dwell interaction, or complex load histories. The following chapter explores the integration of ANNs into the lifetime assessment process to enhance predictive capability and extend the model's applicability across a broader range of service conditions.

CHAPTER 3

ANN-BASED LIFETIME ESTIMATION

3.1 Literature Review

3.1.1 Early Development of Artificial Neural Networks

The conceptual roots of artificial neural networks (ANNs) originate from neuroscience-inspired computational models developed in the mid-20th century. The foundational work was conducted by McCulloch and Pitts, who in 1943 introduced the first mathematical abstraction of a neural network, demonstrating how networks of simple binary neurons could simulate logical reasoning processes [90]. Shortly thereafter, Hebb proposed the theory of synaptic plasticity, now referred to as Hebbian learning, which suggested that connections between neurons strengthen through co-activation [91]. These principles laid the groundwork for biologically inspired learning systems.

In 1958, Rosenblatt introduced the perceptron model, which could learn from input–output pairs by adjusting weights in a supervised fashion [92]. While a major milestone, the model was later criticized by Minsky and Papert in their 1969 book for its inability to solve non-linearly separable problems, such as XOR logic [93]. This criticism contributed to a temporary decline in neural network research during the 1970s.

Despite this setback, progress continued in alternative network topologies. Group Method of Data Handling (GMDH), developed by Ivakhnenko [94], introduced a deep multilayer structure for self-organizing systems as early as 1971. In the 1980s, Hopfield [95] introduced a recurrent architecture for associative memory tasks, and

Kohonen [96] developed self-organizing maps (SOMs) for topological feature mapping.

The resurgence of neural networks occurred in 1986 with the introduction of the backpropagation algorithm for training multilayer perceptrons, as demonstrated by Rumelhart, Hinton, and Williams [97]. This re-enabled deep learning capabilities through error-driven weight updates and opened the door for feed-forward networks to solve non-linear problems. These developments eventually led to the modern deep learning revolution in the 2010s, with improved training techniques and architectures, as summarized by LeCun et al. [98].

3.1.2 Applications to Engineering and Materials Science

Following the mathematical formalization of neural networks, researchers in the 1990s began to apply ANNs to engineering problems, particularly those involving pattern recognition, prediction, and modeling of complex nonlinear relationships. A Feed-forward neural network structure tailored for regression tasks is illustrated in Figure 3.1. Feed-forward neural networks (FFNNs) became a standard method for material behavior prediction due to their universal function approximation property. They were adopted for predicting stress–strain behavior, failure modes, and thermal properties across a wide variety of materials and loading regimes [99, 100].

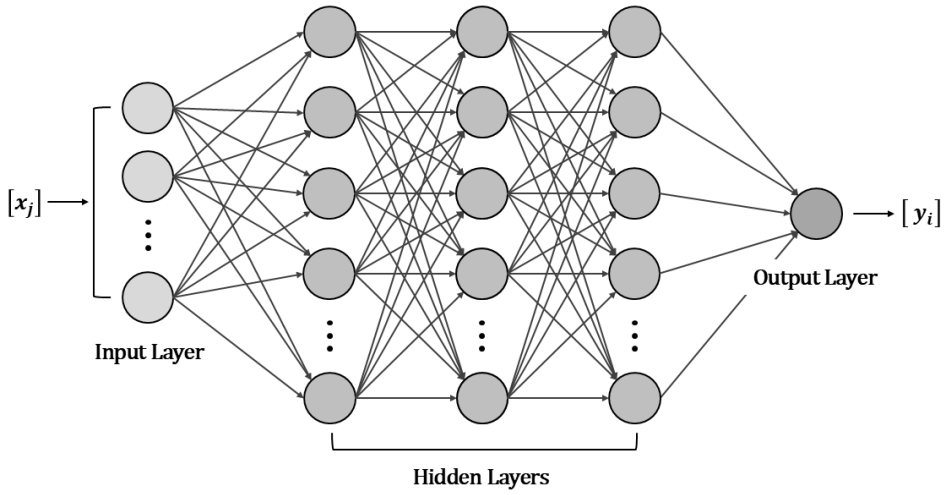

Figure 3.1: Structure of feed-forward neural networks (FFNNs) tailored for regression tasks, illustrating the input, hidden, and output layers.

In fatigue research, FFNNs were used to generate S–N curves directly from material properties and loading conditions, reducing the dependency on large-scale experimentation. Applications expanded to elevated temperature behavior prediction (e.g., creep–fatigue life) [101], composite laminates [41, 102], and damage accumulation under spectrum loading [103]. These implementations demonstrated the versatility of ANNs, including modular and ensemble networks for energy-based fatigue models [104].

3.1.3 ANNs for Lifetime Estimation

Neural network applications in fatigue life estimation became more systematic and extensive in the early 2000s. Several researchers focused on FFNNs due to their straightforward implementation for supervised regression tasks. Xiang et al. [105] demonstrated successful ANN-based lifetime prediction for rubber composites, while Maleki et al. [106] applied neural models to shot-peened steels.

A comprehensive review was conducted by Santecchia et al. [28], who classified fatigue life prediction models into stress-life (S–N), strain-life (ϵ–N), and crack growth frameworks, evaluating how ANNs contribute to each. More recently, Chen and Liu [27] surveyed the various NN architectures, including FFNNs, convolutional NNs (CNNs), and recurrent NNs (RNNs), applied to fatigue modeling, and emphasized the growing integration with hybrid or physics-informed frameworks.

3.1.4 Recent Advances in Lifetime Prediction

Recent work has explored deep learning models that integrate physical insight with data-driven flexibility. Zhang et al. [107] proposed a deep learning method that simultaneously handles creep, fatigue, and combined creep–fatigue loading conditions. Gulgec et al. [108] introduced a strain prediction method using acceleration data and deep networks for structural health monitoring.

Alqahtani et al. [109] utilized CNNs to classify crack propagation states, while Zhan and Li [110] trained machine learning models on additive manufacturing parame-

ters for fatigue prediction of stainless steel components. Kalayci et al. [111] further reviewed soft computing techniques in fatigue, comparing them with conventional empirical models.

These studies collectively suggest that ANN-based fatigue prediction is evolving from purely data-driven mappings to hybrid and application-specific networks that exploit domain knowledge, allowing for generalized lifetime prediction across a wide range of materials and mechanical scenarios.

3.2 Fundamentals of Artificial Neural Networks

Artificial Neural Networks (ANNs) are a class of machine learning algorithms originally inspired by the structure and function of biological neural systems. While biological neurons transmit electrical signals through interconnected synapses to perform cognitive tasks, artificial neurons are simplified mathematical constructs designed to perform numerical computations through weighted combinations of inputs and nonlinear transformations. ANNs have evolved into powerful function approximators capable of modeling intricate nonlinear relationships between high-dimensional inputs and outputs. Their capacity to learn directly from data and generalize beyond the training set has made them increasingly valuable for predictive modeling in materials science and mechanical engineering, particularly in applications involving fatigue life estimation, creep deformation, damage evolution, and fracture behavior [112, 113].

Unlike traditional analytical models, ANNs do not require explicit formulations of constitutive relationships. Instead, they infer mappings by optimizing internal parameters (weights and biases) over large datasets. This data-driven paradigm is especially advantageous in cases where physical models are difficult to construct or computationally expensive to evaluate, such as in the fatigue assessment of anisotropic single crystal superalloys subjected to thermomechanical loading. As such, ANNs are increasingly being explored either as standalone surrogate models or as complementary tools within hybrid physics-informed frameworks [27].

In this section, the mathematical underpinnings and architectural components of ANNs are presented in detail. Key topics include the structure and function of neurons,

activation functions, loss functions, gradient-based optimization methods, and regularization strategies. This foundation serves as the basis for the predictive models introduced later in this chapter, where ANN-based frameworks are applied to fatigue life estimation using both experimental and synthetic datasets.

3.2.1 Artificial Neuron and Network Architecture

The artificial neuron is the fundamental computational unit of an ANN. Each neuron receives multiple inputs, scales them by trainable weights, adds a bias, and processes the result through a nonlinear activation function. The output y of a neuron is given by:

$$y = f(z) = f\left(\sum_{i=1}^{n} w_i x_i + b\right) \tag{3.1}$$

where:

- x_i are the input values,
- w_i are the associated weights,
- b is the bias term, and
- $f(\cdot)$ is the activation function.

The nonlinear function f is crucial; without it, the network would reduce to a linear combination of inputs regardless of depth. These neurons are arranged in layers: the *input layer* receives the raw data, *hidden layers* transform data into useful intermediate representations, and the *output layer* provides the final prediction. A network composed of at least one hidden layer is referred to as a *Multilayer Perceptron (MLP)* [113].

The capacity of an ANN to approximate complex functions increases with the number of layers (depth) and neurons per layer (width). According to the universal approximation theorem, a single hidden layer network can approximate any continuous function to arbitrary precision, provided it has sufficient width [114]. However,

deeper networks are generally more parameter-efficient and better at capturing hierarchical patterns, which is particularly beneficial in modeling physical processes involving multiscale interactions, such as cyclic damage accumulation or dislocation-based plasticity [112].

In fatigue modeling, input features may include quantities such as maximum stress, stress ratio R, temperature, dwell time, or cycle frequency, while the output is typically a scalar value representing fatigue life (e.g., number of cycles to failure). The architecture must be chosen to balance expressive power and generalization ability. Too small a network may underfit the training data, while overly complex architectures risk overfitting and poor extrapolation.

3.2.2 Activation Functions

Activation functions are mathematical transformations applied to the neuron's aggregated input. Their primary purpose is to introduce nonlinearity, allowing the network to learn complex and non-additive mappings between input and output variables. In the absence of nonlinear activation, a network composed of linear operations would be mathematically equivalent to a single-layer linear model, regardless of its depth—significantly limiting its ability to model real-world physical phenomena.

Table 3.1: Common activation functions used in artificial neural networks.

Name	**Equation**	**Range**
Sigmoid	$\frac{1}{1+e^{-x}}$	$(0, 1)$
Tanh	$\frac{e^{x}-e^{-x}}{e^{x}+e^{-x}}$	$(-1, 1)$
ReLU	$\max(0, x)$	$[0, \infty)$
Leaky ReLU	$\max(\alpha x, x)$	$(-\infty, \infty)$
ELU	x if $x \geq 0$, else $\alpha(e^{x} - 1)$	$(-\alpha, \infty)$
Swish	$x \cdot \text{sigmoid}(x)$	$(-0.28, \infty)$

Table 3.1 provides an overview of popular activation functions employed in artificial neural networks, including their equations and corresponding output value ranges. The choice of activation function can substantially impact the learning dynamics, con-

vergence behavior, and ultimately, the predictive accuracy of the model. Activation functions must be differentiable (or at least sub-differentiable) to permit backpropagation of gradients during training. Moreover, they should maintain healthy gradient flow across layers to avoid the well-known *vanishing gradient* or *exploding gradient* problems [115].

Historically, the sigmoid and hyperbolic tangent (tanh) functions were widely used in early neural network designs due to their smooth and continuous nature. However, they both suffer from saturation at large input magnitudes, resulting in near-zero gradients that hinder weight updates; a problem known as the vanishing gradient issue. Tanh offers a zero-centered output range, which can be advantageous for faster convergence in networks where input distributions are symmetrically distributed about zero [113].

The introduction of the Rectified Linear Unit (ReLU) marked a significant advancement in deep learning. Its simplicity and efficiency stem from the fact that it returns zero for all negative inputs and retains positive inputs unchanged. This sparsity in activation reduces computational cost and mitigates the vanishing gradient problem. However, ReLU has its own limitation; if a neuron consistently receives negative inputs, it may stop updating entirely, leading to "dead neurons."

To address this, variants such as Leaky ReLU and Exponential Linear Unit (ELU) were developed. Leaky ReLU introduces a small slope in the negative region, typically with $\alpha \approx 0.01$, ensuring that gradients remain nonzero even for negative inputs. ELU, on the other hand, produces smooth outputs and enforces a mean activation close to zero, promoting faster learning and better generalization [115].

The Swish activation function, introduced by Ramachandran et al. [116], is a smooth, non-monotonic function that has shown superior performance in deep models, particularly in large-scale learning tasks. By combining the identity function and sigmoid gating, Swish allows gradient flow while preserving complex representational capacity.

In the context of fatigue life modeling, ReLU and Leaky ReLU remain the most practical choices due to their computational efficiency and stability during training. They

are especially useful in deep architectures where lifetime predictions span multiple orders of magnitude. Nevertheless, alternative functions such as Swish may offer benefits in transfer learning frameworks or when integrating heterogeneous datasets.

3.2.3 Loss Functions and Optimization Methods

In supervised learning frameworks, the loss function, also referred to as the cost or objective function, plays a central role by quantifying the discrepancy between predicted outputs ($\hat{y}$) and actual targets (y). The purpose of training a neural network is to minimize this loss function over a given dataset, thereby enabling the model to generalize from input features to accurate predictions. In the context of fatigue life prediction, which is inherently a regression problem, this task typically involves predicting continuous variables such as the number of cycles to failure or rupture time based on a set of mechanical and environmental features.

Loss Functions for Regression Problems

The choice of loss function is critical, as it directly influences the convergence behavior, sensitivity to outliers, and robustness of the model. The two most commonly employed loss functions in regression-based fatigue life prediction are the Mean Squared Error (MSE) and the Mean Absolute Error (MAE).

Mean Squared Error (MSE):

$$\mathcal{L}_{\text{MSE}} = \frac{1}{N}\sum_{i=1}^{N}(\hat{y}_i - y_i)^2 \tag{3.2}$$

MSE emphasizes larger errors due to the square term, making it particularly effective when large deviations from the true value are unacceptable. However, its sensitivity to outliers can be a disadvantage in experimental fatigue datasets, which often contain anomalies due to specimen or testing variability [112].

Mean Absolute Error (MAE):

$$\mathcal{L}_{\text{MAE}} = \frac{1}{N}\sum_{i=1}^{N}|\hat{y}_i - y_i| \tag{3.3}$$

MAE treats all deviations equally, resulting in more robust training, especially in the presence of noisy or heteroscedastic data. Its piecewise linear derivative makes it less sensitive to outliers but can lead to slower convergence due to a lack of smooth curvature [113].

In recent literature, a logarithmic variant is often used for fatigue modeling because the number of cycles to failure may span several orders of magnitude:

$$\mathcal{L}_{\log} = \frac{1}{N}\sum_{i=1}^{N}\left(\log_{10}(\hat{y}_i) - \log_{10}(y_i)\right)^2 \tag{3.4}$$

This formulation ensures that multiplicative errors (e.g., predicting 10,000 instead of 1,000 cycles) are treated more evenly across fatigue regimes [117].

Customized Loss Functions in Physics-Informed Models

In physics-informed neural networks (PINNs), loss functions are designed to integrate physical knowledge or boundary conditions into the learning process. These custom terms supplement the traditional error-based loss and are typically weighted by hyperparameters to control their influence during training. Such loss functions take the general form:

$$\mathcal{L}_{\text{total}} = \mathcal{L}_{\text{data}} + \lambda_1\mathcal{L}_{\text{physics}} + \lambda_2\mathcal{L}_{\text{constraints}} \tag{3.5}$$

where $\mathcal{L}_{\text{data}}$ represents conventional error terms like MSE or MAE, and the remaining terms embed domain-specific constraints or governing equations [118].

Gradient-Based Optimization

Once the loss function is defined, model parameters are optimized using gradient descent methods, which iteratively adjust weights w in the direction of decreasing loss:

$$w \leftarrow w - \eta\frac{\partial\mathcal{L}}{\partial w} \tag{3.6}$$

where η is the learning rate. Full-batch gradient descent computes gradients over the entire dataset, which can be computationally intensive for large datasets.

Stochastic Gradient Descent (SGD) addresses this by computing the gradient using a single randomly selected data point:

$$w \leftarrow w - \eta \frac{\partial \mathcal{L}(x_i, y_i)}{\partial w} \tag{3.7}$$

Though noisier, SGD performs frequent updates and its stochasticity helps avoid shallow local minima [119]. An intermediate strategy is *mini-batch gradient descent*, which uses small subsets of data to balance gradient accuracy and computational efficiency.

Adaptive Optimization Algorithms

Adaptive methods such as Adam (Adaptive Moment Estimation) dynamically adjust the learning rate for each parameter:

$$\begin{aligned} m_t &= \beta_1 m_{t-1} + (1 - \beta_1) \nabla \mathcal{L}_t \\ v_t &= \beta_2 v_{t-1} + (1 - \beta_2)(\nabla \mathcal{L}_t)^2 \\ w &\leftarrow w - \eta \frac{\hat{m}_t}{\sqrt{\hat{v}_t} + \epsilon} \end{aligned} \tag{3.8}$$

Adam is preferred for its robustness, rapid convergence, and suitability for noisy gradient landscapes [120]. Its variant AdamW decouples weight decay from the gradient update rule, improving generalization on overparameterized models [121].

Regularization Techniques

In the context of fatigue life modeling, where the size of available experimental datasets is often constrained due to the cost and duration of mechanical testing, overfitting becomes a major concern. Overfitting occurs when a model learns spurious patterns or noise within the training data rather than generalizable features, leading to poor performance on unseen data. This risk is amplified in high-capacity neural networks with thousands or millions of trainable parameters. As such, regularization strategies are critical to ensure the learned representations remain robust, physically meaningful, and generalizable across varying loading conditions and alloy compositions.

L2 Regularization (Weight Decay)

L2 regularization adds a penalty term to the loss function that discourages large weights, promoting smoother model behavior. The regularized loss is given by:

$$\mathcal{L}_{\text{total}} = \mathcal{L} + \lambda \sum_{j=1}^{P} w_j^2 \tag{3.9}$$

where λ is the regularization coefficient, P is the number of weights in the network, and w_j denotes the jth weight. This formulation biases the optimizer toward simpler models with smaller parameter norms, in line with the principle of Occam's razor. It is particularly effective when the training set is small or contains outliers that might otherwise cause the model to overfit sharply curved or high-magnitude solutions [112].

Dropout Regularization

Dropout is a stochastic regularization technique in which a subset of neurons is randomly "dropped" (i.e., set to zero) during each forward pass in training. Formally, a dropout mask $\mathbf{r} \sim \text{Bernoulli}(p)$ is applied element-wise to the activations:

$$\tilde{h}_i = r_i h_i, \quad \text{with } r_i \in \{0, 1\}, \quad \mathbb{P}(r_i = 1) = p \tag{3.10}$$

where h_i is the output of neuron i and p is the retention probability. By preventing neurons from relying on the presence of specific other neurons, dropout encourages the network to learn redundant, distributed representations. This helps reduce co-adaptation of features and improves robustness against data noise. In practice, dropout is typically disabled during inference by scaling the activations to their expected values [122].

Dropout is particularly useful in fatigue modeling scenarios where:

- The sample size is insufficient to cover all relevant loading cases;
- Certain regions of the stress-life domain are overrepresented;
- The network must generalize across interpolated and extrapolated temperature regimes.

Early Stopping

Early stopping is a dynamic form of regularization that monitors performance on a validation set during training and halts training once the model begins to overfit. This is typically implemented by observing the validation loss over epochs and stopping once no improvement is detected for a predefined number of steps (patience). Unlike static methods like L2 regularization, early stopping adapts to the complexity of the training process and avoids excessive memorization of training data noise.

In fatigue life prediction, early stopping is often essential due to the following:

- Limited diversity of training cycles and loading configurations;
- Strong noise components in experimental fatigue datasets;
- Irreversibility of model overfitting during prolonged training.

In this chapter, a custom early stopping strategy is introduced, specifically tailored to fatigue lifetime prediction tasks. In addition to monitoring the loss value, the method evaluates whether the predicted SN curve exhibits a physically consistent nonlinear relationship between stress amplitude and number of cycles to failure. If the predicted lifetime deviates from expected trends (e.g., non-monotonicity, slope inversions, or unrealistic endurance limits), training is halted early even if the validation loss appears to improve. This approach promotes stable models that generalize well while maintaining physically meaningful behavior across all stages of the SN curve. It is particularly effective when training on hybrid datasets combining both synthetic and experimental inputs, where loss reduction may not always correlate with mechanistic interpret-ability.

Combining Regularization Strategies

In practice, regularization techniques are most effective when used in combination. For instance, dropout and L2 regularization can be used simultaneously to control both the co-adaptation of units and the magnitude of weights. When working with transfer learning frameworks in fatigue modeling where pretrained base models are extended to new loading types, temperature domains, or alloy systems, early stopping can be coupled with reduced learning rates and layer freezing to preserve useful feature hierarchies while avoiding overfitting to small target datasets.

Thus, the appropriate design and tuning of regularization strategies are crucial in applying artificial neural networks to fatigue life prediction tasks, especially when bridging synthetic and experimental data domains.

3.3 Training with Experimental and Semi-Generated Data

This subsection presents the development of two artificial neural network (ANN) models trained on experimentally obtained datasets without the use of physics-based synthetic data. These models are designed to provide preliminary fatigue life predictions for single crystal superalloys by directly learning from empirical data while maintaining physically interpretable trends. The training data is derived from the experimental work of Aslan [84], which includes both creep rupture and fatigue life tests conducted across a range of mechanical and thermal loading conditions.

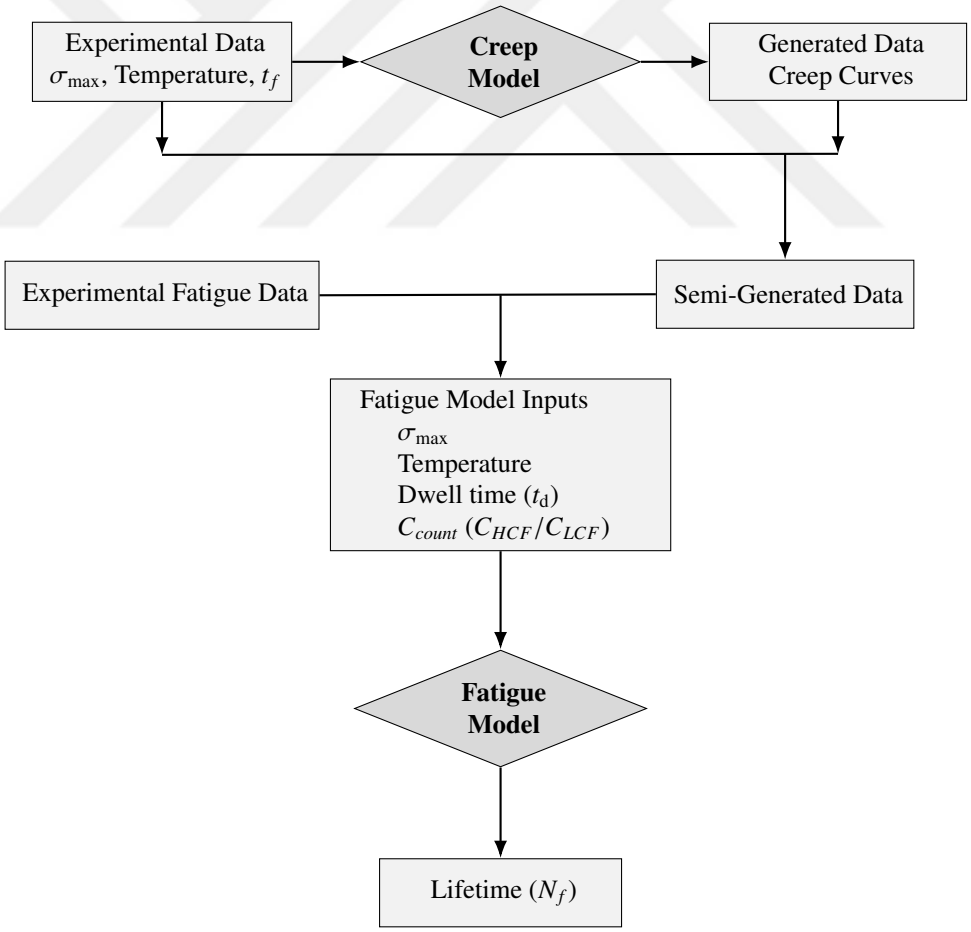

Figure 3.2: Workflow integrating experimental and semi-generated obtained from creep model for fatigue model lifetime prediction.

Creep Model Configuration

The first ANN is trained to model high-temperature creep behavior. The input parameters for this model are the applied stress $\sigma_{\max}$ and temperature T, while the output is the rupture time t_r. The primary goal of this model is to capture the time-dependent deformation mechanisms of CMSX-4 under sustained loading, which are critical to understanding the role of dwell time in fatigue life degradation. Once trained, the predicted rupture times are introduced into the fatigue ANN as approximated dwell time values. This approach allows for the incorporation of time-dependent damage effects without requiring a fully coupled creep-fatigue simulation framework.

Fatigue Model Configuration

The second ANN is tasked with predicting fatigue lifetime (N_f) directly from a set of high-level physical input variables. These include the stress ratio R, temperature T, dwell time (derived from the creep model), and the ratio between high cycle fatigue (HCF) and low cycle fatigue (LCF) components, which quantifies the severity of Combined Cycle Fatigue (CCF). All input features are normalized prior to training, and the fatigue model is trained independently from the creep model.

The training dataset includes a combination of fatigue data collected under LCF, HCF, and CCF conditions. In order to enhance model robustness and provide generalization across different loading histories, dummy values are introduced during preprocessing. Specifically, high ultimate tensile strength (UTS) values ranging from 10^{10} to 10^{12} are assigned to account for infinite lifetime regions and stress insensitivity thresholds. These serve to prevent overfitting and allow the model to learn transitions between failure and endurance zones. Similarly, a limited number of dwell time estimates are interpolated using the creep ANN to account for fatigue test conditions not explicitly documented in the experimental record.

Model Architecture and Performance

The Creep and Fatigue Models are implemented as fully connected FFNNs with different structural configurations. The Creep Model comprises 4 hidden layers with 40 neurons each, while the Fatigue Model includes 10 hidden layers, each containing 100 neurons. Both models use the ReLU activation function, which ensures non-saturating gradients and improves convergence in deep architectures [123].

Training is performed using stochastic gradient descent (SGD) with learning rates of $\eta_{\text{creep}} = 0.0001$ and $\eta_{\text{fatigue}} = 0.001$. The objective function for both models is the mean squared error (MSE), given respectively by:

$$\mathcal{L}_{\text{MSE}}^{\text{creep}} = \frac{1}{n}\sum_{i=1}^{n}(t_i - \hat{t}_i)^2 \quad \text{and} \quad \mathcal{L}_{\text{MSE}}^{\text{fatigue}} = \frac{1}{n}\sum_{i=1}^{n}\left(N_i - \hat{N}_i\right)^2 \tag{3.11}$$

where t_i and N_i denote the ground truth rupture time and fatigue lifetime for the ith data point, and $\hat{t}_i$ and $\hat{N}_i$ are the corresponding ANN predictions.

Fifteen percent of the total dataset is reserved as a test set to assess generalization. Performance metrics in terms of training and test losses are reported in Table 3.2. While the Creep Model is mainly used to estimate dwell time effects, the Fatigue Model directly predicts fatigue lifetime for loading histories including low cycle fatigue (LCF), high cycle fatigue (HCF), and combined cycle fatigue (CCF).

Table 3.2: Training and test losses (MSE) for experimental ANN models.

Model	**Training Loss (MSE)**	**Test Loss (MSE)**
Creep	0.0180	0.0145
Fatigue	0.0553	0.0547

The agreement between experimental and predicted values is further illustrated in Figure 3.3 and Figure 3.4. The first shows the creep curves produced by the ANN across a range of temperatures, highlighting the stress-time dependence. The second presents predicted versus experimental fatigue lifetimes, including LCF, HCF, and CCF cases across different R-ratios. Both figures confirm that the models provide physically consistent predictions over a wide range of conditions, even without the use of synthetic data.

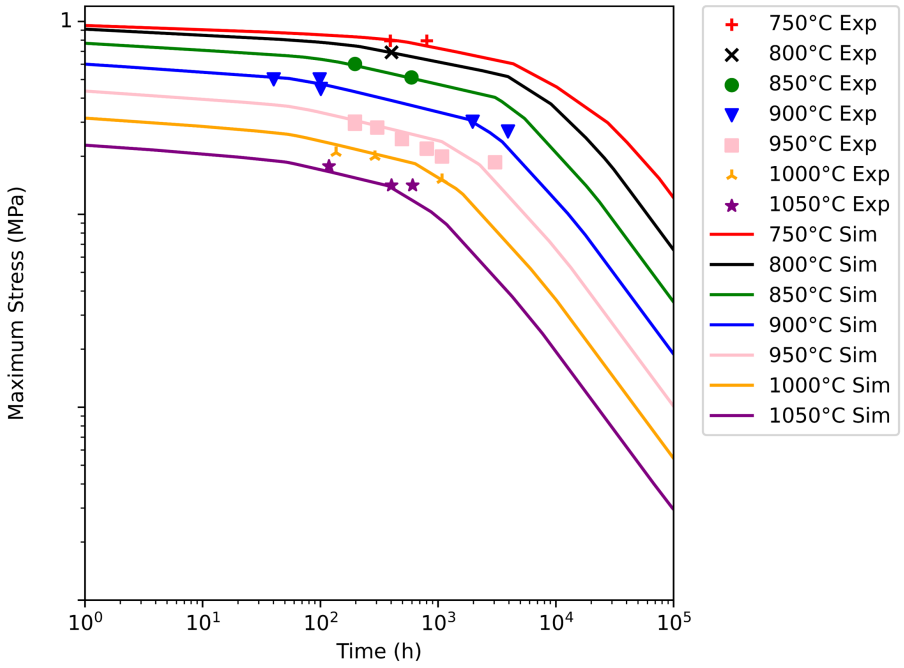

Figure 3.3: Creep curve predictions using the trained ANN model. Experimental data points and predicted curves are shown for various temperatures.

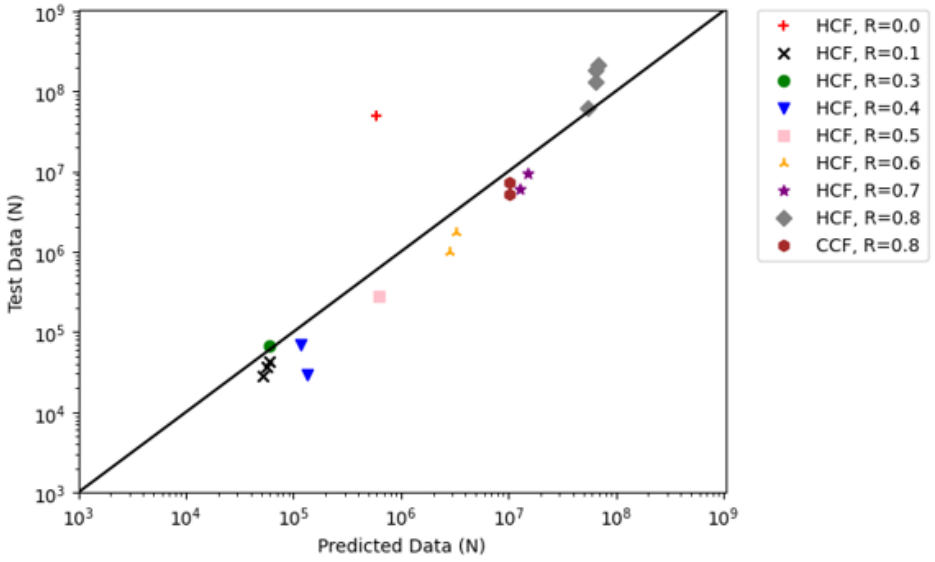

Figure 3.4: Fatigue model predictions versus experimental results on test data. Data includes HCF, and CCF experiments across various R-ratios.

Although both models show favorable predictive accuracy, some input values used during preprocessing are interpolated or dummy-assigned. In particular, high ultimate tensile strength (UTS) values ranging from 10^{10} to 10^{12} are introduced to mark

high-lifetime regions and prevent overfitting. Similarly, dwell time values not explicitly available in the dataset are estimated using the creep model. While these augmentations support generalization, they are insufficient to produce fully consistent SN curves or to capture damage accumulation across broader loading modes. Consequently, in the next subsection, a physics-based synthetic dataset generated via a calibrated Chaboche model is introduced to enhance fatigue prediction coverage and structural robustness.

3.4 Training with Synthetic Data Generated from the Chaboche Model

3.4.1 Material Parameter Selection and Temperature-Specific Optimization

The Chaboche damage model used for fatigue lifetime prediction requires a set of temperature-dependent material parameters. As detailed in Chapter 2, the model incorporates constitutive terms that evolve differently under varying thermal conditions. For this reason, distinct parameter sets were optimized for each target temperature: 600 °C and 900 °C. The necessity of separate calibrations arises from the strong influence of temperature on mechanical properties such as ultimate tensile strength (σ_{UTS}), yield behavior, and creep resistance in nickel-based single crystal superalloys such as CMSX-4.

These parameters were fitted using experimental fatigue curves obtained from Aslan [84] for both temperatures. The resulting optimized values are provided in Appendix A. This separation ensures the Chaboche model faithfully reproduces the material behavior under each thermal condition, enabling the generation of synthetic lifetime data consistent with experimental observations.

The temperature-sensitive formulation particularly affects the softening behavior and fatigue limit definition, which are critical for modeling transitions from low-cycle fatigue (LCF) to high-cycle fatigue (HCF) regimes. By resolving the model for each temperature independently, the synthetic data produced become well-suited for training data-driven models such as ANNs, which benefit from high-fidelity input-output mappings without introducing artificial variability across temperature domains.

3.4.2 Synthetic Data Generation via Chaboche Model

The fatigue lifetime curves used to train the neural network model in this section were generated using the Chaboche-based damage framework calibrated separately for 600 °C and 900 °C. Once the temperature-specific parameters were obtained, the model was used to compute fatigue lifetimes over a broad range of stress amplitudes and R-ratios. For each temperature, synthetic data were generated in the following ranges:

- **Stress Range:** From σ_{end} up to σ_{UTS}
- **R-ratio:** From $R = 0$ to $R = 0.4$ in increments of 0.1
- **Lifetime Target:** Maximum lifetime capped at 10^8 cycles (considered as infinite life)

Each generated dataset follows the physics-based predictions of the Chaboche damage model, eliminating the need for dummy extrapolations or artificial upper-bound limits that were used in earlier experimental+semi-generated datasets (see Section 3.3). This provides a high-fidelity dataset in the $\log_{10}(N)$ domain across R-ratios and stress amplitudes at both temperatures.

The purpose of generating this dataset is to provide a well-distributed and physically consistent training space for the ANN. These synthetic curves preserve nonlinearities inherent in fatigue behavior—such as the rapid drop in life near UTS or the flattening of curves near the endurance limit—enabling the model to learn realistic trends even in sparsely available experimental regimes.

In total, over 400 synthetic data points were created per temperature, combining various R-ratios and stress levels. The resulting dataset is visualized in Figure 3.5 and Figure 3.6, showing the fatigue life predictions from the Chaboche model for CMSX-4 at both 600 °C and 900 °C across the stress–lifetime spectrum.

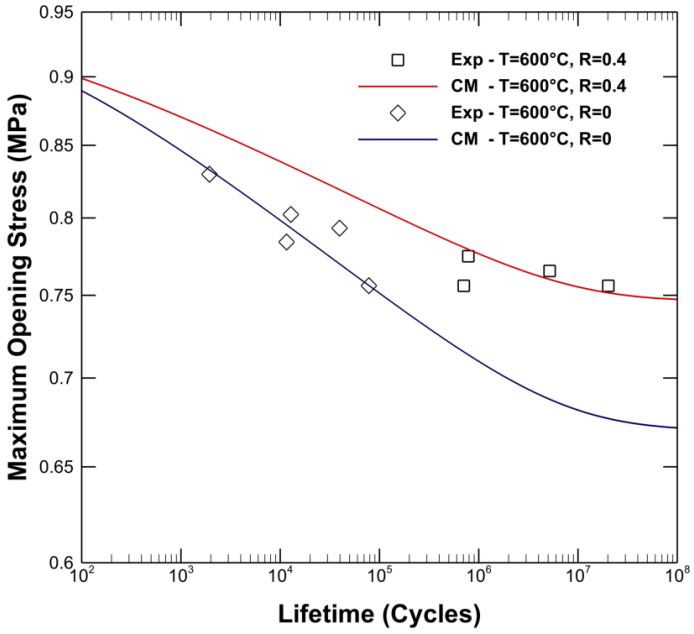

Figure 3.5: Synthetic SN curves produced using the Chaboche model for CMSX-4 at 600 °C with various R-ratios.

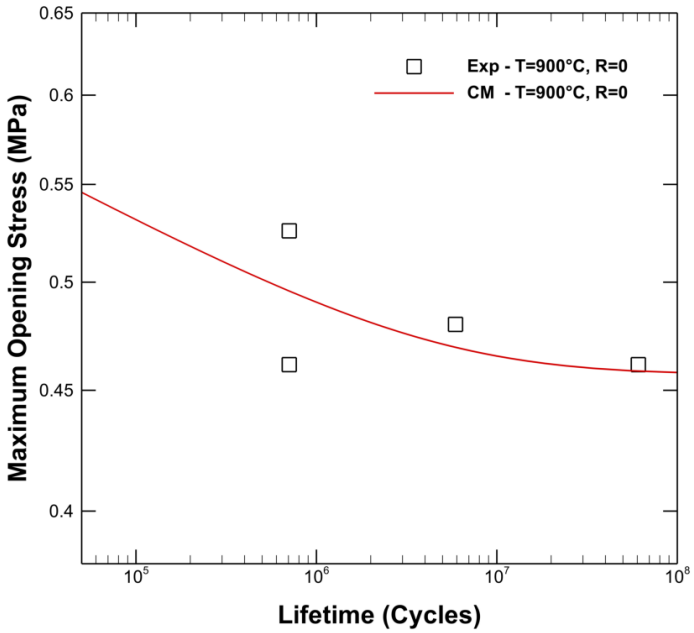

Figure 3.6: Synthetic SN curves produced using the Chaboche model for CMSX-4 at 900 °C with various R-ratios.

3.4.3 Model Architecture and Training Setup

To capture the nonlinear fatigue behavior encoded in the synthetic dataset, a fully connected feed-forward artificial neural network (ANN) architecture was employed. The model was designed to map three input features to the corresponding fatigue lifetime value in log-scale:

- Maximum Stress ($\sigma_{\max}$)
- R-Ratio (R)
- Temperature (T)

The model consists of 10 hidden layers, each with 100 neurons, using the ReLU activation function. The choice of ReLU improves convergence and maintains sparsity in gradient updates, preventing the vanishing gradient problem in deeper networks [123]. Batch normalization layers were not applied since the input space was already normalized across all dimensions prior to training. The output is a scalar prediction of lifetime, N, in $\log_{10}(N)$ format.

Model training was conducted using the stochastic gradient descent (SGD) optimizer with a learning rate of $\eta = 0.001$, and the mean squared error (MSE) loss function defined as:

$$\mathcal{L}_{\text{MSE}} = \frac{1}{n} \sum_{i=1}^{n} \left(\log_{10}(N_i) - \log_{10}(\hat{N}_i) \right)^2 \tag{3.12}$$

A batch size corresponding to 3.5% of the total training set was used, and training was performed for 250 epochs. During training, validation loss was monitored and early stopping was applied based on a custom heuristic. Specifically, training was halted if the validation RMSE plateaued over 20 consecutive epochs while the training loss continued to decrease. This criterion ensured that overfitting was avoided and that the network captured only the general trends present in the data without exploiting artifacts.

The temperature dependence of fatigue behavior was handled implicitly through this input, enabling the model to interpolate lifetime predictions between 600 °C and 900 °C. This architecture setup is chosen to serve as a baseline before applying transfer learning in the subsequent section.

Model Configuration and Training Details

The artificial neural network trained on synthetic data generated by the Chaboche model was designed to capture complex, nonlinear interactions between maximum stress, temperature, and R-ratio with respect to fatigue lifetime. All stress inputs were $\log_{10}$-scaled and paired with corresponding log-scaled lifetime values to ensure numerical stability and to reflect the wide range of stress-life behavior commonly observed in fatigue datasets. Because the ultimate tensile strength (UTS) and endurance limit values were inherently embedded within the maximum stress values, no additional feature engineering was necessary to encode these physical thresholds into the model.

The network architecture comprises 25 fully connected hidden layers with 25 neurons in each layer. ReLU activation functions were employed throughout to ensure nonlinear learning capability without saturation. Notably, no batch normalization or regularization (e.g., L1, L2, or dropout) was applied during training, as the dataset generated from the Chaboche model was dense and highly structured, reducing the risk of overfitting.

The model was trained using the Adam optimizer with a learning rate of 1×10^{-4} and a mini-batch size of 3.5% of the total training data. The training was carried out over 250 epochs with the mean squared error (MSE) serving as the loss function:

$$\mathcal{L}_{\text{MSE}} = \frac{1}{n} \sum_{i=1}^{n} \left(\log_{10}(N_i) - \log_{10}(\hat{N}_i) \right)^2 \tag{3.13}$$

where N_i denotes the true lifetime and $\hat{N}_i$ the model prediction, both in $\log_{10}$ scale. Importantly, no early stopping or learning rate scheduler was used during training, ensuring that the model converged fully under consistent optimization pressure.

To generate interpretable results, all prediction outputs were inverse-transformed from their $\log_{10}$-scaled form during post-processing. This conversion allows for meaningful comparisons with physical fatigue life data and enables graphical representation across temperature and R-ratio sweeps. The complete training configuration reflects a deliberate emphasis on stability, interpretability, and predictive generalization across the domain of synthetic fatigue curves.

3.4.4 Prediction and Evaluation Results

The model's predictive capability is first evaluated on the Chaboche-generated training dataset. Figure 3.7 and Figure 3.8 illustrate that the artificial neural network (ANN) successfully reproduces fatigue curves across different temperatures and R ratios, capturing the smooth trend between the endurance limit and the ultimate tensile strength (UTS) for each case.

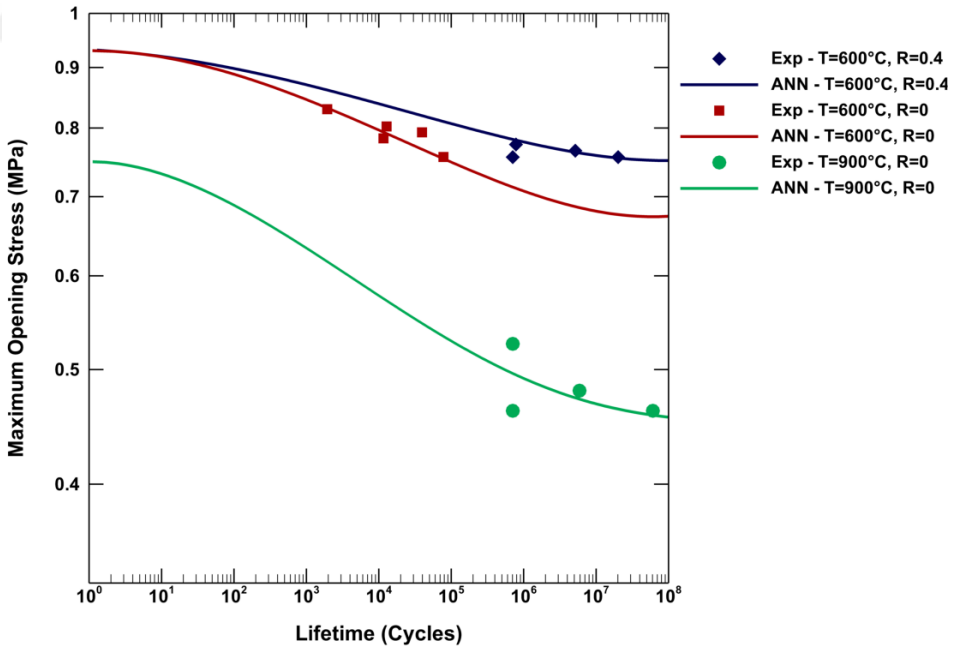

Figure 3.7: Fatigue curves predicted on synthetic training data for different temperatures and R-ratios.

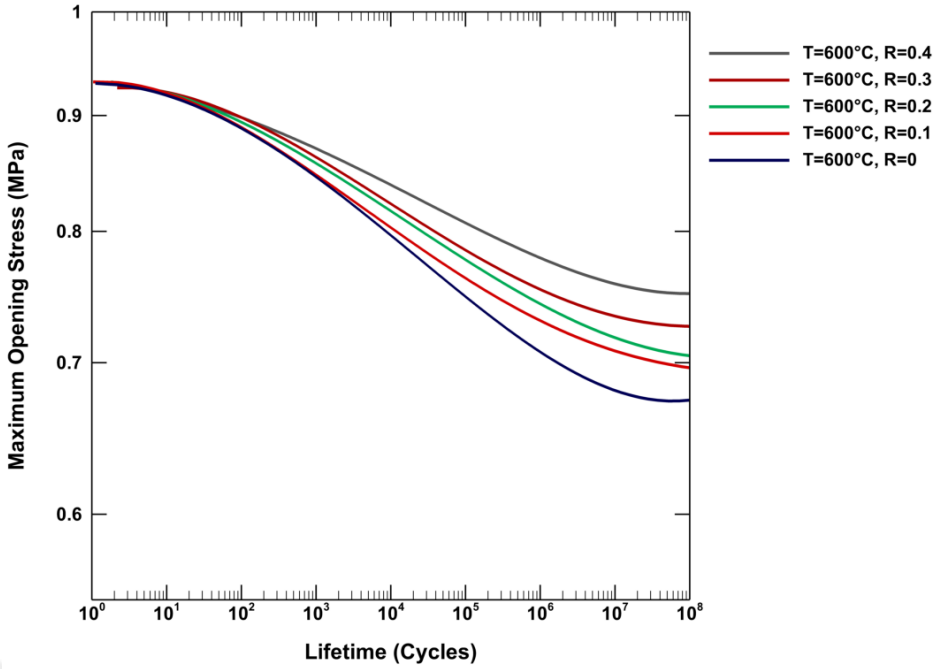

Figure 3.8: Fatigue curves predicted on synthetic training data for varying R-ratios at a fixed temperature.

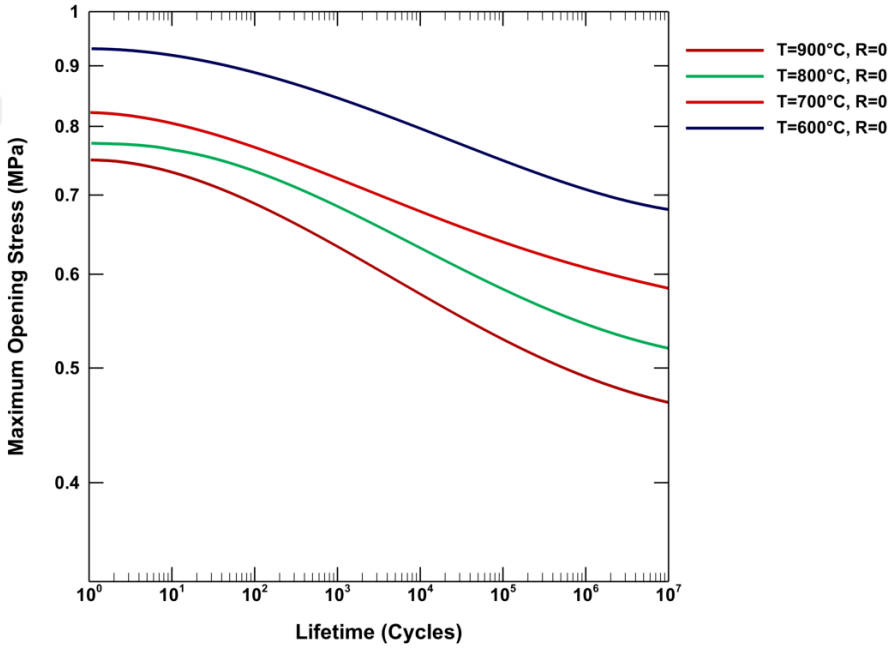

Figure 3.9: Fatigue curves predicted at intermediate temperatures for CMSX-4.

Comparison with original Chaboche model outputs is shown in Figure 3.5 and Figure 3.6, where the ANN demonstrates good alignment with the parametric model

even though it learns from the data only. The trained model is then tested on interpolated temperatures (e.g., 700°C and 800°C), where no original Chaboche curves are provided. As shown in Figure 3.9, the network generalizes temperature effects, maintaining the expected monotonic decrease in UTS and fatigue limit with increasing temperature.

Performance metrics on the validation and independent test sets are reported in Table 3.3. The predictions are performed in $\log_{10}$-scaled stress and lifetime domains and then inverse-transformed for visualization. To interpret model accuracy in the original domain, multiplicative factors are derived from the log-scale errors, showing that small deviations in the log domain correspond to manageable variations in predicted lifetime.

Table 3.3: Validation and test metrics for ANN trained on Chaboche-generated synthetic data.

Dataset	**RMSE ($\log_{10}$)**	**MAE ($\log_{10}$)**	R^2
Validation Set	0.2605	0.1521	0.9919
Test Set	0.2659	0.1549	0.9902

These RMSE and MAE values in the $\log_{10}$-domain correspond to multiplicative uncertainties of approximately 1.82 (RMSE) and 1.42 (MAE), highlighting high prediction fidelity.

3.4.5 Uncertainty Analysis and Model Robustness

To evaluate robustness under slight deviations in input conditions, the model is tested with perturbations of 1%, 5%, and 10% across the input space. Table 3.4 presents the average standard deviation observed in the predicted lifetimes for both validation and test datasets.

Table 3.4: Uncertainty (standard deviation) of lifetime predictions under input perturbations.

Perturbation Level (%)	**Validation SD**	**Test SD**
1%	0.1269	0.1106
5%	0.5397	0.5158
10%	0.9812	0.9581

These results show that the model maintains prediction consistency within the trained domain. While small and moderate perturbations result in stable behavior, 10% input noise leads to significantly increased uncertainty, emphasizing the limits of extrapolation beyond the training distribution.

3.4.6 Discussion on Generalization Capability

The synthetic data generated using the Chaboche damage model enables the ANN to cover the entire SN curve from the endurance limit to the UTS by design. Unlike the physics-based model that requires parameter optimization for each new temperature or condition, the ANN learns a continuous and multi-dimensional mapping from maximum stress, R ratio, and temperature to lifetime, all within a unified architecture.

This flexibility makes the model especially suited for lifetime prediction across operational domains, without retraining or manual reparameterization. However, the temperature interpolation presented in this study (e.g., between 600°C and 900°C) relies on training data limited to those bounds. Broader temperature generalization, or the inclusion of additional failure mechanisms such as dwell time or LCF-HCF interaction, would necessitate either new synthetic data generation or a model capable of adapting.

Since the synthetic dataset is generated using a Chaboche damage model that has been optimized specifically for CMSX-4, the ANN learns fatigue behavior unique to this alloy. Applying the same approach to a different material would require repeating the Chaboche parameter optimization to generate new synthetic data. This process can become impractical for each new alloy. To overcome this limitation, the ANN should be capable of understanding general fatigue trends in metals and adapting its predictions using experimental data from the target material.

This motivates the next section, which explores transfer learning and input expansion strategies to reuse and adapt this model for new conditions and materials with minimal retraining effort.

3.5 Transfer Learning

3.5.1 Introduction

In traditional machine learning pipelines, each new material or loading condition typically requires a full retraining of the model, which is inefficient and computationally costly, particularly in fatigue-critical materials like single crystal superalloys. Transfer learning offers a structured alternative, allowing the reuse of knowledge captured in base models and extending their capabilities through targeted adaptation.

The approach adopted in this thesis involves two distinct transfer strategies: one that reuses the pretrained model directly with minimal fine-tuning, and another that expands the input space to incorporate new physical variables while keeping the original network structure intact. Both methods rely on a base model trained on synthetic fatigue curves generated from the Chaboche damage law. These base models are then transferred and adapted to predict the lifetime of materials using experimental data.

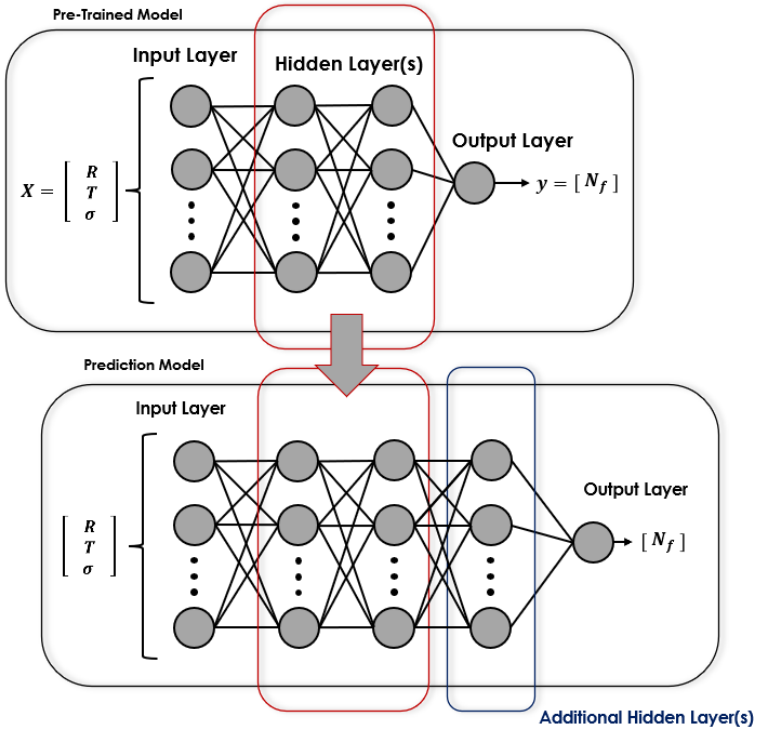

Figure 3.10: Schematic representation of the two transfer learning approaches: direct reuse of pretrained architecture (top), and input expansion with appended hidden layers (bottom).

Figure 3.10 illustrates the structural difference between these two strategies. In the standard transfer model (top), the pretrained input and hidden layers are reused, and only the final output is tuned to adapt to new data. In contrast, the input expansion approach (bottom) maintains the pretrained layers but appends new hidden layers after them. This allows for the integration of additional features or modified physics without altering the original learned relationships.

In the following sections, both transfer methods are implemented and evaluated independently for two types of datasets:

- A **Single Crystal Superalloy Dataset** (CMSX-4), representing materials with complex, temperature-enhanced strength up to a peak threshold before rapid degradation.
- A **Generic Metal Dataset**, covering materials with more conventional UTS vs temperature behavior and isotropic response characteristics.

Both methods are trained on Chaboche-simulated data before being transferred to experimental domains. Their training behavior, generalization capabilities, and structural advantages are analyzed comparatively across material types and modeling configurations.

3.5.2 Synthetic Data Generation

In fatigue modeling, temperature plays a crucial role in both crack initiation and propagation behavior. The concept of *effective temperature* has emerged to capture the cumulative thermal effects on material degradation, including time-dependent deformation mechanisms such as creep and oxidation. This term refers not only to the instantaneous mechanical temperature but also to the operational thermal load's influence over the lifetime of the component [38, 39]. Neu and Sehitoglu [38] introduced a framework that accumulates damage from fatigue, oxidation, and creep, providing a foundational model for thermomechanical fatigue. Later, Cai et al. [39] formalized the concept of effective temperature as a means to incorporate cyclic thermal history into fatigue life prediction models.

Single Crystal Superalloy Dataset

Nickel-based single crystal superalloys such as CMSX-4 exhibit a distinct UTS vs temperature profile. Unlike conventional metallic materials, their UTS increases slightly with temperature up to approximately 600°C due to enhanced dislocation mobility and solid solution strengthening. The material reaches its maximum UTS around 800°C. At higher temperatures, however, microstructural degradation mechanisms—such as γ' coarsening and diffusion-assisted softening—lead to a steep drop in strength.

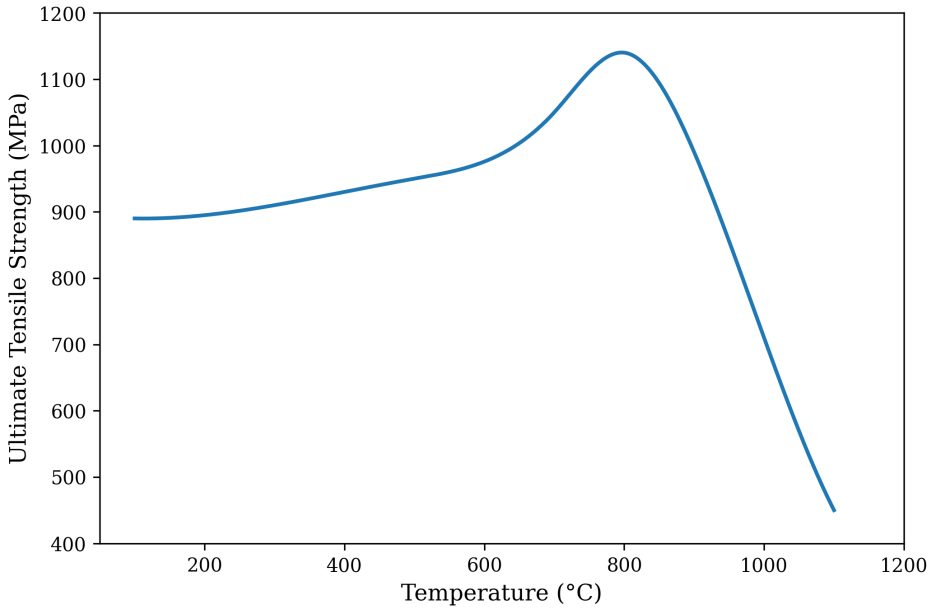

Figure 3.11: Ultimate tensile strength (UTS) versus temperature behavior of CMSX-4 single crystal superalloy. The figure is inspired by data trends reported in Sengupta et al. [87].

To capture these trends in fatigue performance, synthetic fatigue curves were generated using the Chaboche model across 9 temperature points, with 8 R-ratios per temperature. A distinct parameter set was optimized for each temperature to reflect the temperature-dependent fatigue resistance of CMSX-4. The full table of optimized Chaboche parameters is provided in Appendix A.

Representative SN curves at $R = -1$ are shown in Figure 3.12. Curves for other R-ratios are included in Appendix B.

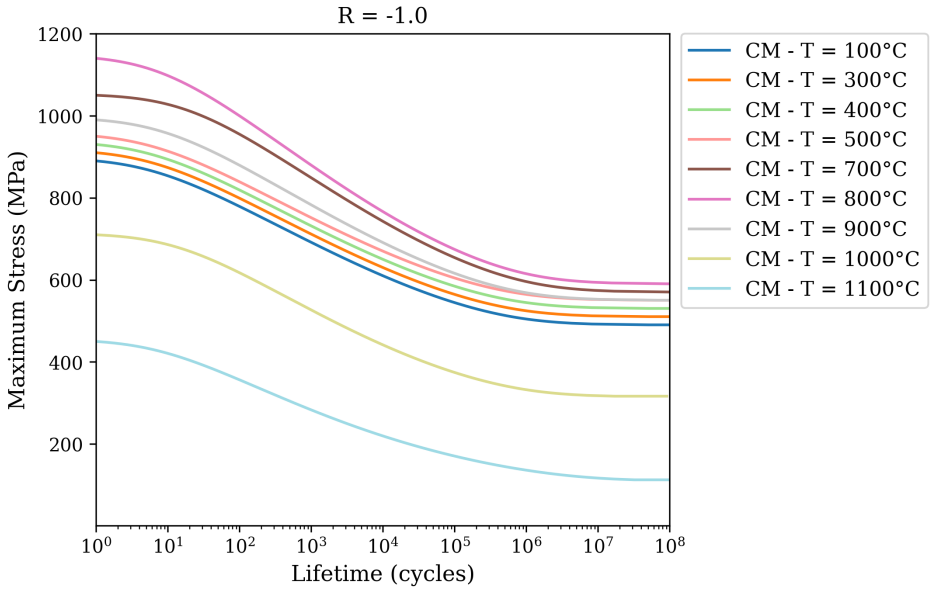

Figure 3.12: Synthetic SN curves for CMSX-4 at $R = -1$ across 9 temperatures.

Generic Metal Dataset

For polycrystalline engineering metals—grouped here as the Generic Metal Dataset—the ultimate tensile strength (UTS) initially remains stable up to a certain threshold temperature, referred to as the effective temperature, beyond which it begins to decline sharply. The effective temperature varies depending on the metal type: for steels, it typically ranges between 300–400°C; for aluminum alloys, it is around 150–200°C; and for nickel-based superalloys, such as CMSX-4, it is considerably higher, often near 600°C. The sharp decline in UTS beyond this effective temperature is nonlinear and results from thermal softening, enhanced dislocation motion, and microstructural degradation as the material approaches its melting temperature.

Since the UTS behavior of CMSX-4 is unusual compared to generic engineering metals—showing strength retention up to significantly higher temperatures—a generalized dataset representing most metals was created by selecting an effective temperature of 400°C. In this synthetic dataset, the UTS is designed to exhibit a slight reduction from room temperature to 400°C due to mild thermal relaxation, followed by a steep drop as the temperature approaches the melting point. This approach allows the dataset to capture the typical mechanical response of common engineering metals under elevated temperature conditions.

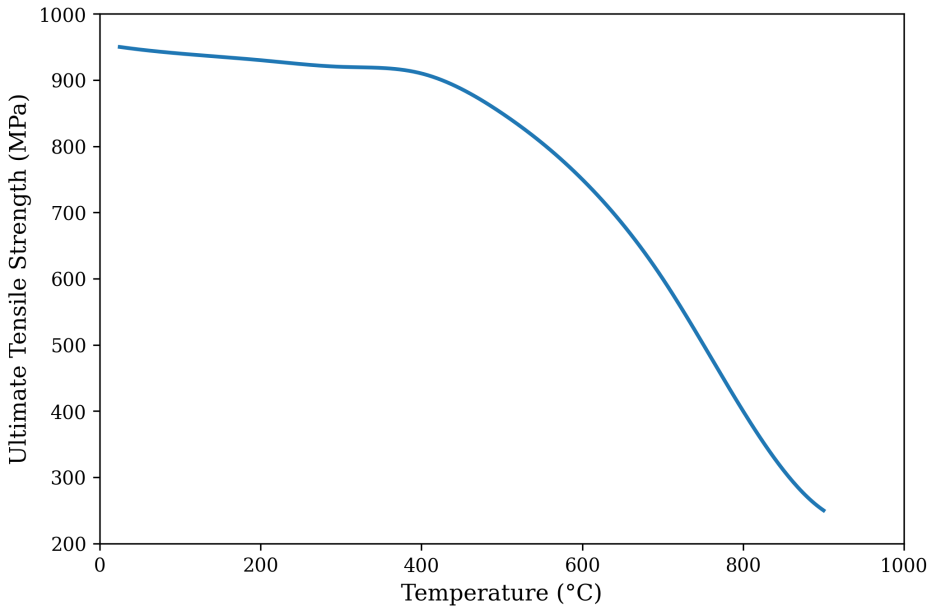

Figure 3.13: UTS vs. temperature behavior of the Generic Metal Dataset where effective temperature is determined as $400°C$.

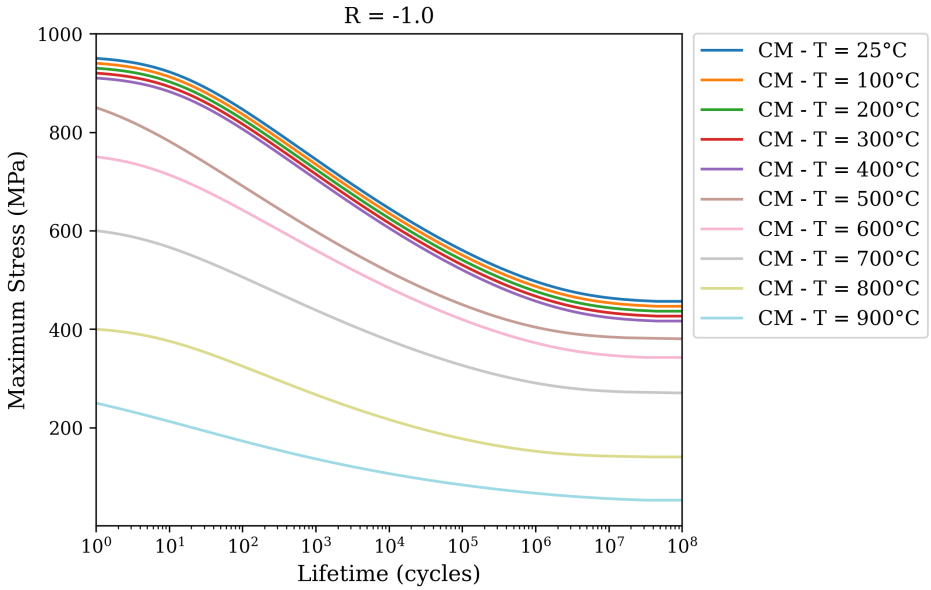

Figure 3.14: Synthetic SN curves for the Generic Metal Dataset at $R = -1$ across 10 temperatures.

To construct a broad and realistic training space for this material class, fatigue curves were generated using 10 different temperature levels, each combined with 8 R-ratios. As with the superalloy dataset, a separate set of Chaboche parameters was optimized at each temperature. These are listed in Appendix A. Figure 3.14 displays the gener-

ated SN curves at $R = -1$, representative of the training distribution. Additional SN curves for other R values are available in Appendix B.

Single Crystal Superalloy Dataset

The ANN model trained on Chaboche-generated fatigue data for CMSX-4 follows the same architectural and training configuration as described previously. It processes $\log_{10}(\sigma_{max})$, R-ratio, and temperature as normalized inputs and returns $\log_{10}(N_f)$ as output. The network consists of 15 hidden layers with 25 neurons each, followed by 10 hidden layers with 15 neurons, all with ReLU activation. Training is performed using the AdamW optimizer with a learning rate of 1×10^{-5}, weight decay of 1×10^{-4}, batch size of 100, and a total of 300,000 epochs using the MAE loss function.

Figure 3.15 presents the prediction versus validation comparison, confirming the model's strong generalization on unseen synthetic data. Most scattering occurs near the endurance limit, where fatigue life predictions diverge asymptotically.

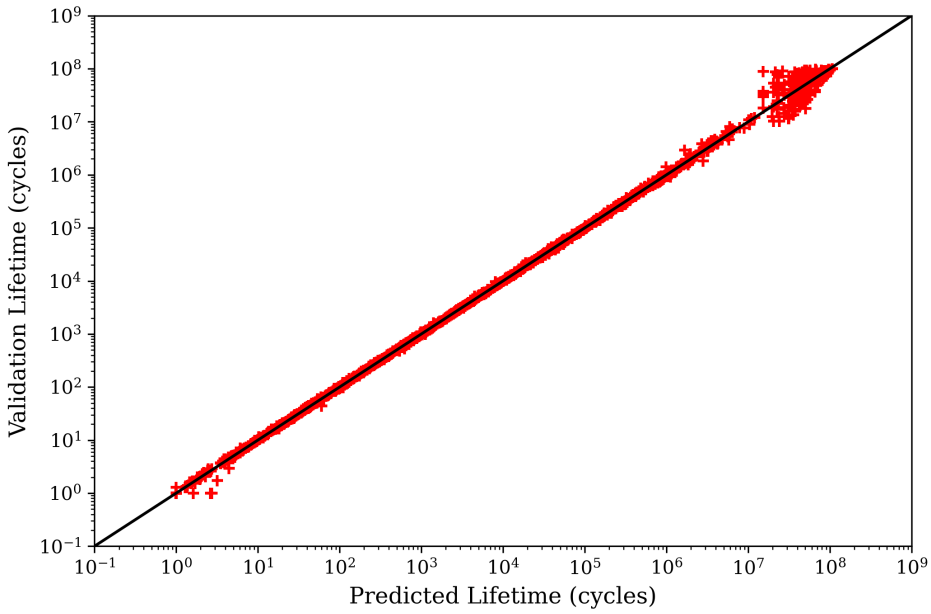

Figure 3.15: Predicted vs. validation data for CMSX-4 training.

The predicted SN curves at $R = -1$ across the full temperature range are shown in Figure 3.16. The model captures the fatigue lifetime trends across both low and high cycle regimes, showing coherence with the underlying Chaboche predictions.

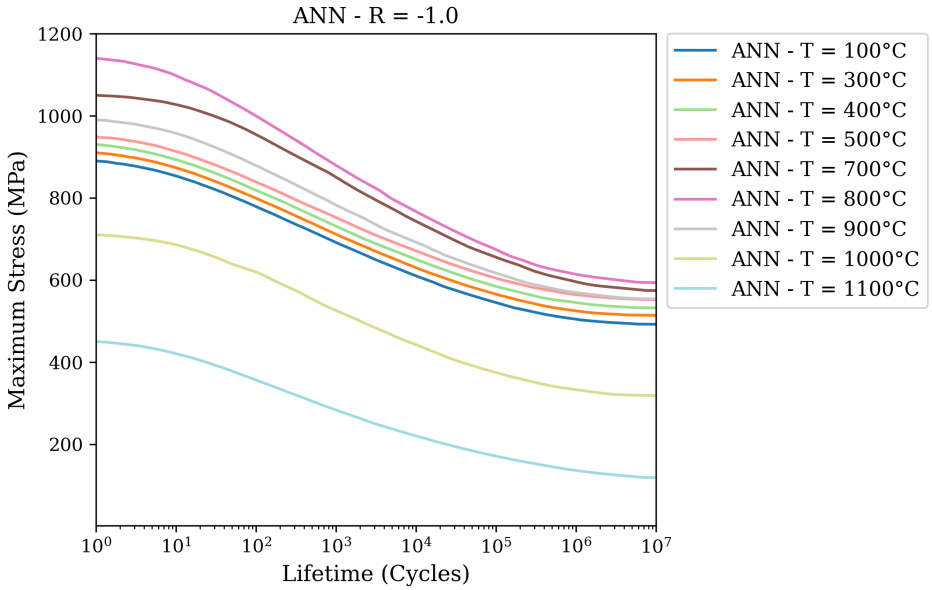

Figure 3.16: Predicted SN curves on Chaboche-generated CMSX-4 training data for $R = -1$.

Goodman behavior at a fixed lifetime of 10^5 cycles is illustrated in Figure 3.17. The model reflects the expected linear degradation with increasing mean stress, aligned with the Chaboche formulation.

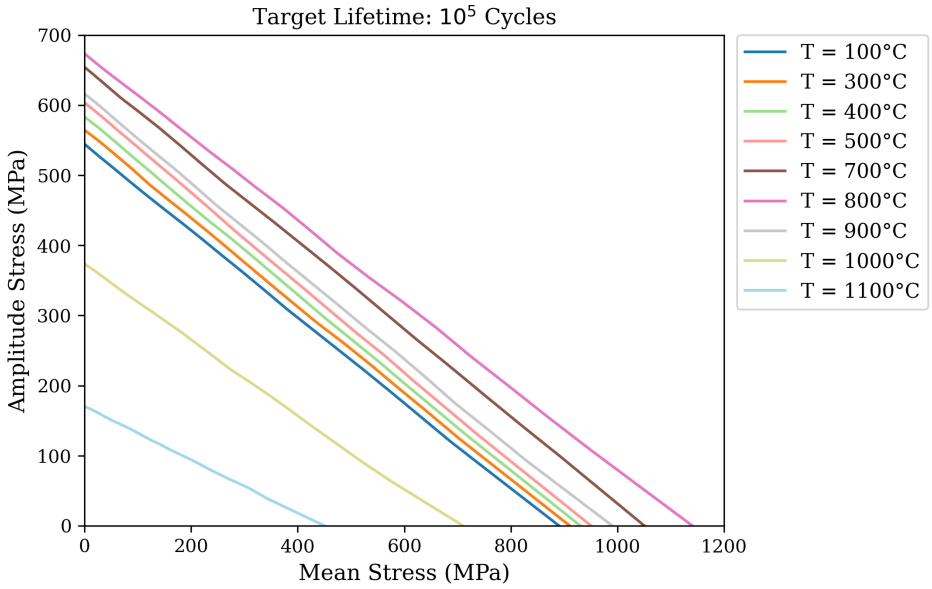

Figure 3.17: Goodman diagram at 10^5 cycles across different temperatures for CMSX-4 training data.

The model's training and validation metrics are summarized in Table 3.5. With an R^2 score above 0.998 and an average scatter of approximately 0.1, the model demonstrates high fidelity and robustness within the synthetic fatigue domain.

Table 3.5: Training and validation performance for the ANN model trained on CMSX-4 Chaboche data.

Metric	Training	Validation
MAE Loss	0.0308	0.0326
R^2	0.9985	0.9986

Further Goodman diagrams for various target lifetimes at different temperatures are provided in Appendix B.

Generic Metal Dataset

The ANN model trained on synthetic data for the Generic Metal Dataset uses the same architecture and training strategy as the CMSX-4 model. It comprises 15 hidden layers with 25 neurons each, followed by 10 hidden layers with 15 neurons, all using ReLU activation. The input features—$\log_{10}$(maximum stress), R-ratio, and temperature—are normalized, and the output is the normalized $\log_{10}$(lifetime). Training was performed with the AdamW optimizer using a learning rate of 1×10^{-5}, weight decay of 1×10^{-4}, and a batch size of 100. The model was trained for 300,000 epochs using MAE as the loss function.

Table 3.6 summarizes the training and validation performance. The model yields high fidelity, with R^2 values above 0.998 for both datasets. A scatter margin of approximately 0.1 is observed, particularly in the asymptotic regime near the endurance limit.

Table 3.6: Training and validation performance for the ANN model trained on Generic Metal synthetic data.

Metric	Training	Validation
MAE Loss	0.0308	0.0326
R^2	0.9985	0.9986

Figure 3.18 displays the predicted versus actual lifetimes on the validation set. The ANN demonstrates strong generalization within the synthetic domain, although some deviation is visible near the endurance limit due to the sharp asymptotic behavior of lifetime predictions.

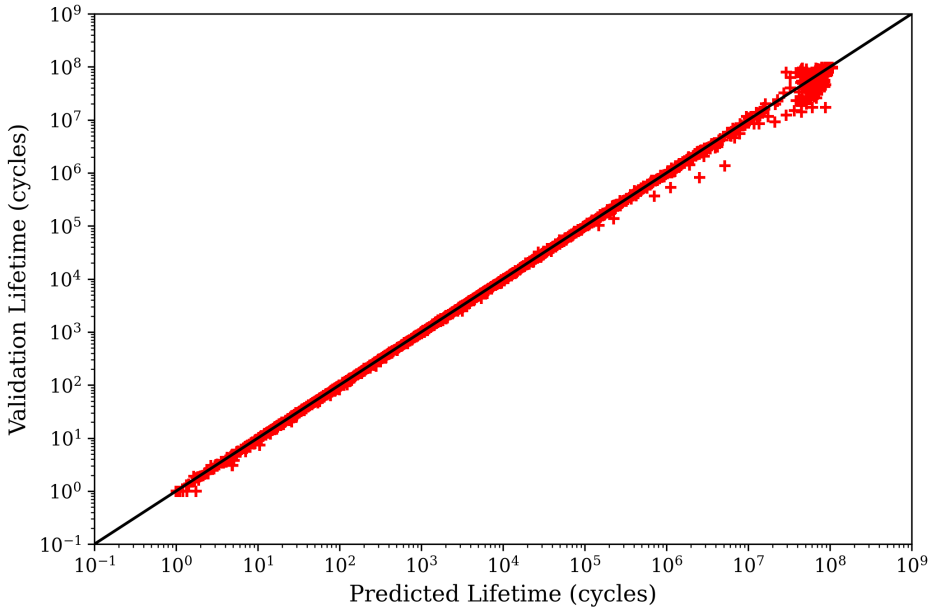

Figure 3.18: Predicted vs. validation data for Generic Metal training.

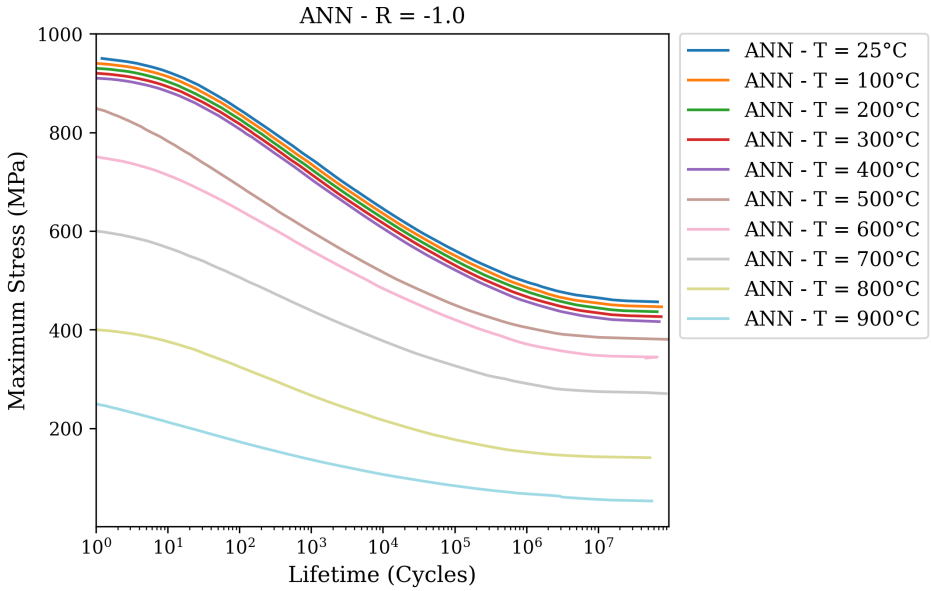

Figure 3.19: Predicted SN curves on Chaboche-generated Generic Metal training data for $R = -1$.

Figure 3.19 presents SN curves generated for $R = -1$ across the training temperature range. The predicted lifetimes show coherent behavior across low-cycle and high-cycle regimes, with slight scatter near extreme stress levels.

To assess model stability on data it was not explicitly trained for, Figure 3.20 shows the Goodman diagram generated at 10^5 cycles across the full R-ratio range. Despite not being exposed to every individual condition during training, the model retains linearity across mean stress, capturing the behavior enforced by the Chaboche model and confirming its robustness.

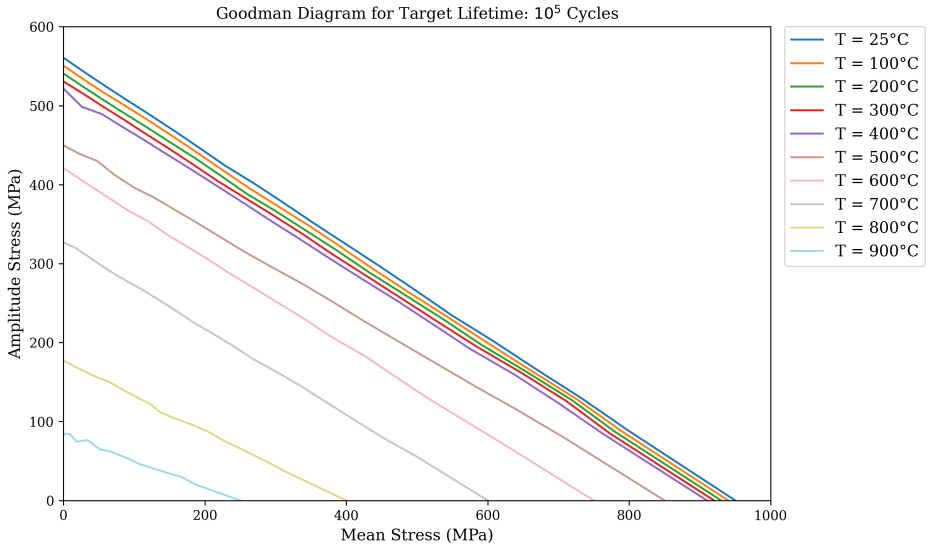

Figure 3.20: Goodman diagram at 10^5 cycles across different R-ratios for Generic Metal training data.

Additional Goodman diagrams for various lifetimes at different temperatures are provided in Appendix B.

3.5.3 Transfer to Experimental Data

When transferring machine learning models to small experimental datasets, conventional validation techniques, such as holding out a fixed percentage for validation (e.g., 15%), are not statistically meaningful. This is especially true for fatigue datasets, where the cost and complexity of experimental testing limit the availability of large samples. To address this issue, the *Leave-One-Out Cross-Validation* (LOOCV) method is applied for evaluating the transferred models.

Validation with Leave-One-Out Cross-Validation (LOOCV)

LOOCV is a special case of k-fold cross-validation where $k = n$, with n being the number of available data points. In this approach, the model is trained n times. Each time, a different single data point is held out as the validation sample, while the remaining $n - 1$ points are used for training. The performance metrics (e.g., MAE, RMSE, R^2) are then averaged across all n iterations to provide a robust estimate of the model's generalization ability.

Mathematically, given a dataset $D = \{(\mathbf{x}_i, y_i)\}_{i=1}^{n}$, the LOOCV procedure is defined as:

$$\text{LOOCV Error} = \frac{1}{n} \sum_{i=1}^{n} \mathcal{L}\left(y_i, f_{-i}(\mathbf{x}_i)\right) \tag{3.14}$$

where f_{-i} denotes the model trained on all samples except the i^{th}, and $\mathcal{L}$ is the chosen loss function (e.g., mean squared error).

This technique ensures every data point is used for validation exactly once and eliminates bias introduced by arbitrary train-test splits. Moreover, it leverages all available data for training in each iteration, which is particularly useful in domains like fatigue testing where each experiment is resource-intensive.

Single Crystal Superalloy Dataset

The base ANN model trained on synthetic CMSX-4 data was transferred to an experimental dataset consisting of 19 fatigue lifetime measurements at temperatures of 600°C (with $R = 0$ and $R = 0.4$) and 900°C (with $R = 0$). These experiments are consistent with those described in Chapter 2. To adapt the pretrained model to the limited experimental data, transfer learning was performed by unfreezing the final 7 hidden layers of the base ANN and appending 5 new hidden layers with 10 neurons each.

Training of the transferred model was conducted using the Adam optimizer with a learning rate of 2×10^{-5}, batch size of 5, and mean absolute error (MAE) as the loss function. No regularization or early stopping criteria were employed, and the training process was carried out for 10,000 epochs.

Given the limited number of available experimental data points, Leave-One-Out Cross-Validation (LOOCV) was adopted to evaluate generalization performance robustly. The validation metrics from the LOOCV procedure, summarized in Table 3.7, indicate strong predictive capability, with an R^2 score of 0.9847. The transferred model demonstrates good fidelity to the experimental data, as evidenced by low training and validation errors.

Table 3.7: LOOCV validation metrics for the transferred ANN model on CMSX-4 experimental data.

Metric	**Training Set**	**LOOCV Validation**
MSE Loss	0.0704	–
MAE Loss	0.1002	0.3935
RMSE	–	0.7568
R^2	–	0.9758

The results demonstrate that the implemented lifetime assessment framework yields consistent agreement with both qualitative and quantitative experimental data. The model successfully captures fatigue crack initiation locations and relative lifetime trends under different loading conditions without requiring further modification to the underlying fatigue damage formulation.

It should be noted that the observed incoherency between certain experimental and predicted results primarily arises from the scattered nature of the experimental data. For cases where multiple experimental lifetimes are observed at the same maximum stress, the model predicts an intermediate value to minimize the overall error and to avoid overfitting to any particular data point.

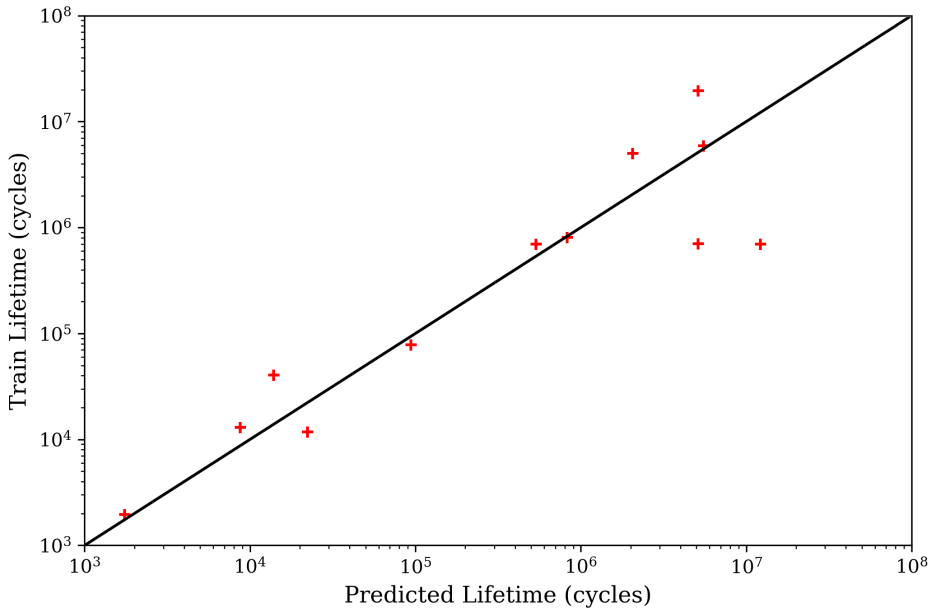

Figure 3.21: Predicted vs. experimental lifetimes on the training set after transfer (Single Crystal Superalloy Dataset).

The effect of the R ratio on fatigue lifetime is clearly visible in the experimental and predicted SN curves. At 600°C, the dataset includes both R = 0.4 and R = 0 conditions. The R ratio, defined as the ratio of minimum to maximum load in a fatigue cycle, significantly influences the lifetime at a given maximum stress.

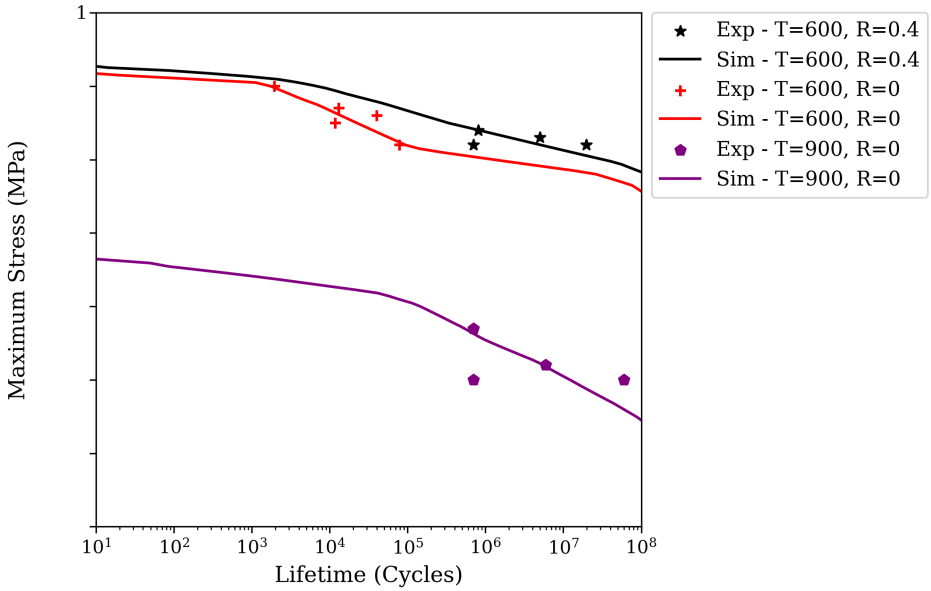

Figure 3.22: Predicted vs. experimental lifetime values for CMSX-4 experimental dataset after transfer.

Lower R values generally correspond to higher mean stresses, which accelerate damage accumulation and reduce fatigue life. This trend is observed in the figure: for the same maximum stress, samples with R = 0 exhibit shorter lifetimes than those with R = 0.4. The transferred ANN model predicts the separation between R = 0 and R = 0.4 SN curves, closely following experimental trends. This result shows that, after fine-tuning with limited data, the network can capture the influence of R ratio on fatigue life.

Generic Metal Dataset

The transferred model is evaluated using experimental fatigue data for AISI 4340 steel, under $R = -1$ at three temperature levels: 315°C, 427°C, and 538°C. UTS data is known and excluded from training to test generalization. A total of 20 lifetime measurements are used.

The transfer is performed by unfreezing only the last hidden layer of the pretrained model and appending five new layers, each with 10 neurons. The training setup includes 2000 epochs, a learning rate of 2×10^{-5}, batch size of 5, and MSE as the loss function. No regularization or early stopping is used.

The LOOCV performance metrics are summarized in Table 3.8. The model demonstrates a high R^2 score and acceptable error margins, especially considering the small sample size and complex temperature-dependent fatigue behavior.

Table 3.8: LOOCV validation metrics for transferred model on experimental data (Generic Metal Dataset).

Metric	Training Set	LOOCV Validation
MSE Loss	0.0919	–
MAE Loss	0.1919	0.4945
RMSE	–	0.7778
R^2	–	0.9847

The predicted versus true lifetimes on the training set are shown in Figure 3.23, demonstrating good alignment between model output and ground truth, even with limited training data.

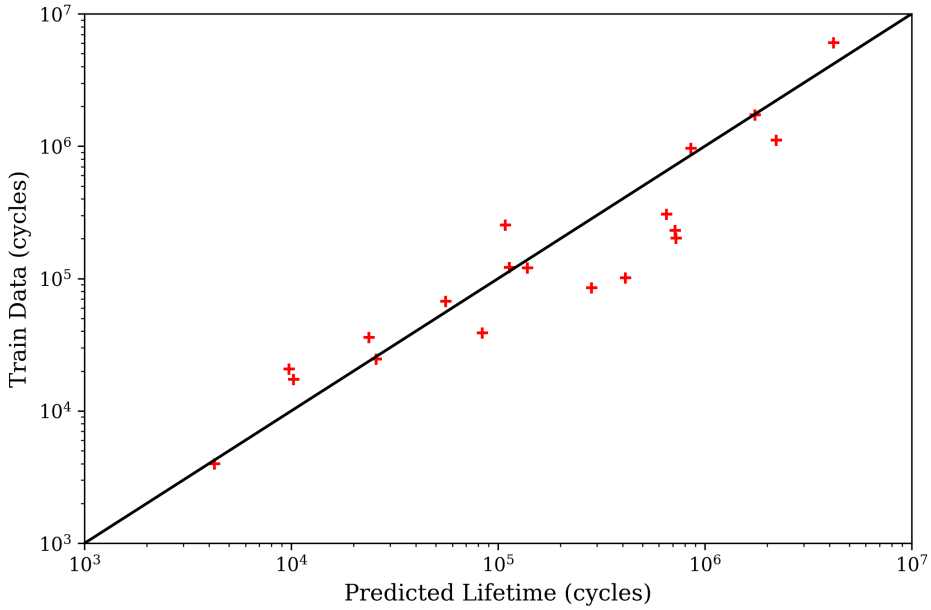

Figure 3.23: Predicted vs. experimental lifetimes on training set after transfer (Generic Metal Dataset).

Figure 3.24 illustrates the predicted SN curves from the transferred model on the AISI 4340 experimental domain. These predictions capture the general fatigue trend and extrapolate reasonably beyond observed points.

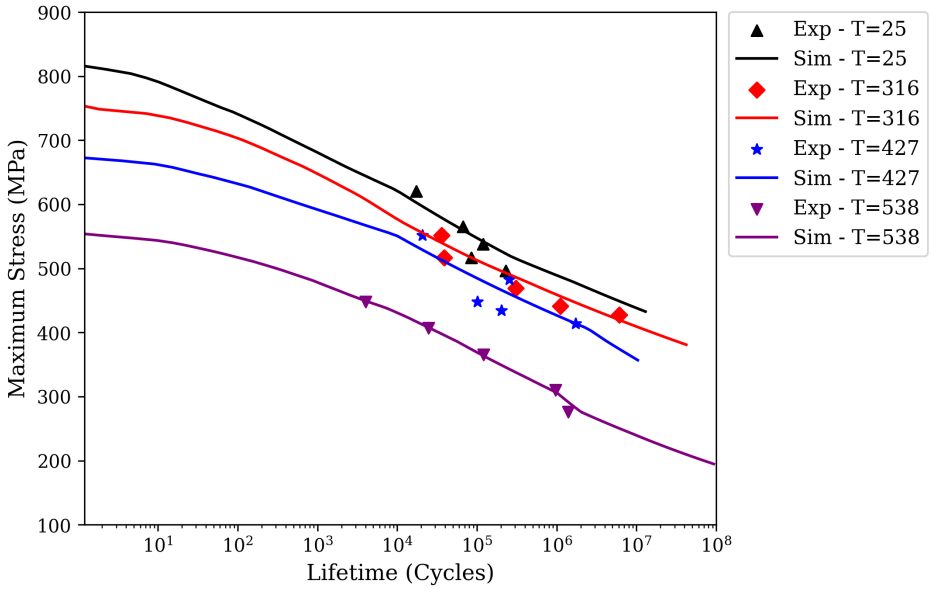

Figure 3.24: Predicted SN curves from transferred model based on experimental data for AISI 4340.

3.6 Input Expansion Approach

3.6.1 Method Description

In deep learning applications for scientific modeling, it is often beneficial to extend a trained neural network to incorporate additional physical input variables without retraining the entire architecture from scratch. This technique is commonly referred to as **input expansion**. In such cases, a base model—previously trained on a limited set of input features—is retained and new physical features are introduced via auxiliary input branches or concatenation blocks.

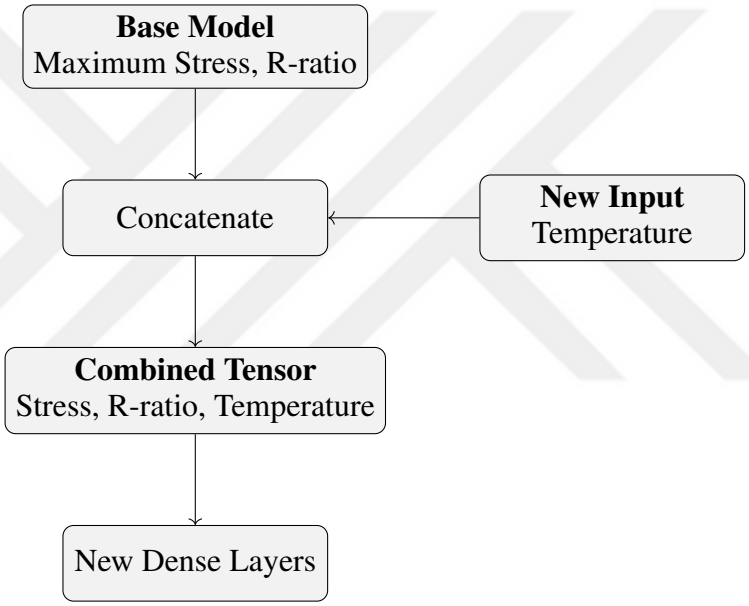

Figure 3.25: Input expansion scheme of Model 2. The base model, trained on maximum stress and R-ratio, is reused and combined with the new temperature input at the concatenation stage. The resulting combined tensor is processed through newly added dense layers to learn the expanded input space.

Input expansion allows for reuse of the learned representations in the earlier layers, especially when the initial model captures general patterns in the data. This is particularly advantageous in fatigue modeling, where new variables like temperature, microstructure descriptors, or environmental conditions may become available after initial training. A schematic representation of the input expansion strategy used in this study is shown in Figure 3.25.

The initial layers of the base network are kept frozen, while a new temperature input is concatenated at a later stage. The subsequent layers are then fine-tuned to account for the new input dependency.

Base Model Training (Model 1)

Model 1 serves as the foundation for the input expansion strategy. It is trained solely on the relationship between maximum stress and R-ratio, excluding temperature as an input. The training dataset consists of Chaboche-generated fatigue lifetimes covering 20 distinct R-ratios ranging from -1 to 0.9 in increments of 0.1. The corresponding stress-lifetime data spans the fatigue lifetime domain from 10^1 to 10^7 cycles, while data near the asymptotic UTS and endurance limit regions are excluded to reduce complexity and stabilize learning performance.

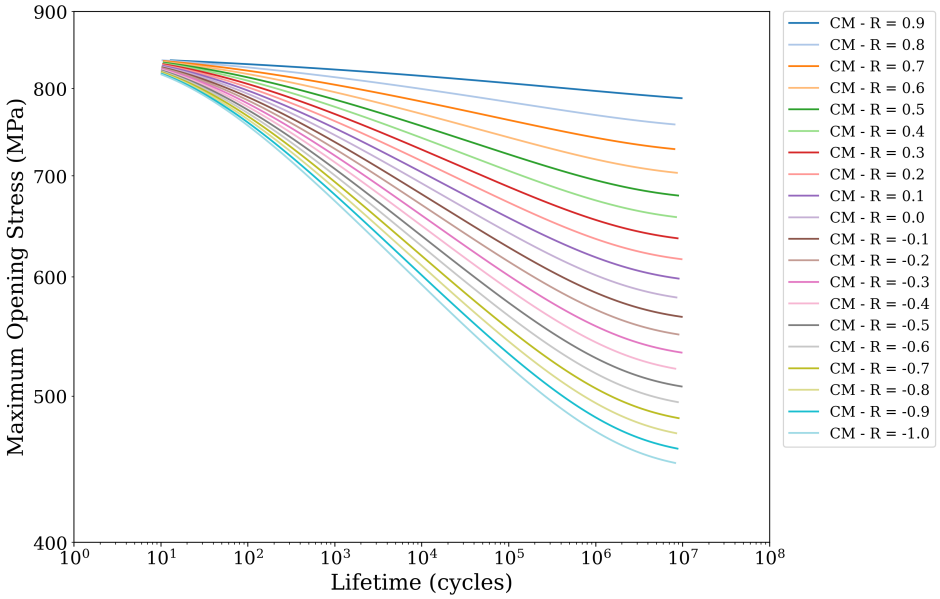

Figure 3.26: Synthetic SN curves for the Model 1's Dataset across 20 R Ratios.

All input features are log-scaled and normalized, and the output fatigue lifetimes are also expressed in normalized $\log_{10}$-scale. The architecture comprises 10 hidden layers with 25 neurons each, followed by 5 layers with 10 neurons, all using ReLU activation. No regularization or normalization techniques are applied within the layers to preserve baseline simplicity. The model is trained using the Adam optimizer with a learning rate of 8×10^{-5}, a batch size of 100, and a total of 3000 epochs. The loss

function is MAE, and R^2 is monitored as a performance metric.

Table 3.9: Training and validation performance for the base Model 1 prior to input expansion.

Metric	Training	Validation
MAE Loss	0.0188	0.0179
R^2	0.9996	0.9997

The prediction accuracy is visually confirmed by the predicted vs. validation plot in Figure 3.27. The agreement remains robust throughout the fatigue domain, without significant deviation near UTS or endurance limit values due to the exclusion of those regimes during training.

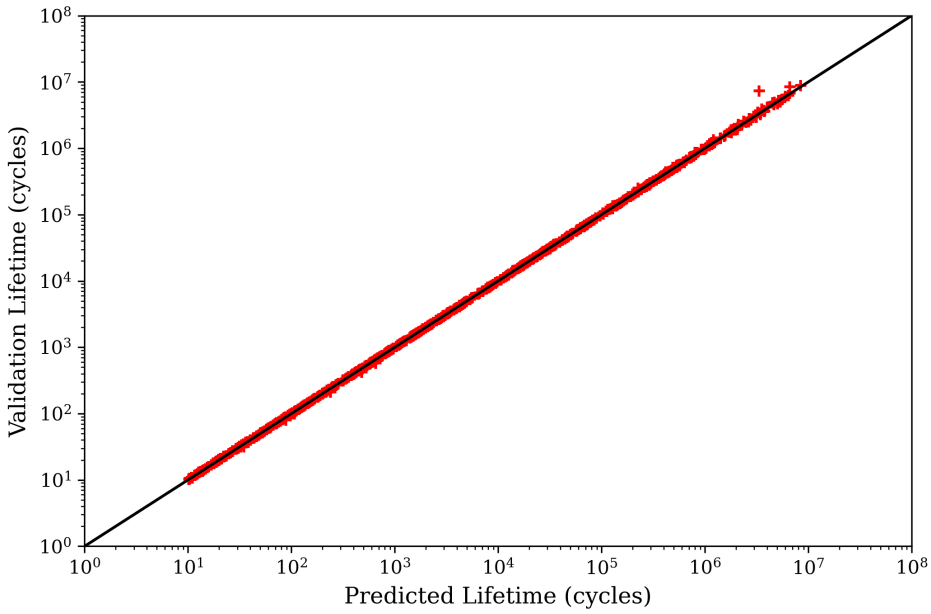

Figure 3.27: Predicted vs. validation values for Model 1 across 20 R-ratios.

To further evaluate the model's performance, SN curves generated on the training dataset are presented in Figure 3.28, and the corresponding Goodman diagram for different target lifetimes is shown in Figure 3.29. These visualizations highlight the model's effective learning of the fatigue lifetime distribution across varying stress levels and mean stress conditions.

In Figure 3.28, the model-predicted SN curves are plotted for a wide range of stress ratios (R values). The curves demonstrate the expected trend where higher R ratios

correspond to higher maximum opening stresses for a given lifetime, while lower R ratios lead to a steeper reduction in stress with increasing cycles. The model captures the continuous transition of the SN response across the full spectrum of R values, from fully reversed ($R = -1$) to tension-tension loading ($R = 0.9$). Furthermore, the consistency and smoothness of the SN curves indicate that the model generalizes well over the training domain, with no abrupt discontinuities or unrealistic oscillations across lifetimes from 10^1 to 10^7 cycles.

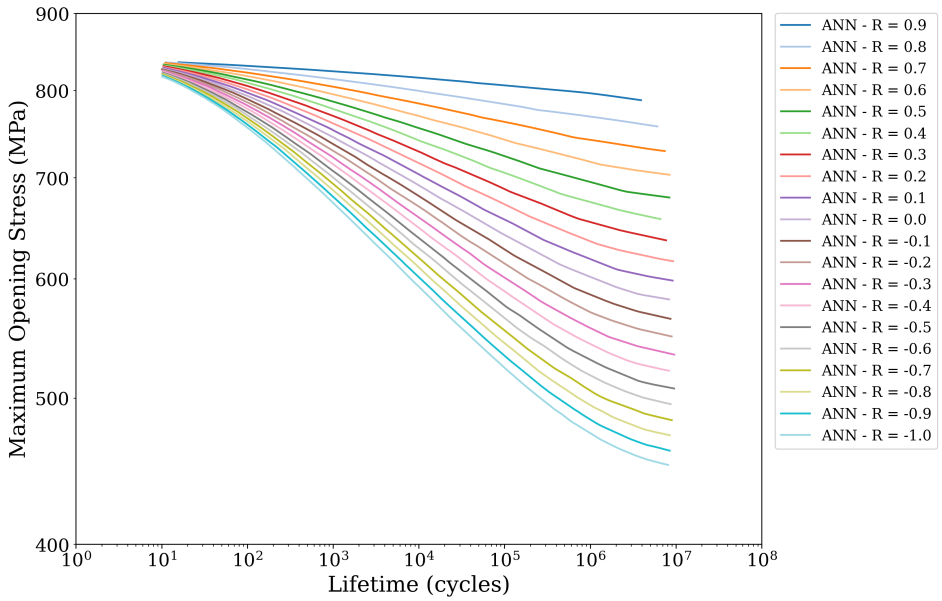

Figure 3.28: SN curves predicted by Model 1 across various R-ratios from training data.

Figure 3.29 illustrates the Goodman diagram generated by the model for different target lifetimes. Each line represents the predicted safe boundary of amplitude and mean stress combinations for a specific number of cycles. The model successfully reproduces the expected linear decay of amplitude stress with increasing mean stress, with clear distinctions between the boundaries for short and long lifetimes. This suggests that the model accurately reflects the combined effects of mean stress and stress amplitude on fatigue performance, supporting its suitability for fatigue life prediction across a broad stress space.

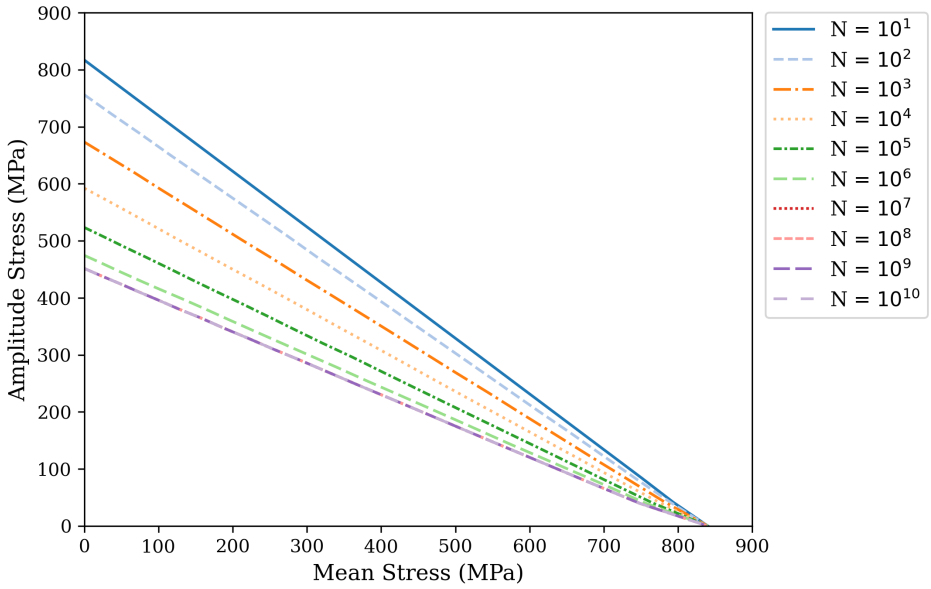

Figure 3.29: Goodman diagram at multiple target lifetimes predicted by Model 1.

Input Expansion on Single Crystal Superalloy Dataset (Model 2)

Model 2 is derived by expanding the input features of Model 1 to include temperature, in addition to maximum stress and R-ratio. The original base model—trained on 20 R-ratios—is transferred with all hidden layers preserved, while only the last five layers are left unfrozen during the new training phase. To capture the more complex temperature-dependent fatigue behavior in CMSX-4, 25 additional layers with 50 neurons and 5 layers with 15 neurons are appended after the transferred portion of the model.

The new training dataset consists of Chaboche-generated CMSX-4 data at 9 different temperatures, each associated with three R-ratios: -1, 0, and 0.8. Data regions near the endurance limit and ultimate tensile strength are excluded to ensure numerical stability and reduce extrapolation issues during training.

The model is trained using the AdamW optimizer with a learning rate of 1×10^{-5}, a weight decay of 1×10^{-4}, batch size of 100, and 500,000 training epochs. The loss function is mean squared error (MSE), and R^2 is used as the evaluation metric. All input features—including temperature—are normalized after log-scaling the stress and lifetime values.

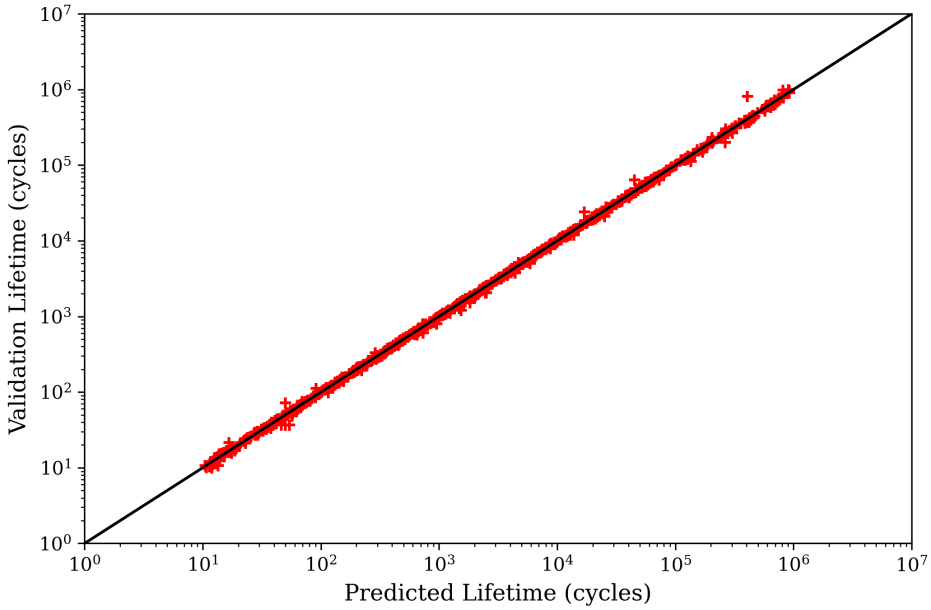

Figure 3.30: Predicted vs. validation values for Model 2 for single crystal dataset.

Evaluation metrics for the training and validation sets are provided in Table 3.10. The model exhibits near-perfect fit within the trained regions, with $R^2 > 0.9995$, and a very low scattering error. However, it fails to generalize reliably outside of the trained R-ratios, making the Goodman diagrams inconsistent across extrapolated domains.

Table 3.10: Performance of Model 2 trained on input-expanded CMSX-4 dataset.

Metric	**Training**	**Validation**
MSE Loss	5.3528×10^{-4}	8.3975×10^{-4}
R^2	0.9997	0.9995

Figure 3.31 shows the predicted SN curves on the training data at $R = -1$, exhibiting excellent alignment across low-cycle and high-cycle fatigue regimes. As noted, Goodman diagrams are omitted due to instability outside trained domains.

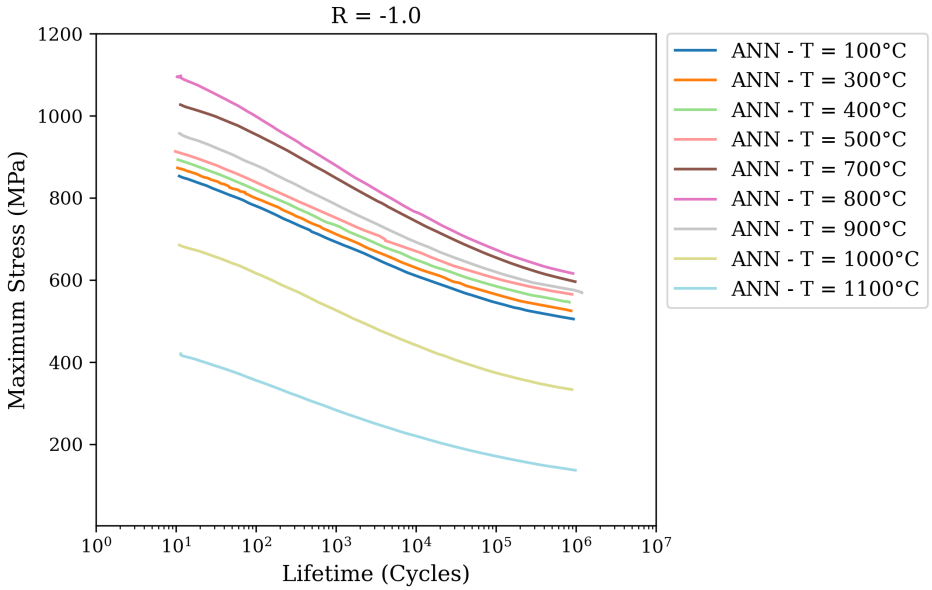

Figure 3.31: SN curves predicted by Model 2 for CMSX-4 training data at $R = -1$.

Input Expansion on Generic Metal Dataset (Model 2)

The same input expansion strategy is applied to the Generic Metal Dataset, but with slight architectural differences to accommodate the smoother and more monotonic ultimate tensile strength (UTS) versus temperature relationship typically observed in conventional metallic materials. Instead of fully retraining the model, the base Model 1 is reused through transfer learning, with only the last two layers unfrozen. This partial unfreezing allows the model to fine-tune its predictions while retaining the general stress–lifetime mapping learned from the initial training on synthetic data.

To capture the thermal behavior of generic metals more effectively, a new network block is appended to the existing architecture. This added block consists of 15 hidden layers with 25 neurons each, followed by 5 layers with 15 neurons, maintaining ReLU activation throughout. The final model architecture receives normalized values for the three input features: temperature, maximum stress, and stress ratio (R-ratio). This tailored structure ensures the network can adjust to the smoother fatigue response surfaces typical of these materials without overfitting to nonlinearities that are more characteristic of single crystal superalloys.

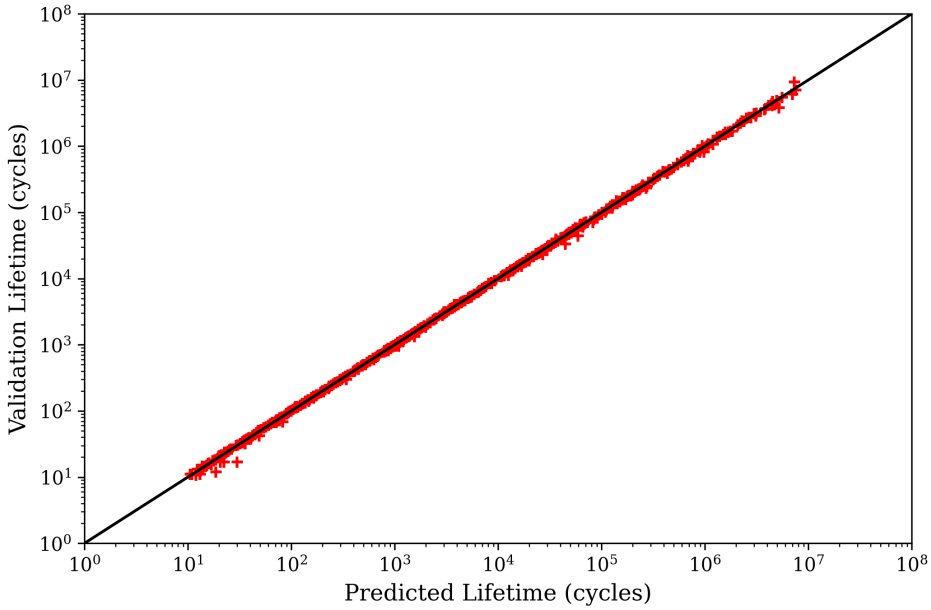

Figure 3.32: Predicted vs. validation values of Model 2 for generic metal dataset.

The training dataset spans 10 different temperatures with three R-ratios (-1, 0, 0.8) per temperature. Like the CMSX-4 case, data near the endurance limit and UTS are excluded to eliminate instability in training and ensure the model captures the stable fatigue range. The model is trained using AdamW with a learning rate of 5×10^{-5}, weight decay of 1×10^{-4}, batch size of 100, and 350,000 epochs. Loss is computed via MSE, and the performance is tracked using R^2.

Evaluation metrics are presented in Table 3.11. As with the superalloy model, this architecture demonstrates exceptional training and validation fit, but loses reliability when extrapolating outside the input training domain.

Table 3.11: Performance of Model 2 trained on input-expanded Generic Metal dataset.

Metric	**Training**	**Validation**
MSE Loss	5.6142×10^{-4}	9.5044×10^{-4}
R^2	0.9998	0.9996

The predicted SN curves for $R = -1$ are shown in Figure 3.33, illustrating a strong correlation with the generated training data. Goodman diagrams are excluded due to inconsistencies in extrapolated R-ratios and temperature combinations.

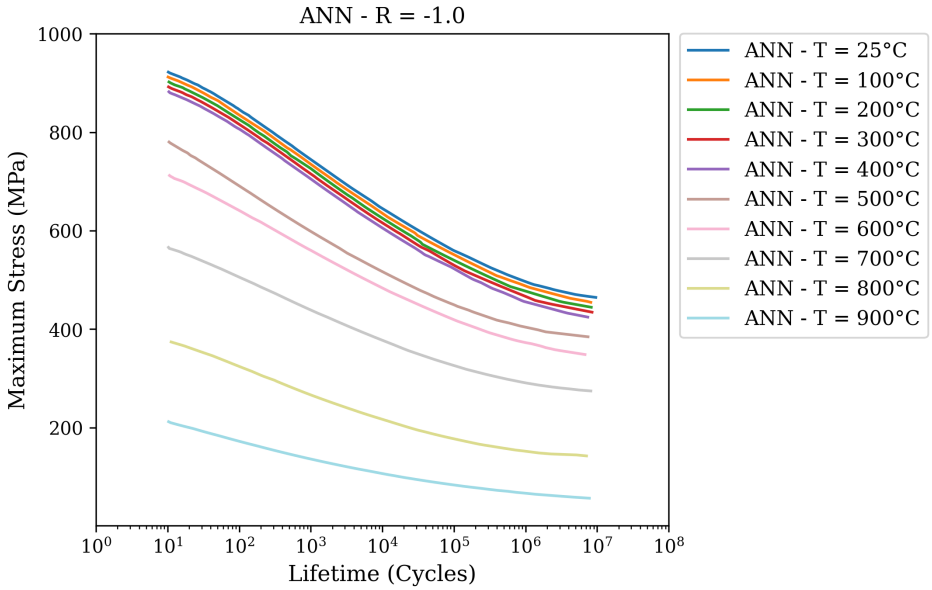

Figure 3.33: SN curves predicted by Model 2 for the Generic Metal Dataset at $R = -1$.

In this approach, only the SN curves generated on the training data are presented for Model 2, as the transferability of the mean stress effect requires further adjustment. The frozen layers inherited from Model 1 continue to enforce the mean stress dependency captured in Figure 3.29, while the newly added layers of Model 2 attempt to learn the temperature-dependent fatigue behavior introduced by input expansion. T

The linear relationship between amplitude and mean stress of Model 2's dataset is not fully interpolated across the stress space, as the model preserves the original mean stress effect at untrained R-ratios and learns new relationships at trained ones, leading to inconsistencies. These findings indicate that further tuning and architectural refinement are necessary to enhance the robustness of the input expansion method and achieve reliable fatigue life predictions across both the original and expanded input domains.

CHAPTER 4

PARAMETER OPTIMIZATION WITH NEURAL NETWORKS

4.1 Introduction

Parameter optimization in constitutive material modeling presents major challenges because internal state variables are tightly coupled and the models exhibit non-linear, path-dependent behavior. Traditional methods reduce complex mechanical responses to scalar objectives, such as differences in yield stress or initial stiffness, which can miss critical features like hysteresis and strain hardening. Modern methods employ full-field inverse techniques, including response-surface optimization and neural-network-based regression using entire stress–strain curves, to infer constitutive parameters more accurately and robustly than scalar-error approaches [124, 125].

Identifying material parameters within user-defined material subroutines (UMATs) remains a non-trivial task due to the high complexity and coupling of internal state variables in advanced constitutive models [126]. These models frequently involve non-linear and history-dependent behavior that is sensitive not only to the parameter values themselves but also to the simulation environment, including boundary conditions, element types, mesh discretization, and loading rate [27, 28, 127]. As such, a given set of parameters may perform well under one condition but fail under others. Moreover, traditional calibration techniques often overlook these dependencies by assuming simplified, homogeneous deformation conditions.

Classical optimization approaches, such as the Levenberg–Marquardt algorithm, Nelder–Mead simplex method, and genetic algorithms (GAs), typically frame parameter calibration as a single-objective minimization problem [127, 128]. These methods collapse the full material response into scalar objective functions, such as the squared error between simulated and experimental stress-strain curves. While straightforward, this reduction ignores important features of the mechanical response, particularly when material behavior is governed by multiple mechanisms acting simultaneously. Highly coupled models, such as those involving isotropic and kinematic hardening or rate-dependent plasticity, often produce complex objective landscapes riddled with local minima. Gradient-based methods can be trapped in these minima, while GAs, though more global in nature, are computationally intensive due to the need for repeated finite element evaluations [128].

More fundamentally, scalar objectives fail to represent the multi-faceted character of experimental stress-strain data. Parameters tuned to match yield stress, for example, may fail to capture post-yield hardening or hysteresis behavior in cyclic loading. To overcome these issues, recent studies have advocated for full curve-based or multi-objective optimization techniques. By comparing entire simulated and experimental curves, these methods ensure that different regions of the mechanical response, such as initial yield, hardening, unloading, and reloading, are all accurately captured [127, 129]. For materials with anisotropic or time-dependent behavior, such approaches are essential: they allow the calibration of parameters using multiple loading paths, directions, or strain rates, providing a richer and more reliable inverse identification framework.

To address these limitations, this study proposes a novel data-driven pipeline based on artificial neural networks (ANNs), which directly matches predicted stress-strain curves to simulation data. Rather than fitting isolated curve descriptors, the ANN learns to regress the underlying material parameters from the full stress-strain profile, as computed from finite element simulations involving the target UMAT. This approach allows for a more comprehensive representation of the material behavior, capturing both global trends and local variations in the mechanical response.

The proposed pipeline utilizes three custom-built Python scripts:

1. A parametric study script that generates a grid of simulations across a predefined parameter space,
2. A post-processing script that extracts stress-strain data from simulation output databases (ODB),
3. A neural network-based regression model that learns to infer material parameters from stress-strain curves.

This framework is tested on a simplified constitutive model: finite strain, rate-independent J2 plasticity with Voce-type isotropic hardening. While this case serves as a controlled baseline, the pipeline is designed to scale toward more sophisticated UMATs involving internal variable evolution, anisotropy, or time-dependent effects. Moreover, the proposed ANN-based method offers an alternative to iterative optimization algorithms by bypassing the need for repeated forward simulations during inverse identification, significantly reducing computational overhead once training is complete.

This chapter introduces the optimization workflow in detail, elaborates on the technical design of the input generation and data extraction scripts, and presents a case study validating the pipeline on a synthetic dataset. The results demonstrate the ability of ANNs to accurately regress multiple material parameters from stress-strain curves alone, offering a promising direction for generalizable parameter inversion in computational materials modeling.

4.2 Optimization Workflow

The parameter optimization framework proposed in this work is implemented as a modular, script-driven pipeline that facilitates the inverse identification of constitutive model parameters via supervised regression. The workflow consists of three primary components: input file generation and simulation execution, stress-strain data extraction from finite element outputs, and artificial neural network (ANN)-based prediction of the optimal parameter set. Each component is handled by a dedicated script,

allowing users to flexibly configure the parameter space, extract simulation data in a consistent format, and apply the trained model to experimental or validation datasets.

Figure 4.1 illustrates the overall scheme. The workflow begins with the script INPUTnODBGenerator.psf, which uses the Abaqus ParStudy module to automate the creation of input decks and execute finite element simulations for different parameter combinations. These simulations generate output databases (.odb files) containing stress and strain responses over the full deformation history.

Next, the DataSetCreator.py script processes the generated output databases. It accesses the field output data (stress and strain) for a specified node or integration point across all frames of the loading step. The extracted values are compiled into a structured CSV file (stress-strain.csv), where each row represents a unique parameter set and each column corresponds to a stress or strain increment. For consistent training, the number of increments and data points must be equal across all simulations.

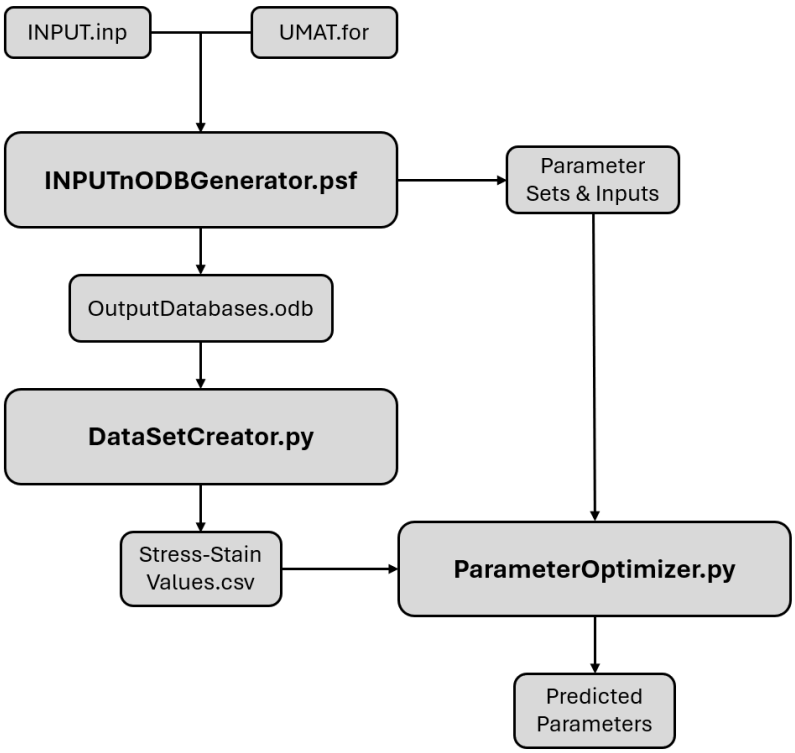

Figure 4.1: Overview of the parameter optimization workflow.

Finally, the ParameterOptimizer.py script merges the stress-strain CSV data with the corresponding input parameters extracted from the Abaqus input files. This consolidated dataset is used to train a regression-based ANN that learns the inverse mapping: given a stress-strain curve as input, the network predicts the underlying parameter set. Once trained, the ANN can be used to predict the parameters corresponding to new input curves, including experimental data that follows the same stress-strain formatting.

This structured workflow ensures separation of concerns: input space definition, simulation automation, data extraction, and regression are decoupled, allowing for scalability to more complex constitutive models and training data configurations. The implementation also accommodates validation and experimental data by enforcing a fixed input structure, ensuring compatibility with the trained model and facilitating generalization analysis. The subsequent sections provide technical details and user instructions for each stage of the workflow.

4.3 Parametric Modeling in Abaqus

A key component of the proposed optimization framework is the ability to systematically vary constitutive model parameters across a specified domain and generate corresponding finite element simulations. This is achieved through the parametric study capabilities of Abaqus/CAE, which allow input files to be dynamically populated with symbolic parameters and batch-executed over a defined grid. The flexibility of this approach ensures coverage of the relevant parameter space for training data generation, while maintaining compatibility with user-defined material models (UMATs).

4.3.1 Parametric Input via *Parameter Block

Abaqus supports the inclusion of symbolic parameters in input files through the *Parameter keyword. Each symbolic name is assigned a default value, which can later be overridden by the parameter study engine. These parameters are referenced in the UMAT input line and interpreted at runtime.

An example of such parametrization is shown below:

```
*Parameter
y_0 = 450.0
Q   = 150.0
b   = 18.0
*Material, Name=Metal
*User Material, Constants=8
200.e3, 0.3, 200.0, <y_0>, <Q>, <b>, 1.0, 1e3
```

Here, the yield stress (y_0), saturation strength (Q), and hardening rate (b) are defined as symbolic variables and injected into the user material definition. This structure allows full compatibility with the Abaqus parameter study module, while also ensuring that the UMAT remains general across simulation instances.

4.3.2 Parameter Study with ParStudy API

The input files with symbolic parameters are processed using the ParStudy module available in Abaqus/CAE's scripting interface. This module provides a programmatic interface for defining parameter types, sampling methods, and design execution. In this work, the parameter study is managed through the custom script INPUTnODBGenerator.psf, which wraps the full setup process with user prompts for domain specification and combination logic. Table 4.1 summarizes the core commands used by the Abaqus ParStudy object.

Table 4.1: Key commands in user-developed parameter study script for Abaqus

Command	**Function**
ps = ParStudy()	Create a parameter study object
ps.define()	Define parameters, ranges, and reference values
ps.sample()	Choose sampling method and number of intervals
ps.combine()	Generate combinations (cross, mesh, tuple)
ps.generate()	Build input files and study designs
ps.execute()	Submit jobs for all design points

The typical parameter study workflow includes the following sequence:

1. Define parameter names, types, and numerical domains
2. Choose a sampling strategy: cross, mesh, or tuple
3. Combine sampled parameters into simulation designs
4. Generate input files for each design point
5. Execute all jobs to produce output databases

4.3.3 Sampling Strategies

The three built-in sampling strategies supported by Abaqus provide different mechanisms to populate the design space:

- **Cross:** Varies one parameter at a time around a reference point (1D perturbation). Useful for sensitivity studies.
- **Mesh:** Constructs a Cartesian grid with every possible combination of all sampled values (full factorial design).
- **Tuple:** Allows manual pairing of parameter sets without combinatorial expansion. Useful for custom designs.

In this study, the **Mesh** method is used to generate a full 3D grid of parameter combinations over the ranges of y_0, Q, and b. This ensures that all possible interactions between the parameters are captured during training and enables the network to generalize across the domain.

The script ensures that each combination is uniquely indexed and produces a corresponding input file and output database, which are later used in dataset generation. Parameters embedded in the input file are labeled with # from study, allowing automated parsing in the optimization stage.

4.4 Data Extraction from ODBs

Once the parameter study simulations are completed, each design point produces an output database (ODB file) containing the computed field outputs such as stress, strain, displacement, and other history-dependent variables. To train an artificial neural network for inverse regression, these simulation results must be extracted in a consistent and structured format across all design points. This is accomplished using a custom Python script, DataSetCreator.py, which leverages Abaqus's postprocessing API.

4.4.1 Output Database Structure

Each ODB file stores results incrementally across analysis steps and frames. Field outputs (e.g., S for stress, E for strain) are available at nodes or integration points. In this framework, data are read from element-nodal outputs, meaning that integration point results are interpolated to nodes before being extracted. [130]

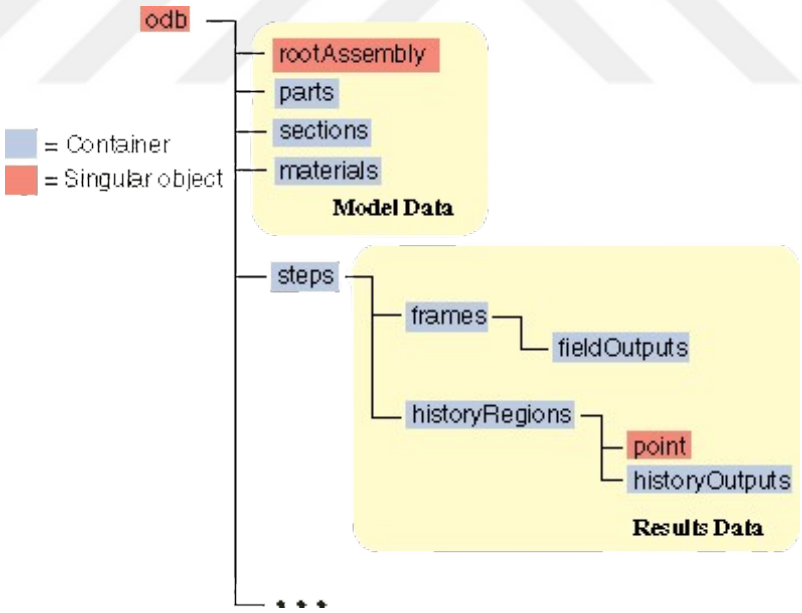

Figure 4.2: Structure of the Abaqus output database and access flow [130].

As illustrated in Figure 4.2, the script opens each ODB, navigates to the specified step and frame range, and extracts the stress and strain tensors from a target node or element centroid. This information is flattened into a one-dimensional array representing the full curve. All such arrays are compiled into a CSV file [130].

4.4.2 Format of Stress-Strain Dataset

The output of DataSetCreator.py is a file named stress-strain.csv. Each row corresponds to a unique parameter set and contains the time-history of the stress and strain values extracted from a single element. For consistency, all simulations must be run with the same number of intervals so that every row has the same length.

Table 4.2: Structure of stress-strain.csv with 4 intervals per simulation.

File Name	σ_1	σ_2	σ_3	σ_4	ε_1	ε_2	ε_3	ε_4
validation.odb	...	...	...	...	...	...	...	...
ParStudy_c1.odb	...	...	...	...	...	...	...	...
ParStudy_c2.odb	...	...	...	...	...	...	...	...
ParStudy_c3.odb	...	...	...	...	...	...	...	...
experiment	...	...	...	...	...	...	...	...

As shown in Table 4.2, each row contains stress values followed by strain values, concatenated to form a single input array for training. Validation data is automatically written in the first row of the file. However, the experimental data must be appended manually to the final row of the file under the name experiment.

4.4.3 Robustness and Error Handling

The script is designed to handle failed or incomplete simulations. If an ODB file lacks an assembly or expected output field, it is flagged and skipped. Similarly, ODBs with constant values, typically resulting from numerical divergence or rigid behavior, are excluded from the training data. This filtering is based on the detection of zero or near-zero variation in stress and strain arrays.

For correct parsing, the number of output intervals (i.e., analysis frames) must match the number used during training data generation. This is controlled by the keyword ”number interval=” in the original input file and must be consistent across all designs. The resulting stress-strain.csv file is saved to the working directory and serves as the sole input to the final stage of the optimization pipeline.

4.5 ANN-Based Regression for Parameter Prediction

Following the construction of the stress-strain dataset, the final stage of the optimization pipeline uses ANNs to regress the underlying material parameters from the full curve response. Unlike conventional symbolic regression or curve-fitting techniques, which attempt to extract a closed-form model or fit individual descriptors (e.g., yield strength, hardening slope), this approach utilizes the entire stress-strain trajectory to infer the governing parameters of the constitutive model.

4.5.1 Motivation for Curve-Based Regression

Material response in finite element simulations is shaped not only by constitutive laws but also by numerical and geometric factors, such as strain rate, boundary conditions, element distortion, and loading history. Consequently, traditional identification techniques based on single-point values or curve features are often insufficient for uniquely identifying material parameters, particularly when multiple parameters interact nonlinearly, as in hardening laws or damage models.

By contrast, curve-level regression offers several advantages:

- The network learns from the full evolution of stress and strain, capturing non-obvious interactions between parameters.
- It becomes possible to recover parameter sets even when they have similar macroscopic characteristics but differ in underlying formulation.
- Once trained, the model provides near-instant predictions without additional simulations, significantly reducing computational cost for inverse identification.

4.5.2 Input and Output Format

The ANN is implemented as a fully connected feedforward network. Each input is a 1D array formed by concatenating the stress and strain values at all time increments.

For a simulation with n frames, the input vector has a size of $2n$.

$$\text{Input vector:} \quad [\sigma_1, \sigma_2, ..., \sigma_n, \varepsilon_1, \varepsilon_2, ..., \varepsilon_n]$$

Each output is a vector containing the material parameters used in the corresponding simulation. In the current study, the ANN is trained to predict the three parameters of the Voce-type hardening law:

$$\boldsymbol{y} = [y_0, Q, b]$$

The input and output data are automatically aligned based on file names and parameter tags parsed from the input decks during dataset construction.

4.5.3 Training and Validation Logic

The training is performed using standard mean squared error (MSE) loss between predicted and actual parameter values. The data are split into training and validation subsets. Any ODB files prefixed with validation are held out during training and evaluated separately to monitor generalization performance.

The experimental input, manually added as the last row of the dataset with the name experiment, is not used during training or validation. Instead, it is used only for final prediction and comparison.

Early stopping and learning rate schedules are not applied at this stage, as the focus is on validating the architecture and assessing baseline performance. All inputs are normalized before training, and output predictions are rescaled to match the original parameter ranges before reporting.

4.5.4 Comparison to Alternative Strategies

Unlike symbolic regression, which seeks an analytical model structure, this method treats the UMAT and finite element model as a black-box simulator and focuses solely on inverse mapping. Additionally, surrogate modeling approaches typically emulate the forward response, while this approach inverts the mapping directly.

This makes the method highly compatible with complex material models where analytic gradients are unavailable or response surfaces are non-convex and ill-behaved. It is also adaptable to models with additional features such as rate-dependence, damage accumulation, or anisotropy, making it a scalable foundation for future extensions.

4.6 Case Study: J2 Plasticity with Voce Hardening

To validate the proposed ANN-based parameter prediction framework, this study applies it to a simplified, yet representative, material model: rate-independent J2 plasticity with isotropic Voce hardening under finite strain kinematics. The model is implemented via a UMAT in Abaqus and serves as a foundational testbed prior to introducing more complex inelastic mechanisms in later stages. This section presents the theoretical formulation of the finite strain plasticity model, the yield surface definition, and the numerical implementation details.

4.6.1 Finite Strain Kinematics

Consider a homogeneous body $\mathcal{B}$ initially in a reference configuration. The deformation of a point $\boldsymbol{X} \in \mathcal{B}$ is described by the motion function:

$$\boldsymbol{x} = \chi(\boldsymbol{X}, t) \tag{4.1}$$

From this mapping, we define the deformation gradient $\mathbf{F}$, velocity $\mathbf{v}$, and velocity gradient $\mathbf{L}$ as:

$$\mathbf{F} = \nabla\chi, \qquad \mathbf{v} = \dot{\chi}, \qquad \mathbf{L} = \nabla\mathbf{v} = \dot{\mathbf{F}}\mathbf{F}^{-1} \tag{4.2}$$

Under finite deformation plasticity, we adopt the Kröner–Lee multiplicative decomposition of $\mathbf{F}$:

$$\mathbf{F} = \mathbf{F}^e\mathbf{F}^p \tag{4.3}$$

where $\mathbf{F}^e$ and $\mathbf{F}^p$ are the elastic and plastic deformation gradients, respectively. The total velocity gradient $\mathbf{L}$ then becomes:

$$\mathbf{L} = \mathbf{L}^e + \mathbf{F}^e\mathbf{L}^p\mathbf{F}^{e-1} \tag{4.4}$$

with the elastic and plastic parts expressed as:

$$\mathbf{L}^e = \dot{\mathbf{F}}^e \mathbf{F}^{e-1}, \qquad \mathbf{L}^p = \dot{\mathbf{F}}^p \mathbf{F}^{p-1} \tag{4.5}$$

Decomposing these tensors into their symmetric (stretching) and skew-symmetric (spin) components yields:

$$\begin{aligned} \mathbf{D}^e &= \mathrm{sym}(\mathbf{L}^e), \qquad \mathbf{W}^e = \mathrm{skw}(\mathbf{L}^e) \\ \mathbf{D}^p &= \mathrm{sym}(\mathbf{L}^p), \qquad \mathbf{W}^p = \mathrm{skw}(\mathbf{L}^p) \end{aligned} \tag{4.6}$$

The determinant of the deformation gradient defines the local volume change:

$$J = \det(\mathbf{F}) \tag{4.7}$$

By applying the decomposition in (4.3), the Jacobian can be written as:

$$J = J^e J^p, \qquad J^e = \det(\mathbf{F}^e) > 0, \qquad J^p = \det(\mathbf{F}^p) > 0 \tag{4.8}$$

Assuming the plastic flow is incompressible and irrotational, we impose:

$$\det(\mathbf{F}^p) = 1, \qquad \mathrm{tr}(\mathbf{D}^p) = 0, \qquad \mathbf{W}^p = \mathbf{0} \tag{4.9}$$

The elastic deformation gradient is decomposed into stretch and rotation via right polar decomposition:

$$\mathbf{F}^e = \mathbf{R}^e \mathbf{U}^e \tag{4.10}$$

where $\mathbf{R}^e$ is the rotation tensor and $\mathbf{U}^e$ is the right stretch tensor. The right Cauchy–Green tensor and Hencky (logarithmic) strain follow as:

$$\mathbf{C}^e = \mathbf{F}^{eT} \mathbf{F}^e = (\mathbf{U}^e)^2, \qquad \mathbf{E}^e = \ln(\mathbf{U}^e) \tag{4.11}$$

Using the incompressibility constraint (4.9), we simplify the plastic velocity gradient and evolution of $\mathbf{F}^p$ as:

$$\mathbf{L}^p = \mathbf{D}^p, \qquad \dot{\mathbf{F}}^p = \mathbf{D}^p \mathbf{F}^p \tag{4.12}$$

The equivalent plastic strain rate and equivalent von Mises stress are defined by:

$$\dot{\bar{\varepsilon}}^p = \sqrt{\frac{2}{3}} \left| \mathbf{D}^p \right|, \qquad \bar{\sigma} = \sqrt{\frac{3}{2}} \left| \mathbf{M}_0^e \right| \tag{4.13}$$

where $\mathbf{M}_0^e$ is the deviatoric part of the elastic Mandel stress. Associated plastic flow assumes codirectionality:

$$\mathbf{N}^p = \frac{\mathbf{D}^p}{|\mathbf{D}^p|} = \frac{\mathbf{M}_0^e}{|\mathbf{M}_0^e|} \tag{4.14}$$

Hence, the plastic stretching tensor can be expressed as:

$$\mathbf{D}^p = \sqrt{\frac{3}{2}}\,\dot{\bar{\varepsilon}}^p\,\mathbf{N}^p \tag{4.15}$$

4.6.2 Yield Surface and Voce-Type Isotropic Hardening

The yield condition is governed by a von Mises-type function:

$$\Phi = \sqrt{\frac{3}{2}}|\mathbf{M}_0^e| - \sigma_y \tag{4.16}$$

Plastic loading occurs when $\Phi = 0$, and during flow, the consistency condition $\dot{\Phi} = 0$ must hold. The evolution of the yield stress is governed by the Voce law:

$$\sigma_y = y_0 + Q\,(1 - \exp(-b\,\bar{\varepsilon}^p)) \tag{4.17}$$

where y_0 is the initial yield stress, Q the saturation strength, and b the hardening rate. These three parameters are the targets of the regression pipeline.

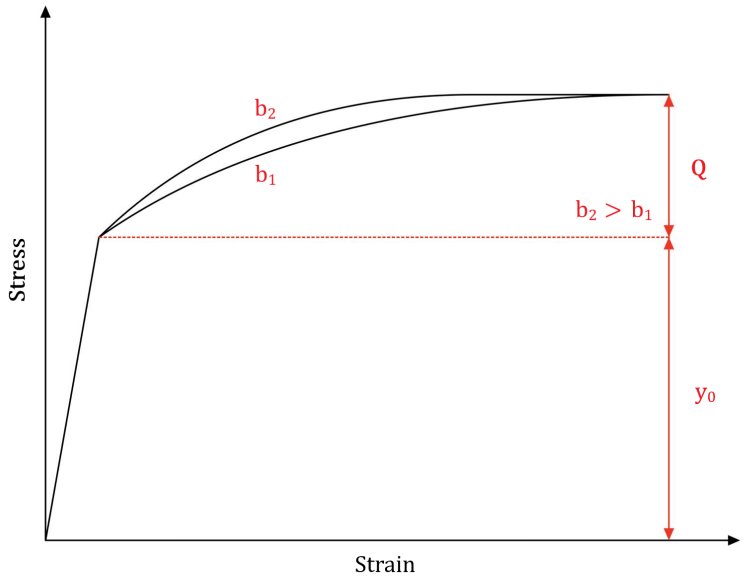

Figure 4.3: Parameters of Voce type isotropic hardening

4.6.3 Numerical Implementation via UMAT

The model is implemented using a custom Abaqus UMAT, operating under an exponential return-mapping framework in logarithmic strain space. At each integration point, the algorithm proceeds as follows:

1. Evaluate trial stress assuming elastic predictor.
2. Check yield condition; if violated, invoke plastic correction.
3. Apply return mapping and update internal variables.
4. Recalculate stress and tangent operator for global convergence.

The internal variable $\overline{\varepsilon}^p$ is stored and evolved incrementally, and the consistent tangent is used for plastic steps.

4.6.4 Domain Sampling for Training Data Generation

The parameter space is discretized over:

- $y_0 \in [400, 500]$ MPa
- $Q \in [100, 200]$ MPa
- $b \in [10, 30]$

Using the ‘mesh‘ strategy from the ParStudy tool, all possible combinations of these values are constructed. Each simulation yields a stress-strain curve under prescribed uniaxial loading, forming the input data for ANN training. As described in Section 4.4, stress and strain vectors are extracted and formatted for supervised learning.

Despite its relative simplicity, the model is sufficient to demonstrate the capability of the ANN to distinguish between nonlinear effects of hardening parameters solely from curve shapes. The test case also establishes a workflow for expanding toward complex crystal plasticity or viscoplastic UMATs.

4.7 ANN Training, Results, and Future Outlook

Having generated a comprehensive dataset from the finite strain J2 plasticity simulations, the next step involves training a feed-forward artificial neural network (ANN) to predict material parameters y_0, Q, and b from the corresponding stress-strain responses. This section presents the architecture, training procedure, evaluation metrics, and regression results of the ANN model applied to this inverse prediction task. It concludes with a forward-looking discussion on extending this framework toward more challenging material systems.

4.7.1 Neural Network Architecture and Input Representation

The regression problem is approached using a fully connected ANN implemented in TensorFlow. The network takes as input a stress-strain curve sampled at fixed intervals and outputs a vector of three predicted material parameters.

The input vector is formed by flattening the stress and strain arrays extracted from simulation outputs. For each curve, both engineering strain ε and engineering stress σ values are interpolated to a fixed length (e.g., 250 points), normalized, and concatenated to form a $2n$-dimensional input vector.

Input shape: 500 (250 strain + 250 stress points)
Output shape: 3 (corresponding to y_0, Q, and b)

The chosen ANN architecture consists of:

- 5 hidden layers
- 200 neurons per layer
- ReLU activation functions throughout
- No batch normalization or dropout (due to the limited dataset)

The network is trained using the Adam optimizer with a learning rate of 0.001, minimizing the mean squared error (MSE) between the true and predicted parameter values.

4.7.2 Training Protocol and Data Splitting

The total dataset consists of 88 simulations generated from the mesh-sampled design space. These are divided into:

- 75 samples for training (85%)
- 13 samples for validation and testing (15%)

Mini-batch training is applied with a batch size of 8. The model is trained for 300 epochs with early stopping enabled to mitigate overfitting. Parameters are scaled to the [0, 1] range prior to training and inverse-transformed post-prediction for interpretation.

4.7.3 Performance Metrics and Loss Behavior

Model performance is evaluated using three standard regression metrics: root mean squared error (RMSE), mean absolute error (MAE), and coefficient of determination (R^2). These metrics provide complementary insights into the ANN's ability to recover the material parameters from input stress-strain curves. RMSE penalizes larger errors more heavily and is sensitive to outliers, while MAE gives a direct average magnitude of errors across predictions. The R^2 score indicates how well the predicted values correlate with the true values, with a perfect model yielding $R^2 = 1$.

Table 4.3: Validation and test metrics for ANN regression model

Metric	**RMSE**	**MAE**	R^2
Validation Set	5.38	3.24	0.986
Test Set	6.01	3.89	0.978

The loss function used during training is the mean squared error (MSE), calculated between the predicted and ground-truth values of the three material parameters y_0, Q, and b. Since these parameters have different physical scales and units (e.g., yield strength in MPa, dimensionless hardening rate), the outputs were normalized before training and later inverse-transformed for evaluation.

During training, the convergence behavior of the MSE loss was smooth and monotonic, with validation loss tracking closely alongside training loss. This suggests that the network generalizes well and does not suffer from overfitting, despite the relatively small size of the dataset. The consistently high R^2 values on both validation and test sets further confirm that the network has captured the underlying functional mapping from stress-strain response to material parameters.

This behavior is similar to what was observed in earlier models trained to predict rupture time and fatigue lifetime: once the output parameter space is normalized and well-covered in training data, MSE-based optimization proves stable and interpretable. Moreover, for inverse problems such as parameter recovery—where small differences in parameters can lead to large deviations in output behavior—the choice of MSE loss ensures that large parameter errors are more strongly penalized, reinforcing precision in sensitive regions of the parameter space.

4.7.4 Curve Reconstruction and Validation

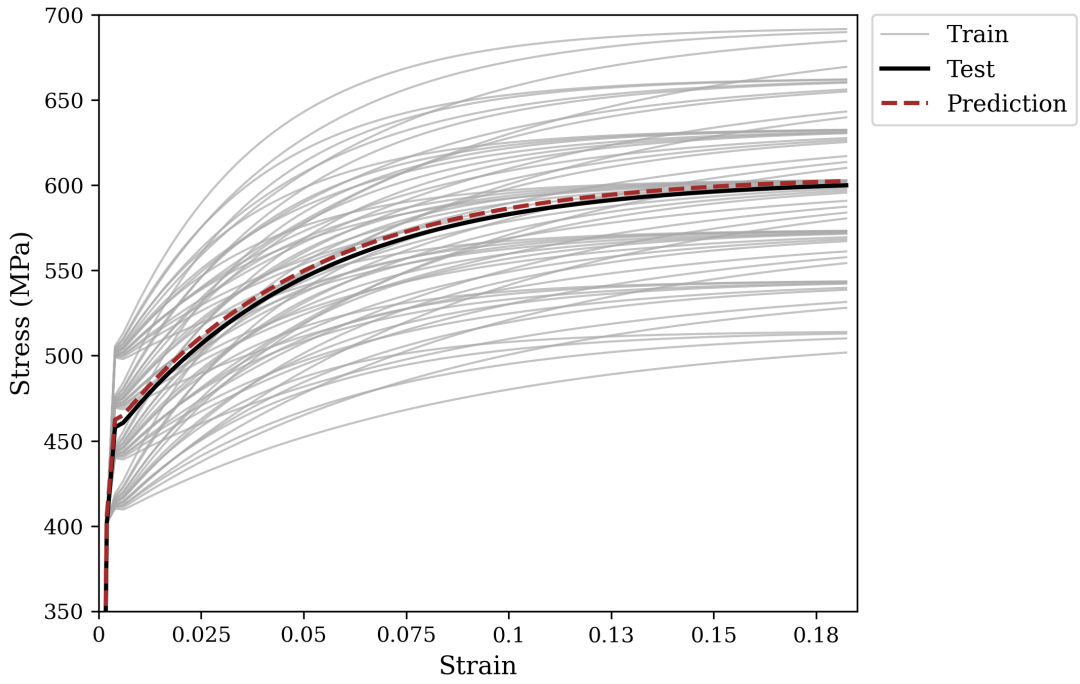

Figure 4.4: Comparison of true and ANN-reconstructed stress-strain curves using predicted parameters.

To verify the effectiveness of the predicted parameters, the output values from the ANN are reinserted into the UMAT to regenerate stress–strain curves. These regenerated curves are then directly compared to the original ones from the simulation dataset to assess the consistency and physical validity of the predictions. A close match between the two indicates that the ANN has accurately captured the underlying material behavior. Figure 4.4 illustrates one such example, where the predicted and original curves exhibit near-identical behavior across the entire deformation range.

4.7.5 Discussion and Future Work

The results of this case study demonstrate that even with a relatively limited dataset and simplified hardening behavior, a neural network can effectively learn the inverse relationship between full stress-strain profiles and their generating parameters. The Voce law introduces enough nonlinearity to challenge the model, yet the regression errors remain within acceptable bounds. This success validates the overall pipeline and highlights the advantages of full-field curve matching over scalar-objective methods. However, the current study also sets the stage for future developments.

1. Application to More Complex Materials:
The next phase of this research will investigate more complex constitutive models, including rate-dependent plasticity, nonlinear viscoplasticity, and softening behaviors. These materials include polymeric composites or elastoplastic systems where the stress-strain response is not strictly monotonic. In such cases, softening leads to repeated stress values for different strain levels (i.e., curve non-injectivity after UTS), posing a challenge for standard feed-forward networks.

2. Sequence Learning via Recurrent Networks:
To handle the temporal nature of softening and post-necking behavior, future models may employ Long Short-Term Memory (LSTM) networks. These architectures are well-suited for time-series or sequential data and can better capture input redundancy or history-dependent evolution, making them promising for stress-strain regression where hysteresis or reloading is involved.

3. Integration with Experimental Noise:

A further challenge will be the incorporation of noisy experimental data. Robustness to measurement error and physical variability is essential for real-world applicability. This will require regularization strategies, data augmentation, and potentially probabilistic regression techniques to quantify uncertainty.

CHAPTER 5

CONCLUSIONS AND FUTURE WORK

5.1 Summary of Contributions

This thesis proposed a hybrid framework combining synthetic data generation via physics-based continuum damage mechanics (CDM) models with data-driven prediction through artificial neural networks (ANNs). The contributions are as follows:

- Modified the Chaboche model to incorporate crystallographic anisotropy specific to FCC single crystals. This model was validated both quantitatively by predicting fatigue lifetimes on experimental datasets and qualitatively by identifying crack initiation sites in notched specimens for different crystallographic orientations.
- Developed a comprehensive synthetic dataset for the CMSX-4 nickel-based single crystal superalloy using a Chaboche-type CDM model across various R-ratios and temperatures.
- Trained ANN architectures capable of learning fatigue lifetime behavior from synthetic data, validated through SN-curves and Goodman diagrams.
- Implemented a transfer learning scheme that adapts pretrained ANN models to sparse experimental datasets using layer freezing and Leave-One-Out Cross-Validation (LOOCV), enhancing generalization.
- Extended the base ANN to incorporate additional features such as temperature, dwell time, and HCF-to-LCF cycle ratio for more realistic fatigue behavior modeling.

- Proposed a second pipeline that performs inverse parameter identification by regressing material model parameters from full-field stress-strain curves using deep ANNs trained on Abaqus-generated simulation data.

5.2 Limitations

Despite the success of the proposed methodologies, certain limitations remain:

- The base model and transfer learning approaches rely on the availability of reasonably representative synthetic datasets, which may be limited by the fidelity of the underlying CDM or UMAT models.
- Experimental validation is constrained by the scarcity of high-quality fatigue data, especially for advanced alloys like CMSX-4 due to proprietary restrictions.
- Input features in the fatigue models (e.g., stress, R-ratio, temperature) are scalar representations; geometric, microstructural, or multiaxial effects are not directly incorporated.
- The inverse parameter identification method assumes monotonicity and injectivity in stress-strain behavior, limiting its applicability to materials with strong softening or path-dependent responses.

5.3 Future Directions

Several avenues exist to extend the present work:

- **Transfer Learning:** Further datasets will be generated to explore the influence of creep-fatigue interaction, enabling the modeling of TMF conditions. This effort aims to improve the robustness and relevance of the transfer learning models in real service environments.
- **Input Expansion Generalization:** Future work will also focus on improving the generalization capability of the input expansion strategy in the transfer

learning models. As additional physical effects are considered, the input space becomes more complex, and reducing this data complexity will be essential for ensuring scalable and efficient learning.

- **Robust Learning with Experimental Noise:** Introduce regularization strategies, data augmentation, and probabilistic regression (e.g., Bayesian ANNs) to enhance robustness to experimental uncertainty.
- **Hybrid Physical-Learning Integration:** Extend the hybrid framework by embedding physical constraints or equations directly into the loss functions or model structure (physics-informed neural networks).
- **Online Learning and Adaptivity:** Explore continual learning frameworks to update the ANN models dynamically with new experimental data during component operation or testing.
- **Advanced Constitutive Modeling:** (For parameter optimization models) Incorporate rate-dependent plasticity, cyclic softening, or viscoplasticity to generate richer training data, enabling models to capture more complex behaviors observed in service conditions.
- **Sequence Learning Models:** (For parameter optimization models) Integrate recurrent architectures such as LSTM or Transformer models to account for non-monotonic stress-strain profiles and memory effects in fatigue and deformation.

The methods developed here serve as a foundational toolset for fatigue lifetime modeling and parameter identification in high-value aerospace alloys. Future research will build on this framework to handle real-world complexity and further bridge the gap between simulations, data, and experimental practice.

REFERENCES

[1] J.G. Leishman, "Turbojet engines," in *Introduction to Aerospace Flight Vehicles*. Embry-Riddle Aeronautical University, 2022.

[2] Rolls-Royce plc, *The Jet Engine*, 5th ed. Derby, England: Rolls-Royce plc, 1996, originally published in 1986.

[3] K. Wei, "Turbofan and turbojet engines: Working process and future development," in *Proceedings of the 2023 International Conference on Mathematical Physics and Computational Simulation*. Blacksburg, Virginia, USA: Theoretical and Natural Science, 2023, pp. 114–119.

[4] J.G. Leishman, "Turbofan & turboprop engines," in *Introduction to Aerospace Flight Vehicles*. Embry-Riddle Aeronautical University, 2022.

[5] A. Linke-Diesinger, *Introduction*. Berlin, Germany: Springer-Verlag Berlin Heidelberg, 2008, ch. 1, pp. 6–7.

[6] W. Maktouf and K. Sai, "An investigation of premature fatigue failures of gas turbine blade," *Engineering Failure Analysis*, vol. 47, pp. 89–101, 2015.

[7] T.J. Carter, "Common failures in gas turbine blades," *Engineering Failure Analysis*, vol. 12, no. 2, pp. 237–247, 2005.

[8] T.S. Chowdhury, F.T. Mohsin, M.M. Tonni, M.N.H. Mita, and M.M. Ehsan, "A critical review on gas turbine cooling performance and failure analysis of turbine blades," *International Journal of Thermofluids*, vol. 18, p. 100329, 2023.

[9] J. Riccius and E. Zametaev, "HCF and LCF analysis of a generic full admission turbine blade," *Aerospace*, vol. 10, p. 154, 2023.

[10] J. Hou, B. Wicks, and R. Antoniou, "An investigation of fatigue failures of turbine blades in a gas turbine engine by mechanical analysis," *Engineering Failure Analysis*, vol. 9, pp. 201–211, 2002.

[11] D. Sun and Z. Wan, “Experimental study and life prediction for aero-engine turbine blade considering creep-fatigue interaction effect,” *Engineering Fracture Mechanics*, vol. 310, p. 110507, 2024.

[12] N. Arakere and G. Swanson, “Effect of crystal orientation on fatigue failure of single crystal nickel base turbine blade superalloys,” *Journal of Engineering for Gas Turbines and Power*, vol. 124, pp. 161–176, 2002.

[13] H. Hong, J. Kang, B. Choi, I. Kim, Y. Yoo, and C. Jo, “A comparative study on thermomechanical and low cycle fatigue failures of a single crystal nickel-based superalloy,” *International Journal of Fatigue*, vol. 33, pp. 1592–1599, 2011.

[14] M. Okazaki and M. Sakaguchi, “Thermo-mechanical fatigue failure of a single crystal Ni-based superalloy,” *International Journal of Fatigue*, vol. 30, pp. 318–323, 2008.

[15] S. Khushbash, A. Hameed, A. Mumtaz, H. Ali Khan, and A. Shahzad, “Investigation of temperature assisted corrosion failure of an aircraft turbine blade,” *Engineering Failure Analysis*, vol. 167, p. 108909, 2025.

[16] Z. Shi, X. Wang, S. Liu, and J. Li, “Low cycle fatigue properties and microstructure evolution at 760 °C of a single crystal superalloy,” *Progress in Natural Science: Materials International*, vol. 25, pp. 78–83, 2015.

[17] R. Wang, B. Zhang, D. Hu, K. Jiang, X. Hao, J. Mao, and F. Jing, “In-phase thermomechanical fatigue lifetime prediction of nickel-based single crystal superalloys from smooth specimens to notched specimens based on coupling damage on critical plane,” *International Journal of Fatigue*, vol. 126, pp. 327–334, 2019.

[18] S. Kalluri and M. McGaw, “Effect of tensile mean stress on fatigue behavior of single-crystal and directionally solidified superalloys,” in *Proceedings of the Symposium on Cyclic Deformation, Fracture, and Nondestructive Evaluation of Advanced Materials*, San Antonio, TX, USA, Nov. 1990.

[19] T.M. Pollock and S. Tin, “Nickel-based superalloys for advanced turbine engines: Chemistry, microstructure, and properties,” *Journal of Propulsion and Power*, vol. 22, no. 2, pp. 361–374, March–April 2006.

[20] R. Reed, "The superalloys fundamentals and applications," *The Superalloys: Fundamentals and Applications*, pp. 1–372, 2006.

[21] R.W. Neu, "Crack paths in single-crystal Ni-base superalloys under isothermal and thermomechanical fatigue," *International Journal of Fatigue*, vol. 123, pp. 268–278, 2019.

[22] E.A.E. Rodas, S. Gorgannejad, and R.W. Neu, "Creep-fatigue behaviour of single-crystal Ni-base superalloy CMSX-8," *Fatigue & Fracture of Engineering Materials & Structures*, vol. 42, no. 9, pp. 2155–2171, 2019.

[23] K.P.L. Fullagar, R.W. Broomfield, M. Hulands, K. Harris, G.L. Erickson, and S.L. Sikkenga, "Aero engine test experience with CMSX-4® alloy single-crystal turbine blades," *Journal of Engineering for Gas Turbines and Power*, vol. 118, no. 2, pp. 380–388, 1996.

[24] G.R. Swanson and N.K. Arakere, "Effect of crystal orientation on analysis of single-crystal, nickel-based turbine blade superalloys," NASA, Marshall Space Flight Center, Marshall Space Flight Center, Alabama, Tech. Rep. NASA/TP–2000-210074, February 2000.

[25] B. Kościelniak, K. Gancarczyk, M. Poreba, and R. Albrecht, "Influence of crystallographic orientation on creep resistance of single-crystal superalloy," *Advances in Manufacturing Science and Technology*, vol. 44, 2020.

[26] Y. Huang, D. Wang, J. Shen, Y. Lu, L. Lou, and J. Zhang, "Initiation of Fatigue Cracks in a Single-Crystal Nickel-Based Superalloy at Intermediate Temperature," in *Superalloys 2020*, S. Tin *et al.*, Eds., The Minerals, Metals & Materials Series. Springer, Cham, 2020, pp. 208–217.

[27] J. Chen and Y. Liu, "Fatigue modeling using neural networks: A comprehensive review," *Fatigue & Fracture of Engineering Materials & Structures*, vol. 45, pp. 945–979, 2022.

[28] E. Santecchia, P. Spinelli, E. Cabibbo, F. Curioni, J. Regev, G. Musharova, D. Carrol, and A. Fortunato, "A review on fatigue life prediction methods for metals," *Advances in Materials Science and Engineering*, 2016.

[29] J. D. Morrow, “Cyclic Plastic Strain Energy and Fatigue of Metals,” in *ASTM STP 378*, pp. 45–87, 1965.

[30] P. Shi and J. Sun, “A New Frequency-Dependent Energy-Based Fatigue Life Prediction Model for Metals under Multiaxial Loadings,” *International Journal of Fatigue*, vol. 119, pp. 30–40, 2019.

[31] Y. Lee, M. Barkey, and H. Kang, “Energy-Based Multiaxial Fatigue Life Prediction with Damage Parameters on Critical Planes,” *International Journal of Fatigue*, vol. 59, pp. 237–245, 2014.

[32] E. Castillo and A. Fernández-Canteli, *A Unified Statistical Methodology for Modeling Fatigue Damage*, Springer, 2009.

[33] ASTM Committee E-9, “Manual on Statistical Planning and Analysis for Fatigue Experiments, ASTM STP 588,” 1963.

[34] M. Brown and K. Miller, “A theory for fatigue failure under multiaxial stress-strain conditions,” *Proceedings of the Institution of Mechanical Engineers*, vol. 187, p. 745, 1973.

[35] A. Fatemi and D. F. Socie, “A Critical Plane Approach to Multiaxial Fatigue Damage Including Out-of-Phase Loading,” *Fatigue & Fracture of Engineering Materials & Structures*, vol. 11, no. 3, pp. 149–165, 1988.

[36] K. Dang Van, “Macro-micro Approach in High-Cycle Multiaxial Fatigue,” in *Advances in Multiaxial Fatigue, ASTM STP 1191*, pp. 120–130, 1983.

[37] S. S. Manson, *Strain-Range Partitioning—A Tool for Characterizing High-Temperature Low-Cycle Fatigue*, NASA Technical Memorandum X-71691, 1975.

[38] R. Neu and H. Sehitoglu, “Thermo-mechanical fatigue, oxidation and creep: Part 2—life prediction,” *Metallurgical Transactions A*, vol. 20, no. 9, pp. 1769–1783, 1989.

[39] C. Cai, P. Liaw, J. Goldberg, M. Mitchell, and D. Klarstrom, “Recent developments in the thermomechanical fatigue life prediction of superalloys,” *JOM*, vol. 51, no. 4, pp. 22–26, 1999.

[40] H. El Kadi, "Modeling the Mechanical Behavior of Fiber-Reinforced Polymeric Composite Materials Using Artificial Neural Networks—A Review," *Composite Structures*, vol. 73, no. 1, pp. 1–23, 2006.

[41] Y. Al-Assaf and H. El Kadi, "Fatigue Life Prediction of Unidirectional Glass Fiber/Epoxy Composite Laminate Using Neural Networks," *Composite Structures*, vol. 53, no. 1, pp. 65–71, 2001.

[42] Y. A. Yucesan and F. A. C. Viana, "A Physics-Informed Neural Network for Wind Turbine Main Bearing Fatigue Prognostics," *International Journal of Prognostics and Health Management*, vol. 11, no. 1, p. 17, 2020.

[43] L.M. Kachanov, "Time of the rupture process under creep conditions," *Izvestiia Akademii Nauk SSSR, Otdelenie Teckhnicheskikh Nauk*, no. 8, pp. 26–31, 1958, english transl. in Int. J. Fracture 97 (1999) 11–18.

[44] J. Lemaitre, "A continuous damage mechanics model for ductile fracture," *ASME Journal of Engineering Materials and Technology*, vol. 107, no. 1, pp. 83–89, 1985.

[45] D. Krajcinovic and G.U. Fonseka, "The continuous damage theory of brittle materials, part 1: General theory," *ASME Journal of Applied Mechanics*, vol. 48, no. 4, pp. 809–824, 1981.

[46] S. Murakami, "Mechanical modeling of material damage," *ASME Journal of Applied Mechanics*, vol. 55, no. 2, pp. 280–286, 1988.

[47] J.P. Cordebois and F. Sidoroff, "Damage-induced elastic anisotropy," in *Mechanical Behavior of Anisotropic Solids*, ser. Euromech 119, J.P. Boehler, Ed. Paris: Springer Netherlands, 1982, pp. 761–774.

[48] C. Chow and J. Wang, "An anisotropic theory of continuum damage mechanics for ductile fracture," *Engineering Fracture Mechanics*, vol. 27, no. 5, pp. 547–558, 1987.

[49] S. Chandrakanth and P.C. Pandey, "An isotropic damage model for ductile material," *Engineering Fracture Mechanics*, vol. 50, no. 4, pp. 457–465, 1995.

[50] J. Chaboche and P. Lesne, “A non-linear continuous fatigue damage model,” *Fatigue & Fracture of Engineering Materials & Structures*, vol. 11, pp. 1–17, 2007.

[51] Y. Liu and S. Mahadevan, “A unified multiaxial fatigue damage model for isotropic and anisotropic materials,” *International Journal of Fatigue*, vol. 29, pp. 347–359, 2007.

[52] Y.C. Xiao, S. Li, and Z. Gao, “A continuum damage mechanics model for high cycle fatigue,” *International Journal of Fatigue*, vol. 20, no. 7, pp. 503–508, 1998.

[53] A. De Jesus, A. Ribeiro, and A. Fernandes, “Finite element modeling of fatigue damage using a continuum damage mechanics approach,” *Journal of Pressure Vessel Technology-transactions of The Asme - J PRESSURE VESSEL TECHNOL*, vol. 127, 2005.

[54] B. Bhattacharya and B. Ellingwood, “A new CDM-based approach to structural deterioration,” *International Journal of Solids and Structures*, vol. 36, no. 12, pp. 1757–1779, 1999.

[55] J.F. Maire and J.L. Chaboche, “A new formulation of continuum damage mechanics for composite materials,” *Aerospace Science and Technology*, vol. 1, no. 4, pp. 247–257, 1997.

[56] H. W. Lee and C. Basaran, “A review of damage, void evolution, and fatigue life prediction models,” *Metals*, vol. 11, no. 4, 2021.

[57] D. Ramírez-Acevedo, R. R. Ambriz, C. J. García, C. Mendoza, and D. Jaramillo, “Strain measurement during quasi-static and cyclic loads in AL-6XN material using digital image correlation technique,” *Materials*, vol. 17, no. 15, 2024.

[58] W. Cui, “A state-of-the-art review on fatigue life prediction methods for metal structures,” *Journal of Marine Science and Technology*, vol. 7, no. 1, pp. 43–56, 2002.

[59] J. Lemaitre and J. Chaboche, *Mechanics of Solid Materials*. Cambridge, UK: Cambridge University Press, 1990.

[60] M. Matsuishi and T. Endo, “Fatigue of metals subjected to varying stress,” in *Proceedings of the Japan Society of Mechanical Engineers*. Japan Society of Mechanical Engineers, 1968.

[61] S. Downing and D. Socie, “Simple rainflow counting algorithms,” *International Journal of Fatigue*, vol. 4, no. 1, pp. 31–40, 1982.

[62] Y.L. Lee and T. Tjhung, “Chapter 3 – rainflow cycle counting techniques,” in *Metal Fatigue Analysis Handbook: Practical Problem-solving Techniques for Computer-aided Engineering*. Butterworth-Heinemann, 2012, pp. 89–114.

[63] C. McInnes and P. Meehan, “Equivalence of four-point and three-point rainflow cycle counting algorithms,” *International Journal of Fatigue*, vol. 30, no. 3, pp. 547–559, 2008.

[64] Y.W. Cheng and J.J. Broz, “Cycle-counting methods for fatigue analysis with random load histories: A FORTRAN user’s guide,” National Bureau of Standards, Boulder, Colorado, USA, Tech. Rep. NBSIR 86-3055, Aug. 1986.

[65] I. Rychlik, “Fatigue cycle counting,” in *Encyclopedia of Tribology*, Q.J. Wang and Y.W. Chung, Eds. Springer, 2013, pp. 1032–1041.

[66] E. Goodin, A. Kallmeyer, and P. Kurath, “Evaluation of nonlinear cumulative damage models for assessing HCF/LCF interactions in multiaxial loadings,” *Proceedings of the 9th National Turbine Engine High Cycle Fatigue Conference*, Pinehurst, NC, March 2004.

[67] A. Palmgren, “Die lebensdauer von kugellagern,” *Verfahrenstechnik*, vol. 68, pp. 339–341, 1924.

[68] J. Shigley and C. Mischke, *Mechanical Engineering Design*, 5th ed. New York, NY: McGraw-Hill, Inc., 1989.

[69] S. Manson, J. Freche, and C. Ensign, “Application of a double linear damage rule to cumulative fatigue,” in *ASTM Special Technical Publication 415*. ASTM International, 1967, pp. 384–412.

[70] S. Manson and G. Halford, "Practical implementation of the double linear damage rule and damage curve approach for treating cumulative fatigue damage," *International Journal of Fatigue*, vol. 17, pp. 169–192, 1981.

[71] F. Richart Jr. and N. Newmark, "An hypothesis for determination of cumulative damage in fatigue," *Proceedings of ASTM*, vol. 48, pp. 767–800, 1948.

[72] F. Bourbita and L. Rémy, "A combined critical distance and energy density model to predict high temperature fatigue life in notched single crystal superalloy members," *International Journal of Fatigue*, vol. 84, pp. 17–27, 2016.

[73] V. Levkovitch, R. Sievert, and B. Svendsen, "Simulation of deformation and lifetime behavior of a FCC single crystal superalloy at high temperature under low-cycle fatigue loading," *International Journal of Fatigue*, vol. 28, pp. 1791–1802, 2006.

[74] Y. Yu, S. Zhu, Q. Liu, and Y. Liu, "A new energy-critical plane damage parameter for multiaxial fatigue life prediction of turbine blades," *Materials*, vol. 10, no. 5, p. 513, 2017.

[75] G. Cailletaud, "Une approche micromécanique phénoménologique du comportement inélastique des métaux," Ph.D. Dissertation, Université Pierre et Marie Curie (Paris 6-Jussieu), Paris, France, 1987.

[76] G. Castelluccio and D. McDowell, "Mesoscale cyclic crystal plasticity with dislocation substructures," *International Journal of Plasticity*, vol. 98, pp. 1–26, 2017.

[77] J. Clayton, *Nonlinear Mechanics of Crystals*. Dordrecht, The Netherlands: Springer, 2011.

[78] L. Meric, P. Poubanne, and G. Cailletaud, "Single crystal modeling for structural calculations: Part 1 - model presentation," *Journal of Engineering Materials and Technology*, vol. 113, pp. 162–170, 1991.

[79] C. Kasar, U. Kaftancioglu, E. Bayraktar, and O. Aslan, "Lifetime prediction of single crystal nickel-based superalloys," *Applied Sciences*, vol. 15, no. 1, 2025.

[80] R. Donahue, H. Clark, P. Atanmo, R. Kumble, and A. McEvily, "Crack opening displacement and the rate of fatigue crack growth," *International Journal of Fracture Mechanics*, vol. 8, pp. 209–219, 1972.

[81] T. Hoshide and D. Socie, "Mechanics of mixed mode small fatigue crack growth," *Engineering Fracture Mechanics*, vol. 26, pp. 841–850, 1987.

[82] J. Lankford, D. Davidson, and K. Chan, "The influence of crack tip plasticity in the growth of small fatigue cracks," *Metallurgical and Materials Transactions A*, vol. 15, pp. 1579–1588, 1984.

[83] J. Qian and A. Fatemi, "Mixed mode fatigue crack growth: A literature survey," *Engineering Fracture Mechanics*, vol. 55, pp. 969–990, 1996.

[84] O. Aslan, "Numerical modeling of fatigue crack growth in single crystal nickel-based superalloys," Ph.D. Dissertation, Ecole Nationale Supérieure des Mines de Paris, Paris, France, 2010.

[85] M. Niazi, H. Wisselink, and T. Meinders, "Viscoplastic regularization of local damage models: Revisited," *Computational Mechanics*, vol. 51, pp. 203–216, 2012.

[86] D. Henann and L. Anand, "A large deformation theory for rate-dependent elastic-plastic materials with combined isotropic and kinematic hardening," *International Journal of Plasticity*, vol. 25, pp. 1833–1878, 2009.

[87] A. Sengupta, S. Putatunda, L. Bartosiewicz, J. Hangas, P. Nailos, M. Peputapeck, and E. Alberts, "Tensile behavior of a new single-crystal nickel-based superalloy (cmsx-4) at room and elevated temperatures," *Journal of Materials Engineering and Performance*, vol. 3, pp. 73–81, 1994.

[88] S. Forest, "Nickel base single crystals across length scales," in *Crystal Plasticity and Damage at Cracks and Notches in Nickel-Base Single-Crystal Superalloys*. Cham, Switzerland: Springer, 2022, pp. 457–473.

[89] D. Dye, J. Coakley, V. Vorontsov, H. Stone, and R. Rogge, "Elastic moduli and load partitioning in a single-crystal nickel superalloy," *Scripta Materialia*, vol. 61, pp. 109–112, 2009.

[90] W.S. McCulloch and W. Pitts, "A logical calculus of the ideas immanent in nervous activity," *Bulletin of Mathematical Biophysics*, vol. 5, no. 4, pp. 115–133, 1943.

[91] D.O. Hebb, *The Organization of Behavior: A Neuropsychological Theory*. New York: Wiley, 1949.

[92] F. Rosenblatt, "The perceptron: A probabilistic model for information storage and organization in the brain," *Psychological Review*, vol. 65, no. 6, pp. 386–408, 1958.

[93] M. Minsky and S. Papert, *Perceptrons: An Introduction to Computational Geometry*. Cambridge, MA: MIT Press, 1969.

[94] A.G. Ivakhnenko, "Polynomial theory of complex systems," *IEEE Transactions on Systems, Man, and Cybernetics*, vol. SMC-1, no. 4, pp. 364–378, 1971.

[95] J.J. Hopfield, "Neural networks and physical systems with emergent collective computational abilities," *Proceedings of the National Academy of Sciences (PNAS)*, vol. 79, no. 8, pp. 2554–2558, 1982.

[96] T. Kohonen, "Self-organized formation of topologically correct feature maps," *Biological Cybernetics*, vol. 43, no. 1, pp. 59–80, 1982.

[97] D.E. Rumelhart, G.E. Hinton, and R.J. Williams, "Learning representations by back-propagating errors," *Nature*, vol. 323, no. 6088, pp. 533–536, 1986.

[98] Y. LeCun, Y. Bengio, and G. Hinton, "Deep learning," *Nature*, vol. 521, no. 7553, pp. 436–444, 2015.

[99] Y.L. Han, "Artificial neural network technology as a method to evaluate the fatigue life of weldments with welding defects," *International Journal of Pressure Vessels and Piping*, vol. 63, no. 2, pp. 205–209, 1995.

[100] P. Artymiak, L. Bukowski, J. Feliks, S. Narberhaus, and H. Zenner, "Determination of S–N curves with the application of artificial neural networks," *Fatigue & Fracture of Engineering Materials & Structures*, vol. 22, no. 8, pp. 723–728, 1999.

[101] V. Venkatesh and H.J. Rack, "A neural network approach to elevated temperature creep–fatigue life prediction," *International Journal of Fatigue*, vol. 21, no. 3, pp. 225–234, 1999.

[102] H. El Kadi and Y. Al-Assaf, "Prediction of the fatigue life of unidirectional glass fiber/epoxy composite laminae using different neural network paradigms," *Composite Structures*, vol. 55, no. 2, pp. 239–246, 2002.

[103] A.P. Vassilopoulos, E.F. Georgopoulos, and V. Dionysopoulos, "Artificial neural networks in spectrum fatigue life prediction of composite materials," *International Journal of Fatigue*, vol. 29, pp. 20–29, 2007.

[104] H. El Kadi and Y. Al-Assaf, "Energy-based fatigue life prediction of fiberglass/epoxy composites using modular neural networks," *Composite Structures*, vol. 57, no. 1–4, pp. 85–89, 2002.

[105] K.L. Xiang, P.Y. Xiang, and Y.P. Wu, "Prediction of the fatigue life of natural rubber composites by artificial neural network approaches," *Materials & Design*, vol. 57, pp. 180–185, 2014.

[106] E. Maleki, O. Unal, and K.R. Kashyzadeh, "Fatigue behavior prediction and analysis of shot peened mild carbon steels," *International Journal of Fatigue*, vol. 116, pp. 48–67, 2018.

[107] X.C. Zhang, J.G. Gong, and F.Z. Xuan, "A deep learning based life prediction method for components under creep, fatigue and creep-fatigue conditions," *International Journal of Fatigue*, vol. 148, p. 106236, 2021.

[108] N.S. Gulgec, M. Takáč, and S.N. Pakzad, "Structural sensing with deep learning: Strain estimation from acceleration data for fatigue assessment," *Computer-Aided Civil and Infrastructure Engineering*, vol. 35, no. 12, pp. 1349–1364, 2020.

[109] H. Alqahtani, S. Bharadwaj, and A. Ray, "Classification of fatigue crack damage in polycrystalline alloy structures using convolutional neural networks," *Engineering Failure Analysis*, vol. 119, p. 104908, 2021.

[110] Z. Zhan and H. Li, "Machine learning based fatigue life prediction with effects of additive manufacturing process parameters for printed SS 316L," *International Journal of Fatigue*, vol. 142, p. 105941, 2021.

[111] C.B. Kalayci, S. Karagoz, and O. Karakas, "Soft computing methods for fatigue life estimation: a review of the current state and future trends," *Fatigue & Fracture of Engineering Materials & Structures*, vol. 43, no. 11, pp. 2763–2785, 2020.

[112] I. Goodfellow, Y. Bengio, and A. Courville, *Deep Learning*. Cambridge, MA, USA: MIT Press, 2016.

[113] C.M. Bishop, *Pattern Recognition and Machine Learning*. New York, NY, USA: Springer, 2006.

[114] K. Hornik, "Approximation capabilities of multilayer feedforward networks," *Neural Networks*, vol. 4, no. 2, pp. 251–257, 1991.

[115] C. Nwankpa, W. Ijomah, A. Gachagan, and S. Marshall, "Activation functions: Comparison of trends in practice and research for deep learning," *arXiv preprint arXiv:1811.03378*, 2018.

[116] P. Ramachandran, B. Zoph, and Q. V. Le, "Searching for activation functions," *arXiv preprint arXiv:1710.05941*, 2017.

[117] D. Yang, A. Jin, and Y. Li, "A novel physics-guided neural network for predicting fatigue life of materials," *Applied Sciences*, vol. 14, no. 6, 2024.

[118] M. Raissi, P. Perdikaris, and G. Karniadakis, "Physics-informed neural networks: A deep learning framework for solving forward and inverse problems involving nonlinear partial differential equations," *Journal of Computational Physics*, vol. 378, pp. 686–707, 2019.

[119] L. Bottou, "Stochastic gradient descent tricks," in *Neural Networks: Tricks of the Trade: Second Edition*, G. Montavon, G.B. Orr, and K.R. Müller, Eds. Berlin, Heidelberg: Springer Berlin Heidelberg, 2012, pp. 421–436.

[120] D. P. Kingma and J. Ba, "Adam: A method for stochastic optimization," *arXiv preprint arXiv:1412.6980*, 2017.

[121] I. Loshchilov and F. Hutter, "Decoupled weight decay regularization," *arXiv preprint arXiv:1711.05101*, 2019.

[122] N. Srivastava, G. Hinton, A. Krizhevsky, I. Sutskever, and R. Salakhutdinov, "Dropout: A simple way to prevent neural networks from overfitting," *Journal of Machine Learning Research*, vol. 15, no. 1, pp. 1929–1958, 2014.

[123] X. Glorot, A. Bordes, and Y. Bengio, "Deep sparse rectifier neural networks," in *Proceedings of the Fourteenth International Conference on Artificial Intelligence and Statistics (AISTATS)*, ser. Proceedings of Machine Learning Research, G. Gordon, D. Dunson, and M. Dudík, Eds., vol. 15. PMLR, 2011, pp. 315–323.

[124] C. M. Hamel, K. N. Long, and S. L. B. Kramer, "Calibrating constitutive models with full-field data via physics-informed neural networks," *Structural Control Health Monitoring*, 2022.

[125] M. Abbasi, "Inverse parameter identification of high-temperature constitutive models using response surface optimization," *Materials*, vol. 14, no. 9, 2021.

[126] T. Mareš, E. Janouchová, and A. Kučerová, "Artificial neural networks in the calibration of nonlinear mechanical models," *Advances in Engineering Software*, vol. 95, pp. 68–81, 2016.

[127] E. Markiewicz and B. Langrand, "Material parameter identification: Challenges and perspectives," in *Procedia Engineering*, vol. 173, 2017, pp. 33–40.

[128] N. Khutia and S. Dey, "Identification of constitutive model parameters using genetic algorithms: Application to cyclic plasticity," *International Journal of Computational Materials Science and Surface Engineering*, vol. 6, no. 1, pp. 50–74, 2014.

[129] P. Delobelle and V. Popov, "Multi-objective calibration of advanced material models: A case study on ratcheting and mean stress relaxation," *International Journal of Plasticity*, vol. 158, p. 103422, 2022.

[130] Dassault Systemes, *Abaqus 2018 Scripting User's Manual*. Dassault Systèmes Simulia Corp., Providence, RI, USA, 2018.

APPENDIX A

MODEL PARAMETERS

A.1 Crystal Plasticity & Modified Chaboche Model

The tables below demonstrate the parameters of material and lifetime prediction model used in Chapter 2.

Table A.1: Parameters of the crystal plasticity model for CMSX-4.

K (MPa$^{1/n}$)	**n**	**Q**	**b**	**C_{11} (GPa)**	**C_{12} (GPa)**	**C_{44} (GPa)**
2200	7.5	100	250	296	204	125

Table A.2: Parameters of the modified lifetime assessment model for CMSX-4.

σ_{uts} (MPa)	σ_{yield} (MPa)	$\mathbf{M_0}$ (MPa)	$\sigma_{l_0}^{\text{clv}}$ (MPa)	b_1 (MPa^{-1})	b_2 (MPa^{-1})	a	β
1200	1100	1800	0	1.12×10^{-4}	1.12×10^{-4}	0.65	7.8

A.2 Synthetic Data Generation (Single Crystal Superalloy Dataset)

Table A.3: Parameters of Chaboche Model used for data generation in Chapter 3.

T (°C)	σ_{uts} (MPa)	$\mathbf{M_0}$ (MPa)	σ_{l_0} (MPa)	b_1 (MPa^{-1})	b_2 (MPa^{-1})	a	β
25	890	1175	490	1.15×10^{-3}	1.12×10^{-3}	0.035	11.5
700	1050	1550	570	9.55×10^{-4}	9.50×10^{-4}	0.035	10.5
800	1150	1550	590	8.95×10^{-4}	8.80×10^{-4}	0.030	10.5
900	990	1400	550	1.05×10^{-3}	1.015×10^{-3}	0.057	11.5
1000	710	900	315	1.50×10^{-3}	1.43×10^{-3}	0.007	8.0
1100	450	800	110	2.20×10^{-3}	2.28×10^{-3}	0.070	6.0

A.3 Synthetic Data Generation (Generic Metal Dataset)

Table A.4: Parameters of Chaboche Model used for data generation in Chapter 3.

$\mathbf{T}$ (°C)	$\boldsymbol{\sigma}_{\text{uts}}$ (MPa)	$\mathbf{M_0}$ (MPa)	$\boldsymbol{\sigma}_{l_0}$ (MPa)	b_1 (MPa^{-1})	b_2 (MPa^{-1})	a	$\boldsymbol{\beta}$
25	950	1500	454	1.070×10^{-3}	1.05×10^{-3}	0.09	10.4
500	850	1150	380	1.156×10^{-3}	1.17×10^{-3}	0.095	10.5
600	750	1050	340	1.35×10^{-3}	1.33×10^{-3}	0.055	10.5
700	600	1050	270	1.70×10^{-3}	1.65×10^{-3}	0.58	10.1
800	400	750	140	2.65×10^{-3}	2.49×10^{-3}	0.18	7.0
900	250	450	50	4.15×10^{-3}	4.05×10^{-3}	0.50	6.7

APPENDIX B

FATIGUE CURVES & GOODMAN DIAGRAMS

B.1 Pre-trained Model (Transfer Learning)

B.1.1 Synthetic Data Generation

The following fatigue curves are generated by the trained transfer learning models for both the single crystal superalloy dataset and the generic metal dataset. While only the $R = -1$ results were presented in Chapter 3, this appendix includes the additional R-ratios covered in the training data. These supplementary SN curves provide a comprehensive representation of the model predictions across all loading conditions considered during training.

Single Crystal Superalloy Dataset

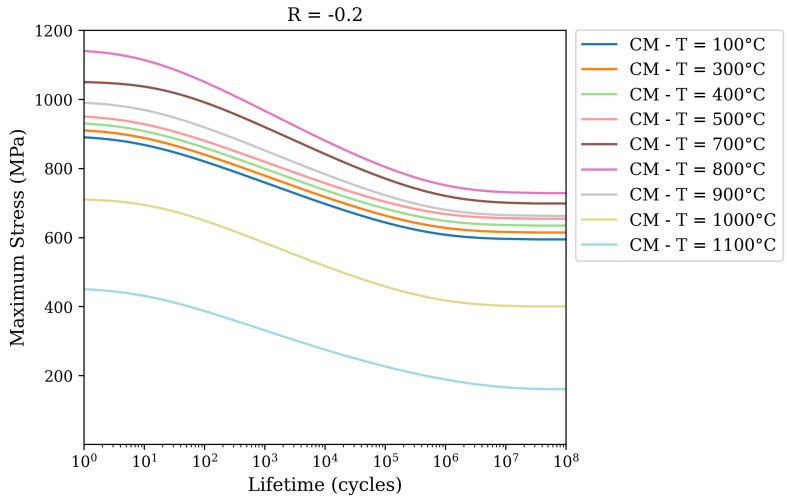

Figure B.1: Synthetic SN curves for CMSX-4 at $R = -0.2$ across 9 temperatures.

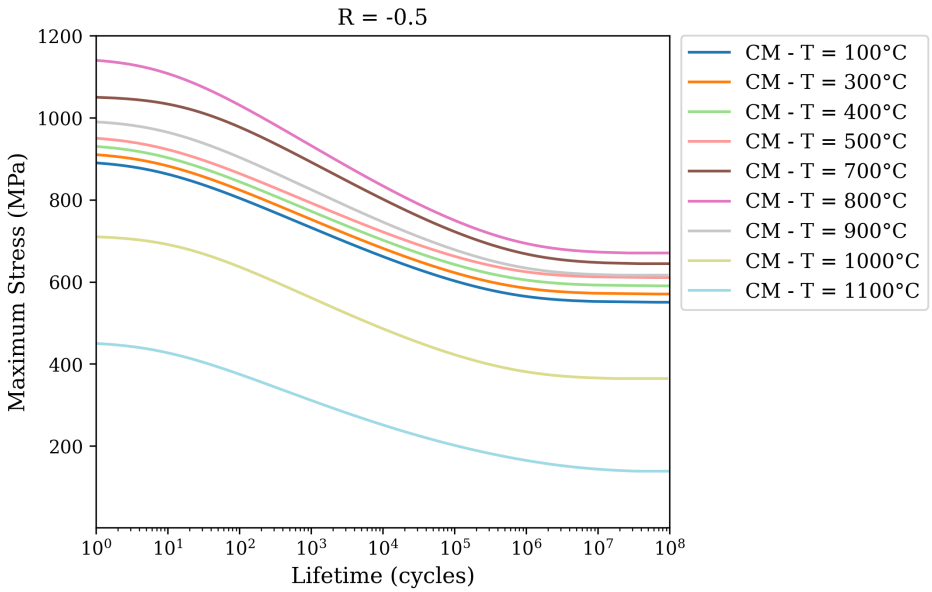

Figure B.2: Synthetic SN curves for CMSX-4 at $R = -0.5$ across 9 temperatures.

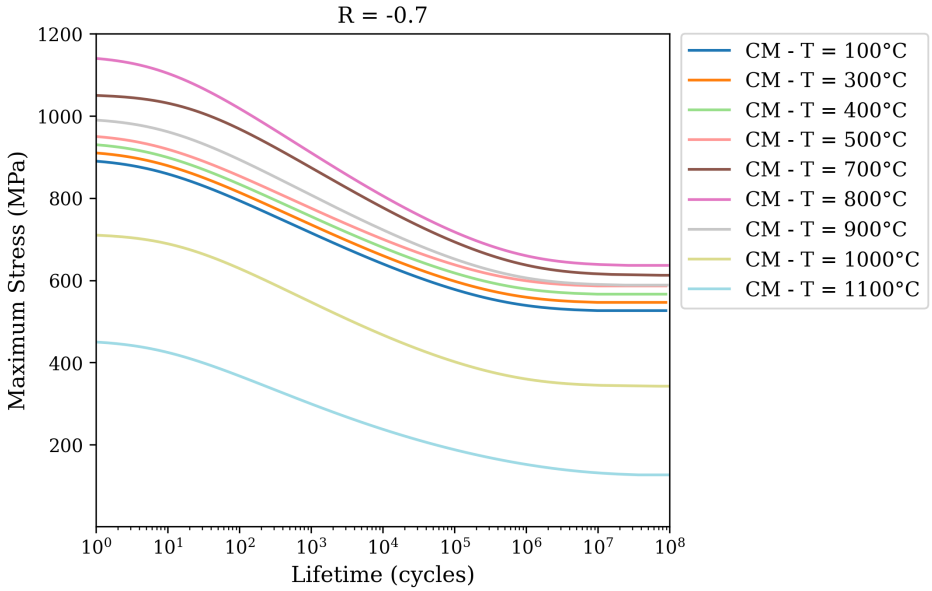

Figure B.3: Synthetic SN curves for CMSX-4 at $R = -0.7$ across 9 temperatures.

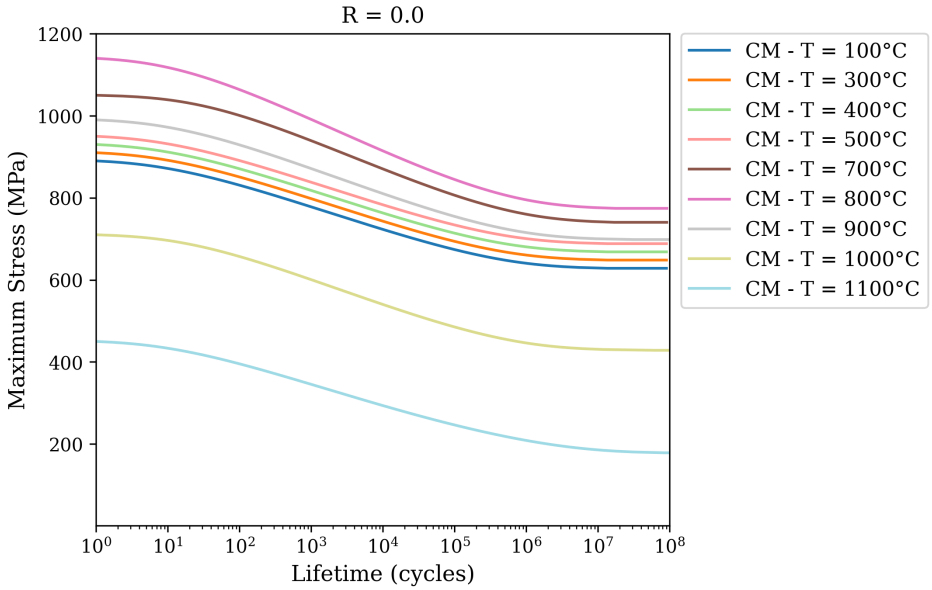

Figure B.4: Synthetic SN curves for CMSX-4 at $R = 0$ across 9 temperatures.

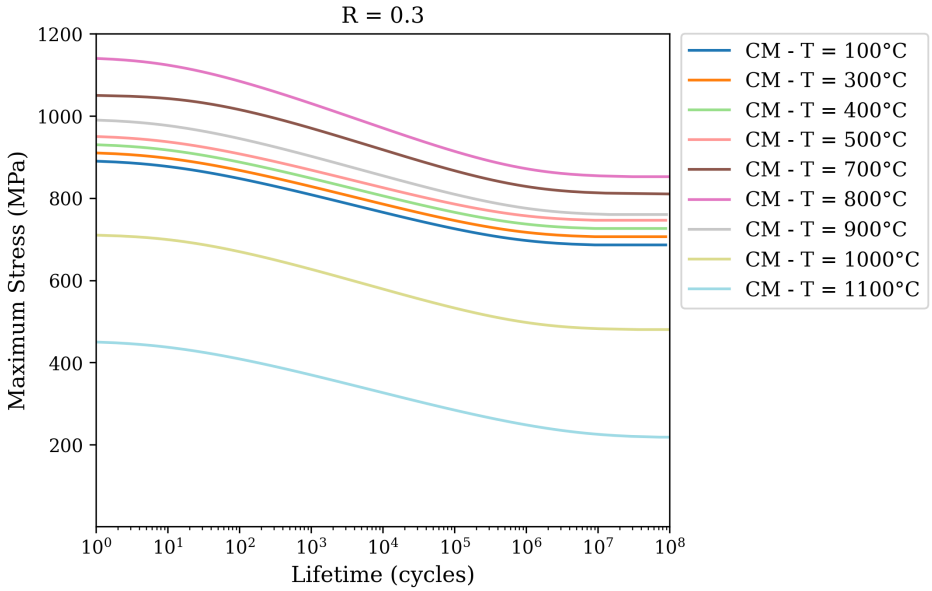

Figure B.5: Synthetic SN curves for CMSX-4 at $R = -0.3$ across 9 temperatures.

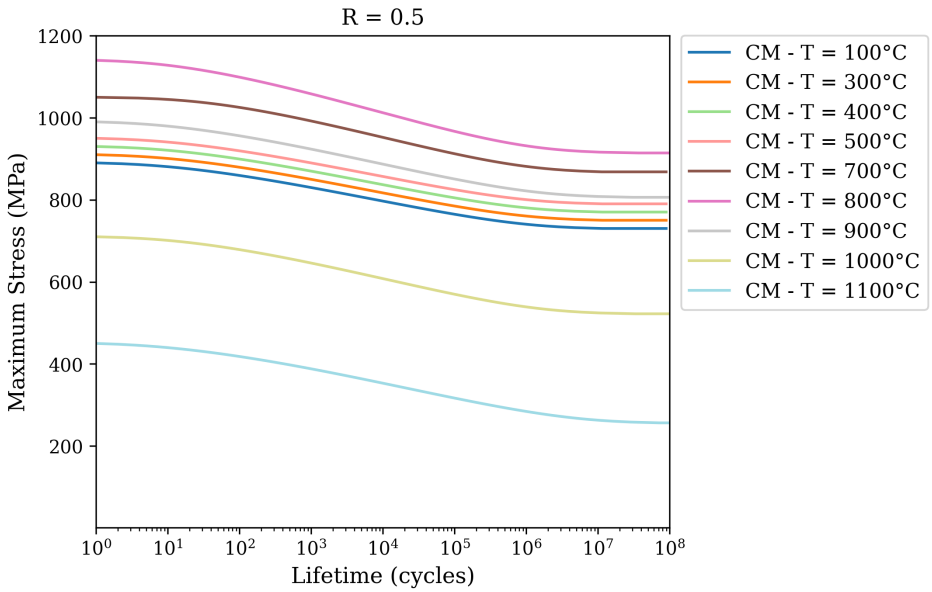

Figure B.6: Synthetic SN curves for CMSX-4 at $R = 0.5$ across 9 temperatures.

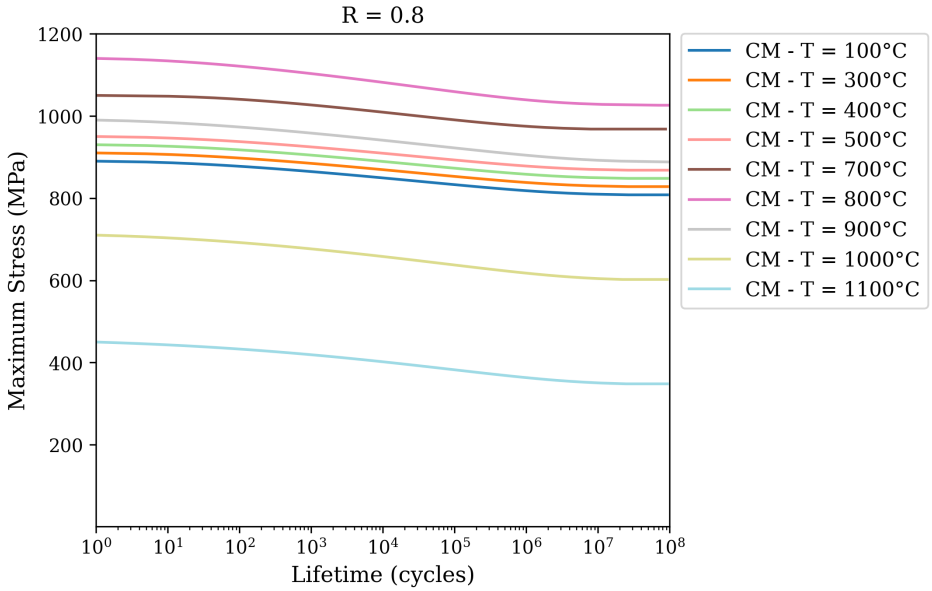

Figure B.7: Synthetic SN curves for CMSX-4 at $R = 0.8$ across 9 temperatures.

Generic Metal Dataset

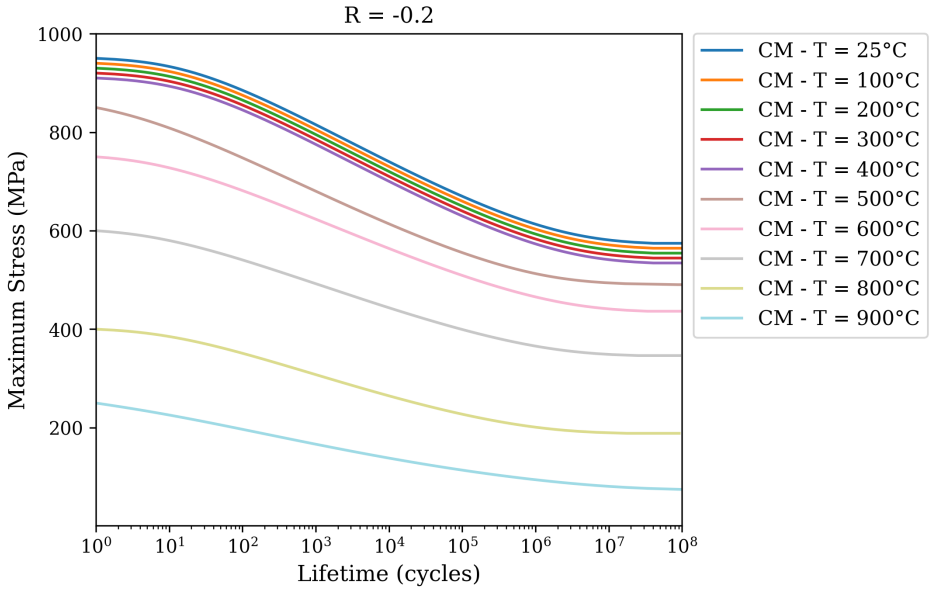

Figure B.8: Synthetic SN curves for the Generic Metal Dataset at $R = -0.2$ across 10 temperatures.

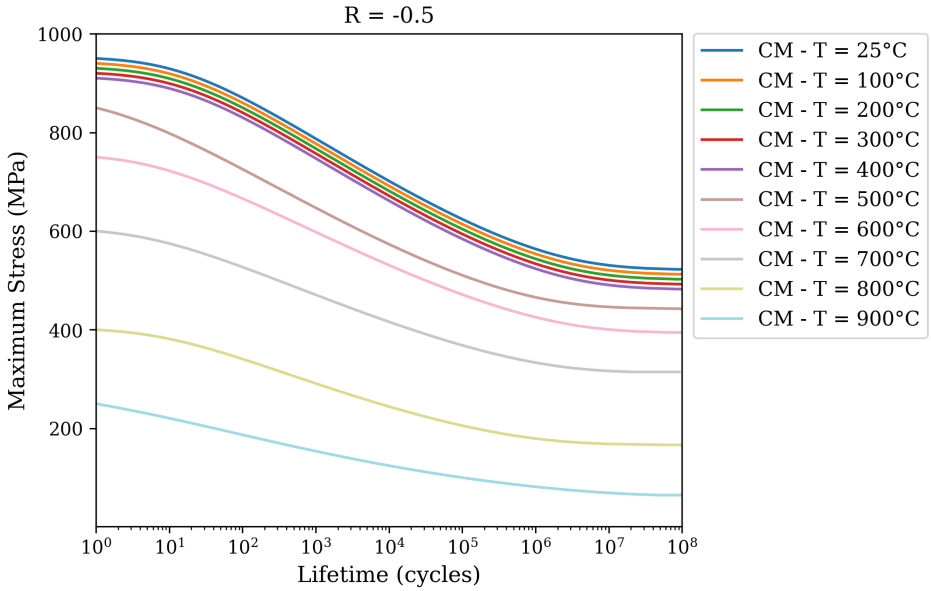

Figure B.9: Synthetic SN curves for the Generic Metal Dataset at $R = -0.5$ across 10 temperatures.

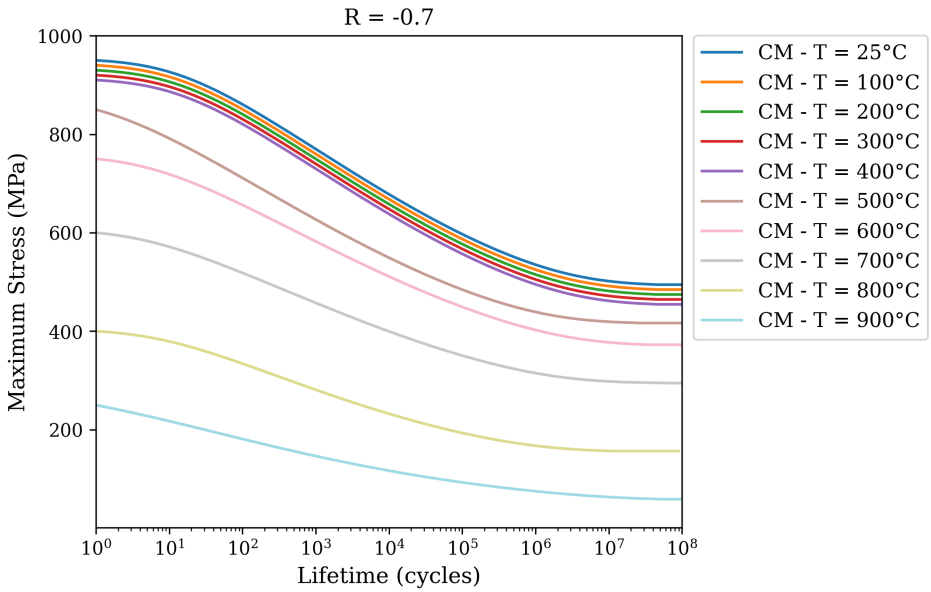

Figure B.10: Synthetic SN curves for the Generic Metal Dataset at $R = -0.7$ across 10 temperatures.

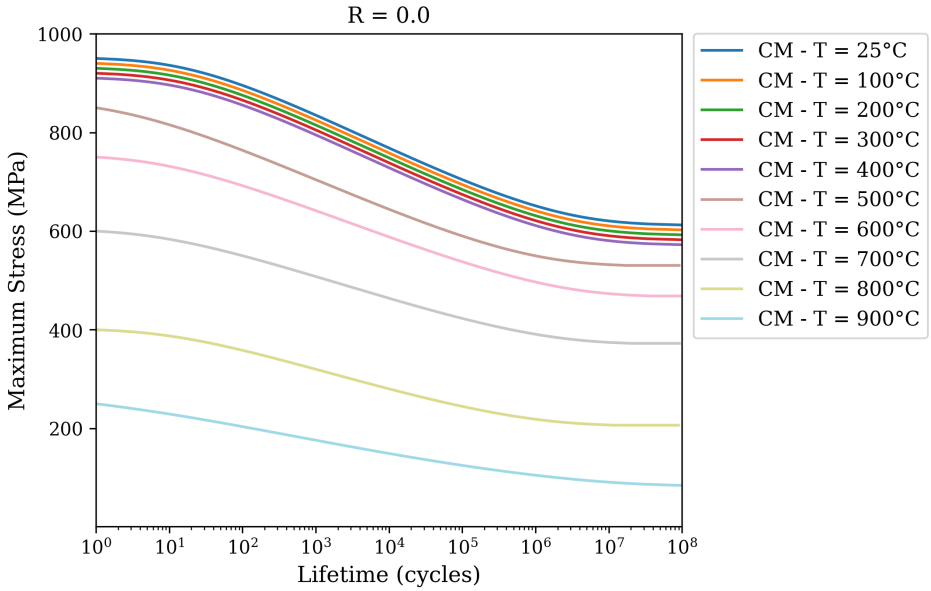

Figure B.11: Synthetic SN curves for the Generic Metal Dataset at $R = 0$ across 10 temperatures.

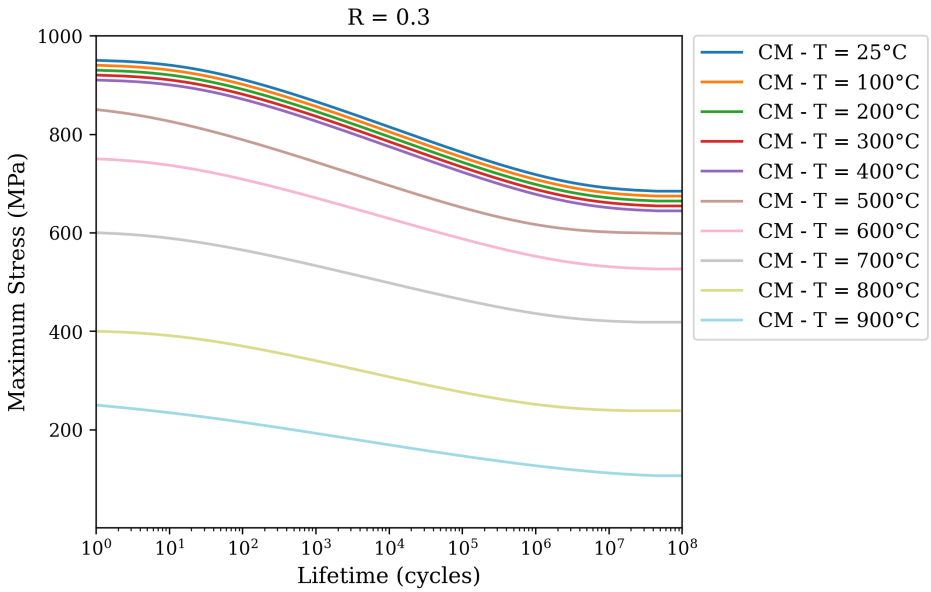

Figure B.12: Synthetic SN curves for the Generic Metal Dataset at $R = 0.3$ across 10 temperatures.

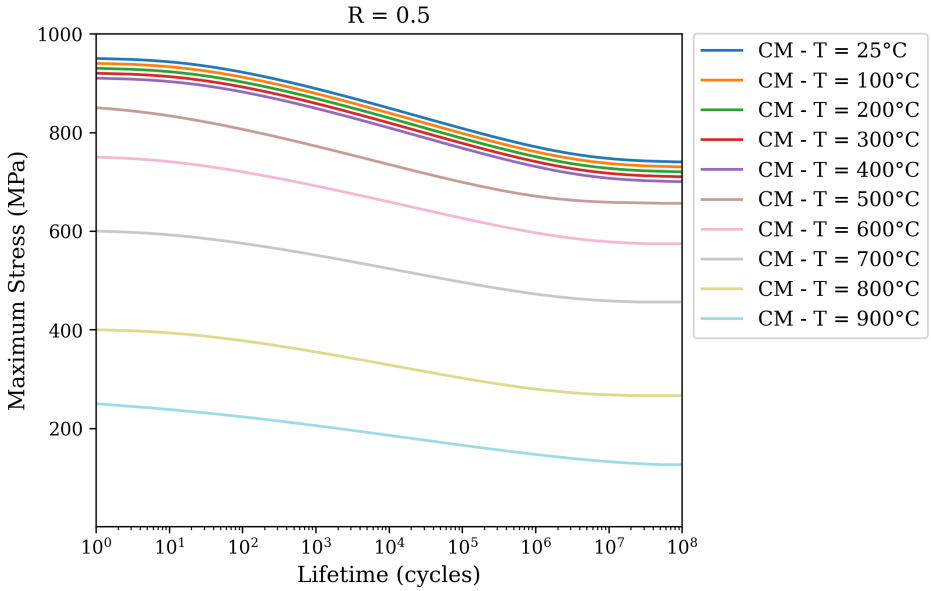

Figure B.13: Synthetic SN curves for the Generic Metal Dataset at $R = 0.5$ across 10 temperatures.

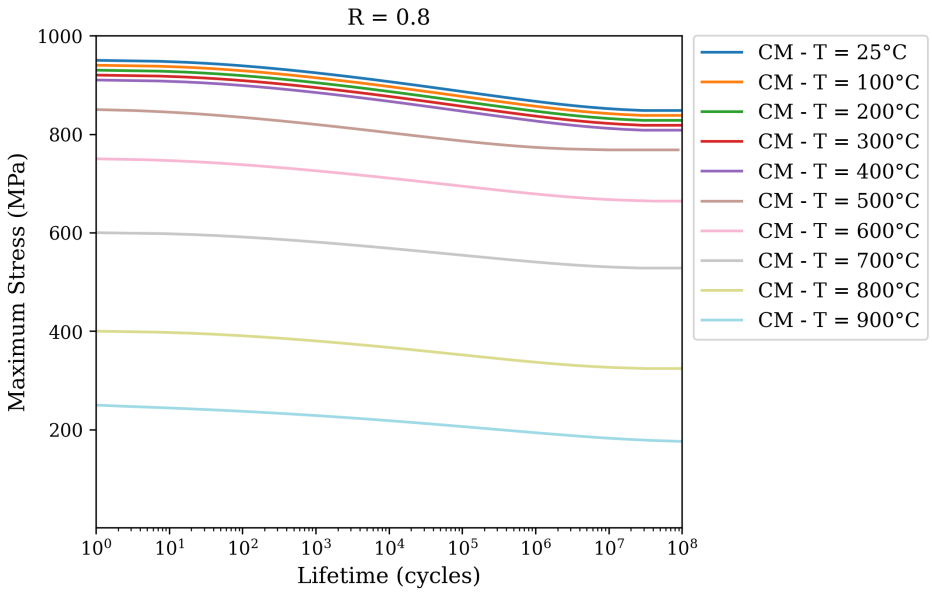

Figure B.14: Synthetic SN curves for the Generic Metal Dataset at $R = 0.8$ across 10 temperatures.

B.1.2 Goodman Diagram Results

The following Goodman diagrams are generated using the pre-trained model, illustrating the predicted safe stress boundaries for multiple target lifetimes across a range of temperatures. While representative results were shown in Chapter 3, this appendix provides a more extensive set of diagrams covering the temperatures included in the training data individually. These figures demonstrate the model's ability to capture the combined effects of mean stress, amplitude stress, and temperature on fatigue life prediction for various fatigue regimes. Since the linear behavior is observed for both single crystal and generic metal datasets, only the single crystal dataset results are represented here.

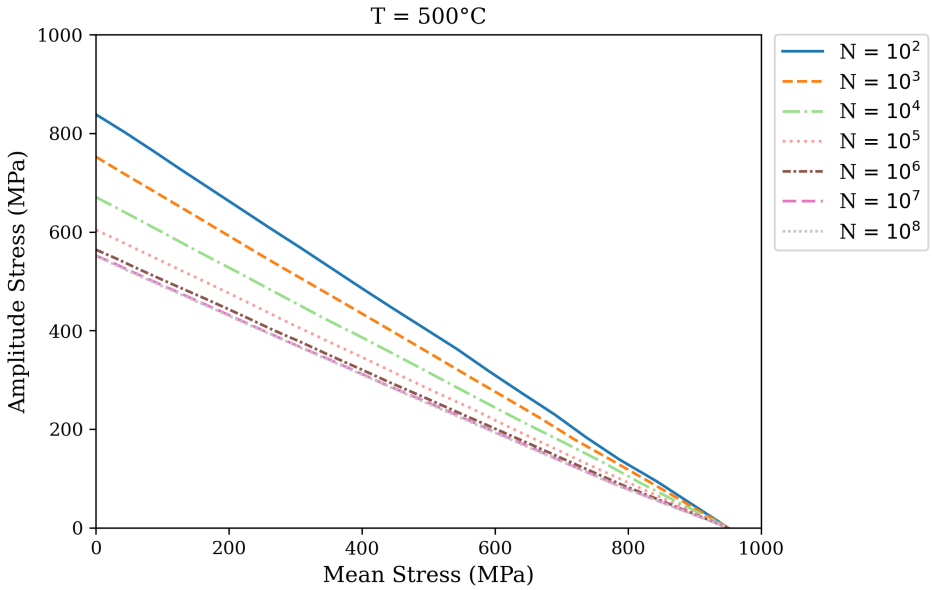

Figure B.15: Goodman diagrams predicted by the pre-trained model for the single crystal superalloy dataset at $T = 500°C$.

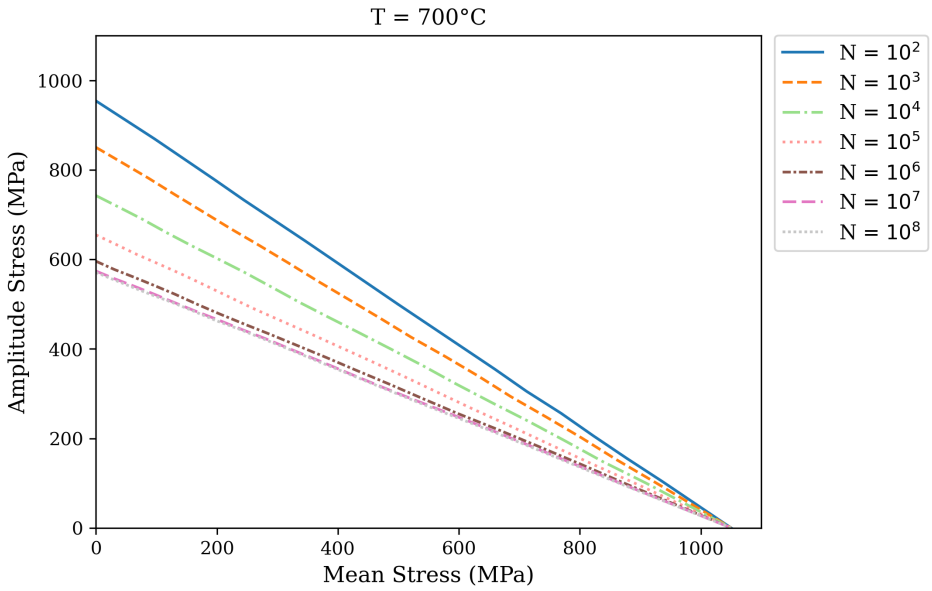

Figure B.16: Goodman diagrams predicted by the pre-trained model for the single crystal superalloy dataset at $T = 700°C$.

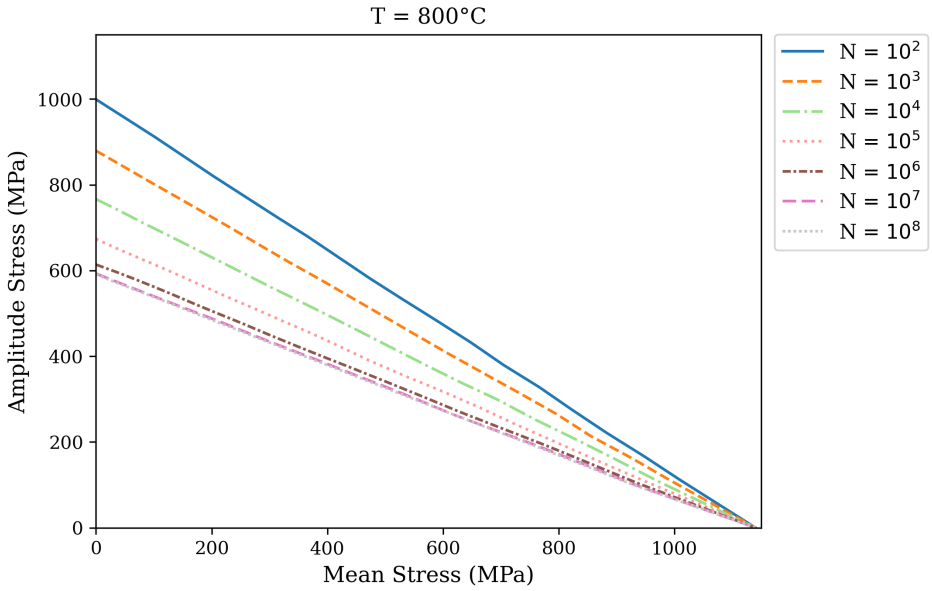

Figure B.17: Goodman diagrams predicted by the pre-trained model for the single crystal superalloy dataset at $T = 800°C$.

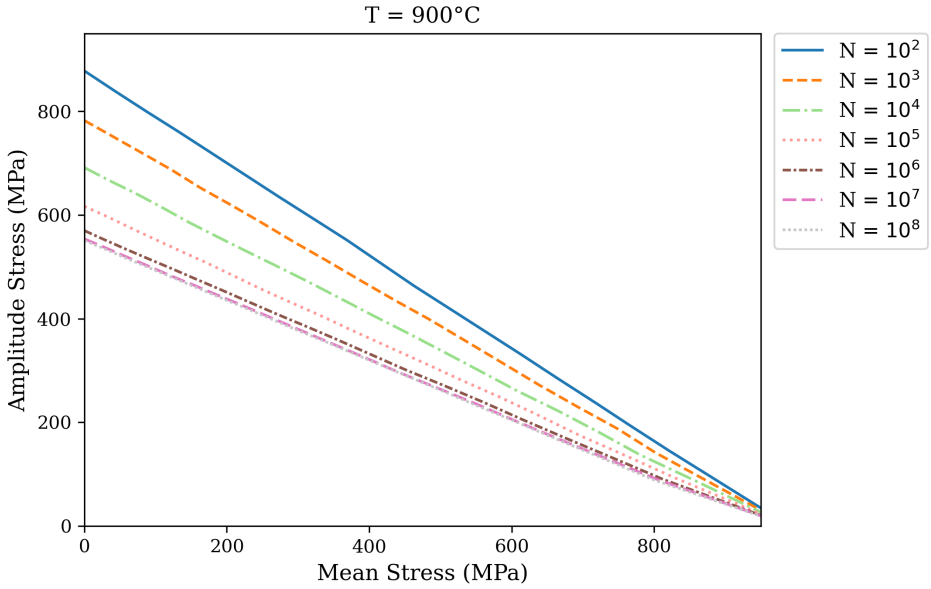

Figure B.18: Goodman diagrams predicted by the pre-trained model for the single crystal superalloy dataset at $T = 900°C$.

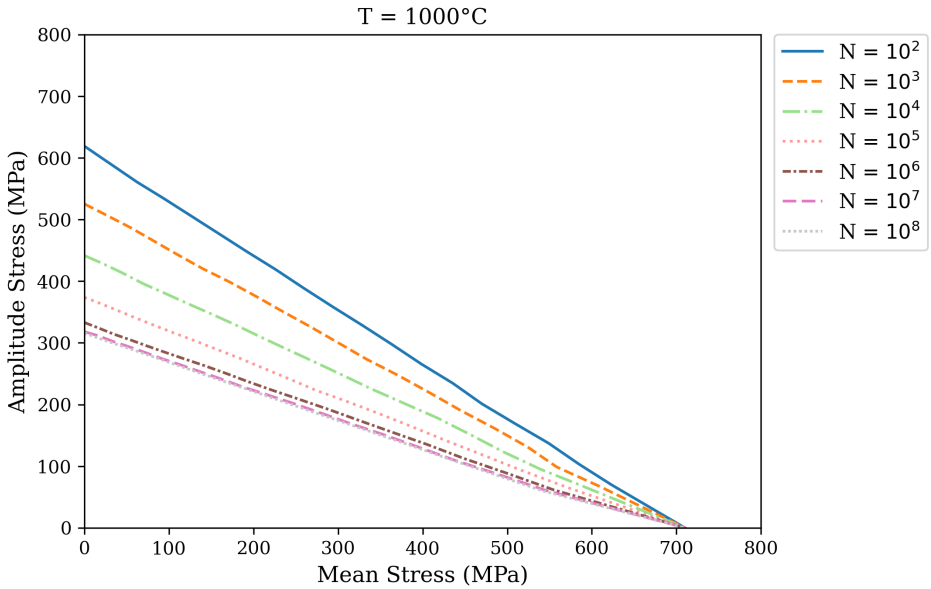

Figure B.19: Goodman diagrams predicted by the pre-trained model for the single crystal superalloy dataset at $T = 1000°C$.

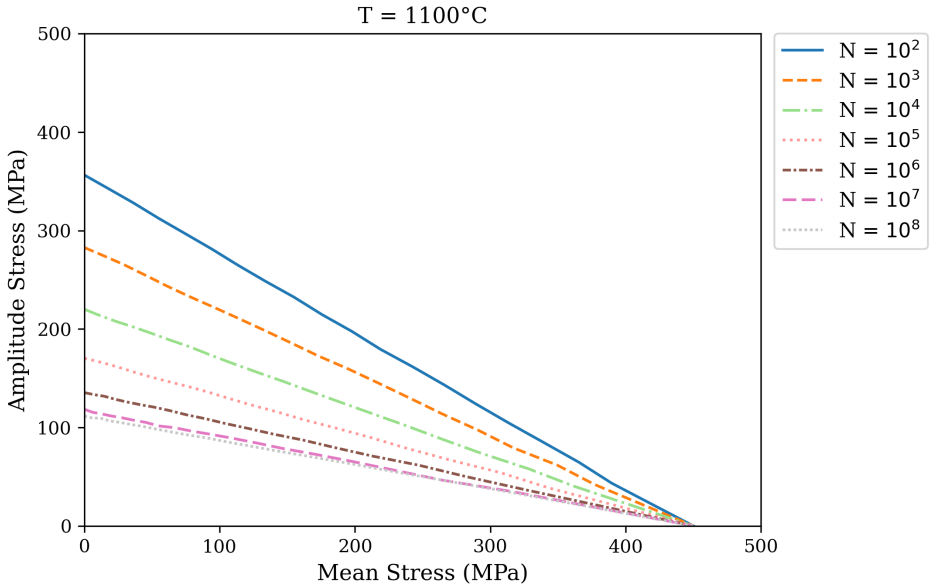

Figure B.20: Goodman diagrams predicted by the pre-trained model for the single crystal superalloy dataset at $T = 1100°C$.

CURRICULUM VITAE

Surname, Name: Kaftancıoğlu, Utku

EDUCATION

Degree	Institution	Year of Graduation
Integrated PhD	Atılım University Mechanical Engineering	2025
BS	Middle East Technical University Metallurgical and Materials Engineering	2020
High School	Etimesgut Anadolu High School, Ankara	2014

FOREIGN LANGUAGES

Fluent English

PUBLICATIONS

1. Ç. Kasar, U. Kaftancioglu, E. Bayraktar, and O. Aslan, "Lifetime prediction of single crystal nickel-based superalloys," *Applied Sciences*, vol. 15, p. 201, 2025.
2. U. Kaftancıoglu, G. Zambelis, F. Gatamorta, I. Miskioglu, and E. Bayraktar, "Development of Ni-Al/Nb_2Al/ZrO_2-based composites for aircraft engine applications produced by a combined method: sintering + forging," in *Mechanics of Composite, Hybrid & Multi-functional Materials, Volume 5*, V. Chalivendra and F. Gardea, Eds., SEM 2022, Springer, Cham, 2023.

RESEARCH INTERESTS

- ➢ Lifetime Assessment Modeling
- ➢ Artificial Neural Networks
- ➢ Transfer Learning
- ➢ Parameter Optimization